RADAR TARGET DETECTION IN NON-GAUSSIAN CLUTTER

A THESIS SUBMITTED TO
THE GRADUATE SCHOOL OF NATURAL AND APPLIED SCIENCES
OF
MIDDLE EAST TECHNICAL UNIVERSITY

BY

ÜLKÜ DOYURAN

IN PARTIAL FULFILLMENT OF THE REQUIREMENTS
FOR
THE DEGREE OF DOCTOR OF PHILOSOPHY
IN
ELECTRICAL AND ELECTRONICS ENGINEERING

SEPTEMBER 2007

Approval of the thesis:

RADAR TARGET DETECTION IN NON-GAUSSIAN CLUTTER

submitted by **ÜLKÜ DOYURAN** in partial fulfillment of the requirements for the degree of **Doctor of Philosophy in Electrical and Electronics Engineering Department, Middle East Technical University** by,

Prof. Dr. Canan Özgen _____
Dean, Graduate School of **Natural and Applied Sciences**

Prof. Dr. İsmet Erkmen _____
Head of Department, **Electrical and Electronics Engineering**

Prof. Dr. Yalçın Tanık _____
Supervisor, **Electrical and Electronics Engineering Dept., METU**

Examining Committee Members:

Prof. Dr. Mete Severcan _____
Electrical and Electronics Engineering Dept., METU

Prof. Dr. Yalçın Tanık _____
Electrical and Electronics Engineering Dept., METU

Assoc. Prof. Dr. S. Sencer Koç _____
Electrical and Electronics Engineering Dept., METU

Assist. Prof. Dr. Mücahit K. Üner _____
Electrical and Electronics Engineering Dept., Hacettepe Unv.

Assist. Prof. Dr. Çağatay Candan _____
Electrical and Electronics Engineering Dept., METU

Date: _____

I hereby declare that all information in this document has been obtained and presented in accordance with academic rules and ethical conduct. I also declare that, as required by these rules and conduct, I have fully cited and referenced all material and results that are not original to this work.

Name, Last name : Ülkü DOYURAN

Signature :

ABSTRACT

RADAR TARGET DETECTION IN NON-GAUSSIAN CLUTTER

Doyuran, Ülkü

Ph. D, Department of Electrical and Electronics Engineering

Supervisor: Prof. Dr. Yalçın TANIK

September 2007, 137 pages

In this study, novel methods for high-resolution radar target detection in non-Gaussian clutter environment are proposed. In solution of the problem, two approaches are used: Non-coherent detection that operates on the envelope-detected signal for thresholding and coherent detection that performs clutter suppression, Doppler processing and thresholding at the same time. The proposed non-coherent detectors, which are designed to operate in non-Gaussian and range-heterogeneous clutter, yield higher performance than the conventional methods that were designed either for Gaussian clutter or heterogeneous clutter. The proposed coherent detector exploits the information in all the range cells and pulses and performs the clutter reduction and thresholding simultaneously. The design is performed for uncorrelated, partially correlated and fully correlated clutter among range cells. The performance analysis indicates the superiority of the designed methods over the classical ones, in fully correlated and partially correlated situations. In addition, by design of detectors

for multiple targets and making corrections to the conventional methods, the target-masking problem of the classical detectors is alleviated.

Keywords: Radar Target Detection, Non-Gaussian Clutter, Heterogeneous Clutter, Constant False Alarm Rate (CFAR).

ÖZ

GAUSSIAN OLMAYAN KARGAŞA ALTINDA RADAR HEDEF TESPİTİ

Doyuran, Ülkü
Doktora, Elektrik ve Elektronik Mühendisliği Bölümü
Tez Yöneticisi: Prof. Dr. Yalçın Tanık

Eylül 2007, 137 sayfa

Bu çalışmada, yüksek çözünürlüklü radarlarda, Gaussian olmayan ve değişken kargaşa altında hedef tespit yöntemleri önerilmektedir. Problemin çözümünde iki ayrı yaklaşım benimsenmiştir: İşlenmiş sinyalin genlik değeri üzerinde çalışan eşikleme yöntemi ve kargaşa bastırma, Doppler işleme, eşikleme işlemlerini birlikte gerçekleştiren uyumlu filtreleme yöntemi. Değişken ve Gaussian-olmayan kargaşa altında çalışmak üzere tasarlanan yöntemler, Gaussian kargaşalı veya heterojen ortamda çalışmak üzere tasarlanmış klasik yöntemlere göre üstün başarı sağlamaktadır. Önerilen uyumlu detektör ise kargaşa bastırma ve eşiklemeyi bir arada yapmakta ve tüm darbe ve menzil hücrelerinden yararlanmaktadır. Çalışmada, farklı ilinti değerlerindeki kargaşaya sahip komşu hücreler kullanılmış ve GLRT-detektörleri tasarlanmıştır. Yöntemin, klasik metotlara göre üstünlüğü başarım analizi ile gösterilmiştir. Ayrıca, çok sayıda hedef için detektör tasarlanarak ve klasik

yöntemde düzeltme yaparak, klasik yöntemlerin çoklu-hedef durumundaki maskeleme problemi engellenmiştir.

Anahtar Kelimeler: Radar Hedef Tespiti, Gaussian Olmayan Kargaşa, Değişken Kargaşa, Sabit Yanlış Alarm Oranı (SYAO)

ACKNOWLEDGMENTS

I would like to express my gratitude to my supervisor Dr. Yalçın Tanık for his guidance, vast knowledge, expertise and patience. I would like to thank the committee members Dr. Sencer Koç, Dr. Yahya Baykal, Dr. Mete Severcan, Dr. Mücahit Üner and Dr. Çağatay Candan for their invaluable advices.

I am grateful to my family for their support through my entire life and in particular, I thank my husband and best friend, Enis, for his love, encouragement and understanding.

Finally, I would like to thank all my friends and colleagues for their support and help.

TABLE OF CONTENTS

ABSTRACT ..... **iv**

ÖZ ..... **vi**

ACKNOWLEDGMENTS ..... **viii**

TABLE OF CONTENTS ..... **ix**

LIST OF TABLES ..... **xi**

LIST OF FIGURES ..... **xii**

ABBREVIATIONS ..... **xv**

1 INTRODUCTION **1**

2 RADAR PRINCIPLES **5**

2.1 Basic Principles 5

2.2 Radar Signals 8
2.2.1 Target Signal 8
2.2.2 Clutter Signal 8

2.3 Radar Detection 16
2.3.1 Clutter Suppression and Doppler Processing 16
2.3.2 Thresholding and CFAR 19

3 NONCOHERENT CLUTTER ESTIMATION **22**

3.1 Weibull Parameter Estimation 22
3.1.1 Method of Moments 23
3.1.2 Maximum-Likelihood Estimation 25

3.2 K-Distribution Parameter Estimation 26
3.2.1 Method of Moments 27
3.2.2 Maximum-Likelihood Estimation 28

4 NONCOHERENT THRESHOLDING 29

4.1 Clutter Model 30

4.2 Goodness-of-Fit CFAR 30

4.3 Expectation-Maximization CFAR 43
4.3.1 Two-Level Algorithm 45
4.3.2 Multi-Level Algorithm 51

4.4 Clutter-Map CFAR 63
4.4.1 Method of Scoring 64
4.4.2 RLS Estimation 68

5 COHERENT CLUTTER ESTIMATION 75

5.1 Compound-Gaussian Clutter Notation 76

5.2 ML Estimation 81
5.2.1 Cramer-Rao Lower Bound for Nonrandom Texture Parameter 81
5.2.2 No Spatial Correlation 83
5.2.3 Full Spatial Correlation 87
5.2.4 ML Estimation in Additive Noise Case 88

5.3 MAP Estimation 90
5.3.1 Cramer-Rao Lower Bound for Random Texture Parameter 90
5.3.2 No Spatial Correlation 92
5.3.3 Full Spatial Correlation 93
5.3.4 Partial Spatial Correlation 94

5.4 Performance Analysis 97

6 COHERENT DETECTION 100

6.1 Detector 101
6.1.1 No Spatial Correlation 102
6.1.2 Full Spatial Correlation 106
6.1.3 Partial Spatial Correlation 114
6.1.4 GLRT-MAP Detector 115

6.2 Detection in Multiple-Target Environment 116

7 CONCLUSION 127

REFERENCES 130

CURRICULUM VITAE 137

LIST OF TABLES

Table 4.1 Anderson-Darling Goodness-of-Fit Test Critical Values 32

Table 4.2 Anderson-Darling Goodness-of-Fit Test performance in heterogeneity identification 37

Table 4.3 GoF-CFAR, probability of detection in homogeneous case 41

Table 4.4 GoF-CFAR, probability of detection in non-homogeneous case- Same SCR, different shape parameters 42

Table 4.5 GoF-CFAR, probability of detection in non-homogeneous case- Different SCR, different shape parameters 43

Table 4.6 EM estimator outputs for scale parameters of two levels and a prior probability of PDF 2 50

Table 4.7 EM-CFAR test scenario 1, assumed shape parameters and a priori probabilities 58

Table 4.8 EM-CFAR test scenario 1, actual distribution parameters 58

Table 4.9 EM-CFAR, estimated distributions 59

Table 4.10 EM-CFAR, estimated distribution parameters and a priori probabilities.60

Table 4.11 Parameter estimation using EM-CFAR algorithm and improved algorithm which uses ML estimation 61

Table 4.12 EM-CFAR test scenario 2, actual distribution parameters 61

Table 6.1 Summary of detectors 110

Table 6.2 Detection probabilities of the detectors for single and two target cases. 122

Table 6.3 Detection probabilities of the double-target and single target GLRT 126

LIST OF FIGURES

Figure 2.1 Weibull probability density functions for various shape parameters 11

Figure 2.2 Weibull probability density functions for various scale parameters 12

Figure 2.3 K-distribution probability density functions for various shape parameters 13

Figure 2.4 K-distribution probability density functions for various scale parameters 14

Figure 4.1 Clutter heterogeneity, PDF transition from $f_x(x, \alpha_1, \beta_1)$ to $f_x(x, \alpha_2, \beta_2)$... 30

Figure 4.2 Threshold parameter for Weibull distribution versus different number of samples, $P_{FA} = 10^{-5}$ 35

Figure 4.3 Probability of false alarm versus threshold parameter for Weibull distribution for different number of samples 35

Figure 4.4 GoF-CFAR, performance of transition point estimation 37

Figure 4.5 GoF-CFAR, probability of detection versus SCR in homogeneous clutter for various shape parameters. 38

Figure 4.6 GoF-CFAR, signal variation in range-heterogeneous clutter and threshold levels for various CFAR methods – no target 40

Figure 4.7 Amplitude variation with range of range-heterogeneous clutter and threshold levels for various CFAR methods - target 40

Figure 4.8 Clutter heterogeneity, PDF transition from $f_x(x, \alpha_1, \beta_1)$ to $f_x(x, \alpha_2, \beta_2)$.. 45

Figure 4.9 Posterior-probability estimate of EM-CFAR algorithm. 50

Figure 4.10 Change of probability of false alarm with the ratio of actual and estimated shape parameters 56

Figure 4.11 Designed shape parameter set for the multi-level EM-CFAR algorithm 57

Figure 4.12 EM-CFA, a posteriori probabilities of the assumed distributions 59

Figure 4.13 EM-CFAR, scale parameter estimates for each simulation point 62

Figure 4.14 Amplitude of the signal and the threshold values obtained with EM-CFAR algorithm 63

Figure 4.15 Histograms of estimates obtained with method of scoring 67

Figure 4.16 CM-CFAR, change of detection probability with SCR for different shape parameter values 73

Figure 4.17 CM-CFAR, probability of detection in the time-varying scenario 73

Figure 4.18 CM-CFAR, probability of false alarm in the time-varying scenario 74

Figure 5.1 Received vector illustration 80

Figure 5.2 Video signal, moderate clutter 80

Figure 5.3 Video signal, spiky clutter 81

Figure 5.4 Performance of texture parameter estimation 86

Figure 5.5 Mean squared estimation error (no correlation) 97

Figure 5.6 Mean squared estimation error (full correlation) 98

Figure 5.7 Mean squared estimation error (partial correlation) 99

Figure 6.1 Detection performance versus SCR, various number of range cells 111

Figure 6.2 Detection performance versus speckle correlation coefficient, various number of pulses 111

Figure 6.3 Detection performance versus Doppler frequency, various number of pulses 112

Figure 6.4 Detection performance versus SCR, various number of range cells, large number of pulses 113

Figure 6.5 Detection performance, various number of range cells, small number of pulses 113

Figure 6.6 Detection performance versus Doppler frequency, various number of range cells..... 114

Figure 6.7 Detection performance versus SCR for various texture correlation coefficients..... 115

ABBREVIATIONS

CFAR	: Constant False Alarm Rate
CRLB	: Cramer-Rao Lower Bound
CUT	: Cell Under Test
EM	: Expectation Maximization
FFT	: Fast Fourier Transform
GLRT	: Generalized Likelihood Ratio Test
GO-CA	: Greater Of Cell Averaging
GoF	: Goodness of Fit
PDF	: Probability Density Function
LRT	: Likelihood Ratio Test
MAP	: Maximum A Posteriori
ML	: Maximum Likelihood
MMSE	: Minimum Mean Squared Error
MTI	: Moving Target Indication
OS	: Ordered Statistics
RCS	: Radar Cross Section
RLS	: Recursive Least Squares
SAR	: Synthetic Aperture Radar
SIR	: Signal to Interference Ratio
SIRP	: Spherically Invariant Random Process
SNR	: Signal to Noise Ratio
SO-CA	: Smaller Of Cell Averaging
STAP	: Space Time Adaptive Processing

CHAPTER 1

INTRODUCTION

The detection of target signals in a background of unwanted echoes, called clutter, which stem from the sea, land or weather, is one of the most important problems of radar systems. Solution of the problem necessitates the understanding of the statistics of the clutter, such as its distribution and correlation properties.

In classical radar systems, the clutter signal is assumed to have Gaussian distribution, which enables the use of the simple and conventional detection algorithms. However, in modern high-resolution radars and especially at low grazing angles, the clutter exhibits a spiky characteristic and the Gaussian assumption is no longer valid [6], [37], [62]. Classical algorithms, designed for Gaussian clutter, yield many orders of higher false alarm rates when operated in non-Gaussian cluttered environment. Hence, the spiky characteristic should necessarily be considered in design of the detector and the statistical model of the clutter should be formulated. In modeling the high-resolution clutter distribution, beside the scale or power of the distribution, another parameter, called shape or order parameter, which defines the spikiness, is introduced [1], [6], [41], [61]. The most common distributions that are used for non-Gaussian clutter envelope are Weibull and K-distribution. In representing the multi-pulse coherent non-Gaussian clutter, compound Gaussian model is used [5], [12], [13], [24], [45], [53], [60].

Another problem in detection of targets is a change in clutter statistics, in time or space. Usually, radar systems use adaptive algorithms in order to follow the changes in the statistics. However, abrupt changes degrade the performance of the adaptive detection algorithms, which make use of the spatially or temporally neighboring cells in estimation of the clutter characteristics and determination of the threshold [23], [47]. There are many methods designed to operate under non-Gaussian clutter [26], [36], [46] or range-heterogeneity [9], [25]. However, none of the methods is suitable for the dual problem.

The detection schemes can be categorized into two main groups: Noncoherent and coherent detection techniques. In the first one, a classical clutter suppression and Doppler processing method is followed by envelope detection. The real signal obtained by this way is analyzed non-coherently to set the appropriate threshold. This operation can also be applied to radar signals that do not retain coherency, such as frequency-agile signals. Examples are given in [1], [23], [29], [46], [50] and [63]. In the second group, a detector is designed to perform the clutter suppression, Doppler processing and thresholding operations simultaneously by operating on the pulses coherently [26], [28], [34], [42], [49], [51].

In this thesis, both noncoherent and coherent detection methods to operate in non-Gaussian clutter environment are designed. In many of the works in the literature, the shape parameter of the clutter is assumed to be known. In this study, both of the parameters are assumed to be unknown and they are estimated.

Three non-coherent techniques, namely, Goodness-of-fit, Expectation-maximization and Clutter-map CFAR, are designed and analyzed. In the first two techniques, heterogeneity of the window that is used in estimation of the clutter parameters is tested and the parameters of the dissimilar regions are determined. With this information, a threshold is set according to the desired false alarm probability. These techniques are novel in that they operate under clutter which is non-Gaussian and heterogeneous. Besides, it is believed that using a Goodness-of-fit test in

heterogeneity detection in CFAR operation is original. In clutter map CFAR method, the parameter estimation is updated at every scan of the radar and the threshold is set using the estimates. Clutter map method is not affected from the range-heterogeneity problem as the spatial-neighbors are not used in estimation of the characteristic. This method is also new, in that the two parameters of the distribution are assumed to be unknown and they are estimated and updated, forming the clutter map. In the literature survey, a two-parameter clutter map CFAR method was not encountered.

In coherent detection, all of the range cells and pulses are utilized as input to the detector. The likelihood-ratio-test is considered as the optimal detection scheme [14], [34], [52], [59]. Since the detector is dependent on the clutter and the target parameters, they are estimated, using maximum likelihood and maximum-a-posteriori estimation techniques to form the generalized likelihood-ratio test. In the study, three cases of texture correlation among range cells are considered: No-correlation, partial-correlation and full-correlation. The estimators and detectors are derived for all of the cases. The well known detectors that use the same approach do not operate on all of the range cells and are shown to experience performance loss in fully and partially-correlated cases. The main contribution of this study is to design a general detector that uses all the available information in neighboring range cells.

It is shown that in multiple target scenarios, the detectors that operate on a single range cell [26], [28], [34], [42], [49], [51], have significant performance degradation and cause even the masking of the target. The reason of this is that the only information that is used in estimation of the clutter is on that range cell, which is corrupted by an interfering target. In this study, a detector is proposed to alleviate the interfering-target masking problem. Also, another method is proposed to succeed the classical detector to make it operate in multiple-target case, which is believed to be novel.

The thesis is organized as follows: In Chapter 2, basic radar principles, information on clutter signal properties and detection schemes are given. In Chapter 3, some

important noncoherent clutter estimation techniques, which estimate the distribution parameters of the non-Gaussian clutter envelope, are described. In Chapter 4, the noncoherent thresholding techniques that operate on Weibull distributed clutter are explained. The coherent estimation techniques that use all the information in the range-cells and pulses to estimate the power of the compound-Gaussian signal for full-correlation, no-correlation and partial correlation cases using ML and MAP approaches are explained in Chapter 5. The estimators derived in Chapter 5 are exploited in design of the GLRT detectors for compound-Gaussian clutter, which are presented in Chapter 6. Concluding remarks are stated in Chapter 7.

CHAPTER 2

RADAR PRINCIPLES

The basic principle of a radar system is transmission of electromagnetic waves and processing of the echo signal in order to extract the necessary information. The information to be obtained varies with the type of the radar. For example, search radars process the echo signal in order to detect targets, obtain their positions and velocities, while tracking radars track the detected targets and obtain the trajectory of them. Imaging radars generate an image of the ground and perform operations such as detection of the targets and classification. There exist many functions and algorithms that perform the cited operations for various types of radars [17], [43], [47], [54], [56].

In the following sections, basic radar principles, detection and interference models are reviewed.

2.1 Basic Principles

The main problem in radar detection is determining whether the received echo signal contains the signal reflected from a target or only interference. Detection is performed by means of cancellation of the clutter and comparing the amplitude of the output to a threshold which is usually computed adaptively using the echo signal. In analyzing the performance of detection, probability of detection and probability of false alarm are the most important criteria. Keeping the other parameters fixed,

increasing or decreasing one of the parameters increases or decreases the other as well. The relation between these parameters is a function of the Signal to Interference Ratio (SIR).

The range information of a target can be extracted from the time delay between the transmission of a pulse and the reception of the echo. Since the time required for a pulse to be reflected from an object at a distance R is $2R/c$, where c is the speed of light, then the target distance for a time delay of t_D can be found using

$$R = c\, t_D / 2 . \tag{2.1}$$

In modern radars, signals are processed digitally. The received signal is filtered, demodulated and sampled appropriately to obtain the signal to be processed. The samples form the range bins, each of which has the size

$$\Delta R = c\, t_S / 2 , \tag{2.2}$$

where t_S is the sampling period.

Resolution is the ability to detect multiple targets, which are close, as separate targets. Resolution cell size may be different from the range cell size. Range resolution depends on the width of the transmitted pulse, while range cell size is determined by the sampling period.

Radial velocity, v, of an object can be measured using the Doppler frequency shift of the echoes by means of the formula

$$v = \frac{c\, f_D}{2\, f_0} , \tag{2.3}$$

where f_D is the Doppler shift and f_0 is the radar operation frequency.

Doppler frequency of a target can be measured by means of spectrum estimation techniques such as Fourier transforms or other types of filter banks.

Multiple measurements of position and radial velocity can be used to determine the motion of the target in three dimensions.

Radar receives many forms of interference that makes the detection and information extraction process difficult. These interfering signals can be so high that they can mask the desired echoes. The most important kind of interference is *clutter*, which is defined as the unwanted echoes from the environment. If the desired signal is the airborne target echoes, then the echoes from sea, land, weather form the clutter. Detailed information on clutter signal is given in the subsection. The other kind of interference is the thermal and external noise. The electromagnetic interference (EMI) and electronic countermeasures (ECM) are the other two types of interference that a radar system must deal with.

The relation between the received echo power and transmitted power in a radar system is given by the radar equation, which is

$$P_r = \frac{P_t G_t G_r \lambda^2 \sigma}{(4\pi)^3 R^4 L}. \tag{2.4}$$

Here, P_t and P_r denote the transmitted and received powers; G_t and G_r show the transmitter and receiver antenna gains, respectively. λ is the wavelength and σ is the radar cross section (RCS) of the target. R represents the target range and L is the total loss (Systems losses and atmospheric attenuation). The equation given above is valid for a point scatterer. Other forms of this equation can be found in [47] and [54].

2.2 Radar Signals

Received radar signal consists of echoes from targets, clutter, thermal noise and other types of interference. Modeling these signals appropriately is vital in successful design of a radar system. In this section, information on target, clutter and noise signal models are given.

2.2.1 Target Signal

The return from a target has a power directly proportional to the radar cross section (RCS) of the target. The radar cross section is defined as an equivalent area that relates the incident power density to the reflected one from the target. RCS of a target varies with respect to the angle, frequency and polarization and it may experience a fluctuation. The most common models that are used in target RCS fluctuation are *Swerling models* [47], [54]. Swerling 1 and Swerling 3 cases correspond to decorrelation from scan-to-scan, while Swerling 2 and Swerling 4 cases correspond to pulse-to-pulse decorrelation. For Swerling 1 and 2 cases, the probability density function of the RCS is Rayleigh and for Swerling 3 and 4 cases, it is Chi-squared with degrees of freedom 4. Swerling 0 refers to a stationary target return.

2.2.2 Clutter Signal

Radar clutter modeling is a complicated task, especially when the clutter is received with a high-resolution radar at a low grazing angle. As a random process, clutter can be defined by means of its spatial and temporal statistical characteristics. Spatial characteristics definition is composed of amplitude statistics and correlation distances. Similarly, temporal variation is defined by amplitude statistics and correlation times.

Spatial and Temporal Characteristics

The earlier assumption on spatial amplitude distribution of the clutter signal was Rayleigh, which is a single parameter distribution. However, recent studies and experimental analysis indicate deviation from Rayleigh PDF, especially in high-resolution radars and at low grazing angles. The reason is that in high-resolution radars, as the number of scattering components is finite or fluctuating in a cell, central limit theorem is no longer valid and Gaussian assumption does not hold. The most common models to represent this type of radar clutter are Weibull, lognormal and K, which are two-parameter distributions. Lognormal distribution, which is sometimes used in sea clutter modeling, is not as widely adopted as the other distributions [13], [24]. Unlike log-normal PDF, K and Weibull distributions cover Rayleigh distribution as a special case.

In a recent paper, characteristic of real clutter data was analyzed [5]. It was validated that first order amplitude statistics fits to Weibull or K-distribution. The in-phase and quadrature components were found to be identically distributed; have symmetric PDF and are non-Gaussian.

In another work, a convenient model to represent non-Gaussian radar clutter was explained [13], [60]. This model represents the clutter as a Gaussian speckle, x, modulated by a slowly varying texture parameter, τ :

$$\mathbf{r} = \sqrt{\tau}\,\mathbf{x} \tag{2.5}$$

Texture component determines the PDF and the speckle component determines the correlation properties. In order to define the higher order PDF, it is assumed that the texture parameter remains constant and SIRP (Spherically Invariant Random Process) model can be used. Short durations are necessary for this model to be valid.

Another model that was employed in non-Gaussian modeling is alpha-stable distribution [40]. In this model, noise is impulsive, i.e., it exhibits more spikes and occasional bursts than Gaussian distribution. It is a generalization of the Gaussian distribution. It has four parameters: Characteristic exponent, scale parameter (dispersion), symmetry and location. Unfortunately, stable random variables do not have a closed-form PDF expression but, on the other hand, they have power series expansions. However, in a study, it was found that K-distribution fits the sea clutter characteristics better than alpha-stable distribution [30].

Correlation distance is a measure of the sampling point change, for the clutter amplitude to change significantly. It is known that land clutter changes significantly from cell to cell, especially at low angles. Thus, samples from different range cells may be assumed to be independent. On the other hand, it is reported that increased correlation is observed from cell to cell, at high angles over uniform forest or at sea clutter [6].

It is known that the time and space characteristics of radar clutter are different [23]. Experimental results show that temporal distribution was found to be Rayleigh, Ricean or Weibull [6]. Rayleigh distribution was shown to be valid when the signal is reflected from wind-blown foliage. It is claimed that Ricean distribution results when there are fixed discretes embedded in foliage, such as trees.

Spectral definition of radar clutter gives an idea on how long it takes for the clutter amplitude of a given cell to change significantly. This information can be extracted from the power spectrum of the clutter. When the clutter results from rocky mountains, its correlation time is so long that it can be assumed to be constant. However, when the clutter results from wind-blown trees, rain or sea, the internal motion of the clutter causes decorrelation in time [5], [24].

Amplitude Distributions

The Weibull distribution accurately represents the clutter distribution over a wide range of conditions. By adjusting its parameters, it can be made either Rayleigh, or approach to lognormal distribution. The Weibull PDF is defined below:

$$f_W(x) = \frac{\beta}{\alpha}\left(\frac{x}{\alpha}\right)^{\beta-1} \exp\left\{-(x/\alpha)^{\beta}\right\}U(x)\,. \tag{2.6}$$

Here, α and β are the scale and shape parameters, respectively.

The distribution function is

$$F_W(x) = 1 - \exp\left\{-(x/\alpha)^{\beta}\right\}. \tag{2.7}$$

It can be seen in Figure 2.1 and Figure 2.2 that this distribution may have very different forms depending on the parameters. β=*2* corresponds to the Rayleigh distribution. The smaller the shape parameter gets, the spikier the clutter signal becomes.

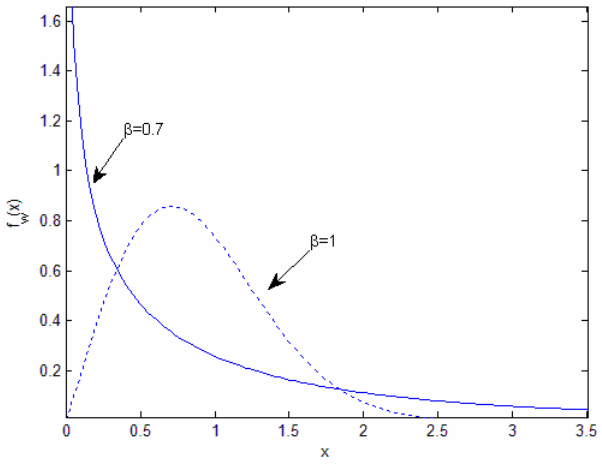

Figure 2.1 Weibull probability density functions for various shape parameters α=1

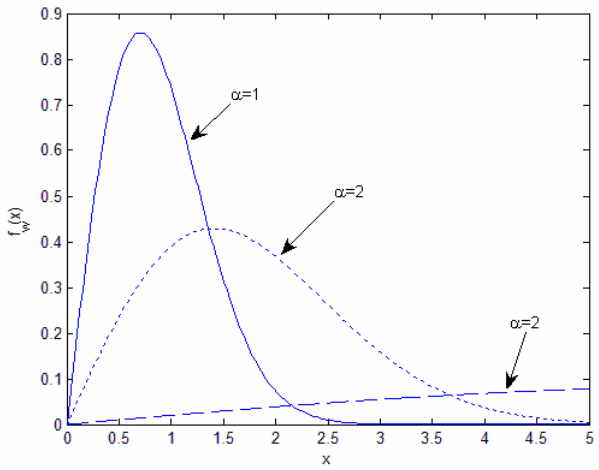

Figure 2.2 Weibull probability density functions for various scale parameters β=2.

The other amplitude distribution that is widely used is K-distribution, which is described by the following probability density function:

$$f_K(x) = \frac{2b}{\Gamma(\nu)}\left(\frac{b\,x}{2}\right)^{\nu} K_{\nu-1}(b\,x)\,U(x), \qquad \nu > 0 \tag{2.8}$$

Here, $\Gamma(\cdot)$ is the Gamma function, $K_\nu(\cdot)$ is the modified Bessel function of the second kind. Parameter b is a positive constant. The functions are defined as

$$\Gamma(z) \stackrel{\Delta}{=} \int_0^1 \left[\ln\left(\frac{1}{t}\right)\right]^{z-1} dt\,, \tag{2.9}$$

$$K_d(z) \stackrel{\Delta}{=} \frac{\Gamma(d+\frac{1}{2})(2z)^d}{\sqrt{\pi}} \int_0^\infty \frac{\cos t}{(t^2+z^2)^{d+1/2}}\,dt\,. \tag{2.10}$$

The shape parameter ν is the measure of the spikiness. The density approaches Rayleigh as the parameter tends to infinity.

The K-distribution function is

$$F_K(x) = 1 - \frac{2}{\Gamma(\nu)}\left(\frac{b\,x}{2}\right)^{\nu} K_{\nu}(b\,x)\,U(x), \qquad \nu > 0 \tag{2.11}$$

The change of the distribution functions with the parameters is shown in the Figures 2.3 and 2.4.

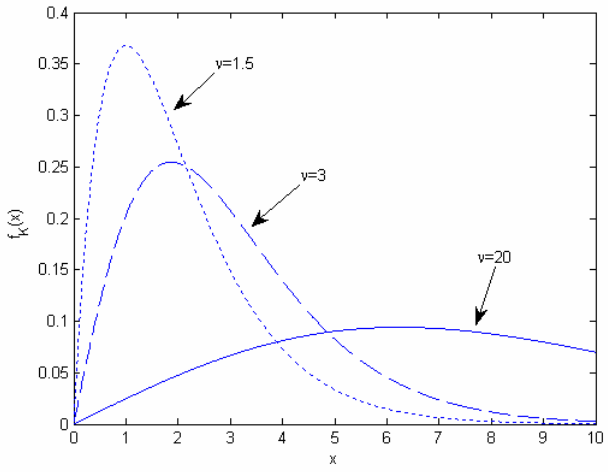

Figure 2.3 K-distribution probability density functions for various shape parameters $b = 1$.

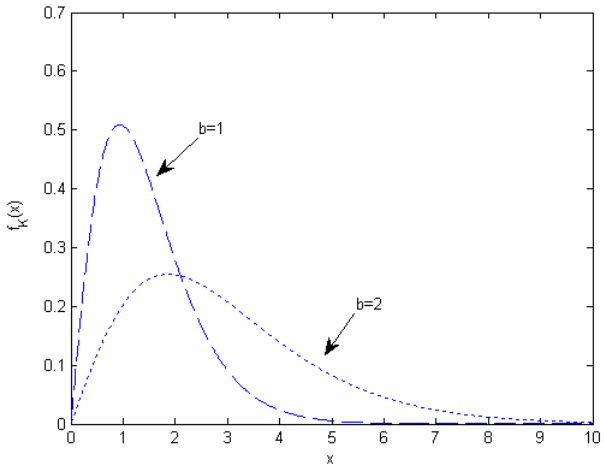

Figure 2.4 K-distribution probability density functions for various scale parameters $\nu = 3$.

Multi-pulse Representation

The modeling of the echoes obtained from multiple pulses with desired distribution function and correlation properties is a difficult task. In order to solve this problem, *Compound Gaussian Clutter Model* is proposed by Ward [60].

In compound Gaussian (product) model, complex clutter can be written as given in Equation (2.5). The speckle component accounts for the local scattering and is a fast-changing component. It is assumed to have complex Gaussian distribution with unit power. The texture component represents the variation of the local power. It is modeled as a real and nonnegative random process [64].

The compound-Gaussian model widely characterizes heavy-tailed distributions, which is a property of high-resolution radar clutter. It also has a physical justification for sea clutter [37].

Compound-Gaussian model belongs to the class of spherically invariant random processes [12].

In compound Gaussian model, the probability density function of the clutter is determined by the distribution of the texture component. The correlation properties are determined by the correlation of the elements that form the speckle component.

Compound-Gaussian is a convenient model due to its ease of mathematical analysis and the fact that it can represent a wide class of radar clutter types. The model has received great attention in literature. Similar to Weibull distribution, K-distribution can represent the earlier assumed Rayleigh distribution as a special case ($\nu \to \infty$).

Let the intensity, y, of the clutter signal be K-distributed [60]:

$$p_y(y) = \frac{2b}{\Gamma(\nu)} (\frac{b}{2} y)^{\nu} K_{\nu-1}(b\, y) \ , \tag{2.12}$$

where v is the shape parameter and b is a scale parameter. Then the texture parameter is gamma distributed:

$$p_\tau(\tau) = \frac{1}{\Gamma(\nu)} \left(\frac{\nu}{\mu} \right)^{\nu} \tau^{\nu-1} \exp(-\frac{\nu}{\mu} \tau) \ , \tag{2.13}$$

where ν is the order parameter and μ is the mean (mean of the clutter intensity).

Hence, the relation between the scale parameter of K-distribution and the mean and order parameter of the Gamma distribution can be given by

$$b \overset{\Delta}{=} 2\sqrt{\frac{\nu}{\mu}} \ . \tag{2.14}$$

2.3 Radar Detection

In radar systems, detection of targets in clutter is an important problem. The classical detection process is composed of three main steps. The clutter suppression, Doppler processing and then thresholding. In some cases, clutter suppression is performed separately as in the case of MTI (Moving Target Indication), or it is performed jointly with Doppler processing. In some cases, just the Doppler processing is sufficient to discriminate the desired echoes from the clutter signal in Doppler frequency. After suppression of the clutter and noise signals, the amplitude of the signal is obtained and a noncoherent operation is performed in order to set the threshold for detection.

A modern signal processing technique is to perform all of the interference suppression, Doppler processing and thresholding operations simultaneously.

Detailed information on these issues is given in the following sections.

2.3.1 Clutter Suppression and Doppler Processing

Clutter suppression and Doppler processing are spectral analysis methods that operate on the pulses received from a specified range bin. The operation is performed on each range bin. Doppler processing notation consisting of N pulses and M range bins are shown in Figure 2.5. The entries in each column correspond to pulse samples, which are separated by a Pulse Repetition Interval (PRI).

Classical clutter suppression methods are simple. They are also called pulse-cancellers. The simplest one is the two-pulse MTI canceller that subtracts echoes from successive pulses. The filtering simply forms a notch at DC and cancels out the stationary clutter component. However, this method performs poorly especially at low-radial velocity targets. Details of the operation can be found in [47] and [54].

Classical spectral analysis and Doppler frequency extraction is performed by means of Fourier transformation, i.e. Fast-Fourier Transformation (FFT). However, this operation corresponds to filtering that has high sidelobes in frequency. This fact causes contamination of target signals by the other targets at neighboring Doppler frequencies. In order to suppress the high side lobes and alleviate the contamination problem, commonly, a data window to weight the slow-time samples is used. On the other hand, the windowing operation, in turn, causes an increase in main lobe width and a decrease in peak amplitude and SNR.

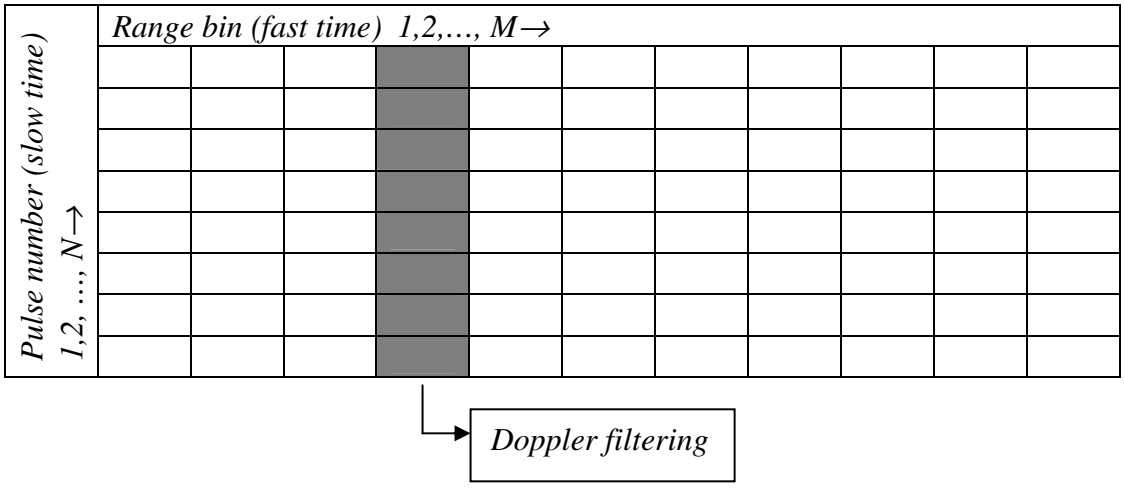

Figure 2.5 Two-dimensional matrix for Doppler filtering

A more effective canceller is the matched filter mentioned in [47], which is derived in the following part:

Let the input signal to the Doppler processing unit be

$$\begin{aligned} & r(k) = s(k) + i(k) \qquad k = 1, 2, \cdots, N \\ & \mathbf{r} \overset{\Delta}{=} [r(1)\ r(2) \cdots r(N)] \end{aligned} \quad . \tag{2.15}$$

Here, *s* and *i* represent the target and interference signals, respectively.

The optimal weights are obtained as

$$\mathbf{w} = \mathbf{M}_{\mathbf{i}}^{-1}\, \mathbf{p} \,. \tag{2.16}$$

The vector **p** represents the desired target signal or Doppler steering vector and is given by

$$\mathbf{p} \overset{\Delta}{=} \left[1 \quad e^{j\Omega} \quad \cdots \quad e^{j\Omega(N-1)}\right]^T . \tag{2.17}$$

$\mathbf{M}_{\mathbf{i}}$ is the covariance matrix of the interference, which is usually the sum of the covariance matrices of the clutter and noise. Ω is the Doppler frequency.

Then, the output, $\mathbf{z} \overset{\Delta}{=} [z(1)\ z(2) \cdots z(N)]$, is obtained as follows:

$$\mathbf{z} = \mathbf{w}^H \mathbf{r} \,. \tag{2.18}$$

This filter is also equivalent to MMSE or Wiener filter, which minimizes the mean squared error between its output and the target return. When the desired signal vector is deterministic, then the max-SIR or eigen-filter, which maximizes the signal to interference power ratio at its output, is also equivalent to this filter [16].

After the filtering operation, the amplitude or power of the signal is obtained.

2.3.2 Thresholding and CFAR

In classical systems, a target is declared if the signal power, obtained at the output of the Doppler processing unit, exceeds the threshold. The method is non-coherent as the operation is performed on the magnitude of the signal.

In modern radar systems, the threshold is determined adaptively. It is set in order to keep the false alarm rate constant by means of estimating the interference power. This operation is named as the *Constant False Alarm Rate* (CFAR) method [23], [47]. In order to keep the false alarm rate constant, the threshold is set according to the following relations for Rayleigh and Weibull clutters, respectively [1], [18], [47]:

$$P_{FA} = \exp(-T/\sigma), \tag{2.19}$$

$$P_{FA} = \exp(-(T/\alpha)^{\beta}). \tag{2.20}$$

Adaptive thresholding can be classified as spatial and temporal. In spatial methods, the threshold is determined by using the neighboring range cells. In temporal methods, the information gathered from the previous scans of the cell under test is used in determination of the threshold.

The performance is measured with probability of false alarm and probability of detection. Since the parameters are estimated using finite number of samples, a higher threshold is used and this causes a decrease in detection probability. This phenomenon is named as *CFAR Loss*.

Spatial Methods

In spatial methods, echoes from the adjacent range cells surrounding the cell under test are used. Assuming that these cells contain interference that has the same distribution and characteristics with the one in the cell under test, the distribution

parameters of the interference are estimated and the threshold is set according to Equation (2.19) and (2.20).

Performance of a spatial CFAR algorithm is measured according to the following criteria:

- Performance under homogeneous clutter condition
- Performance under non-homogeneous clutter condition
- Performance with interfering targets
- Computational complexity

The most common spatial CFAR methods for Rayleigh clutter are *Cell-Averaging CFAR* (CA-CFAR) and *Ordered-Statistics CFAR* (OS-CFAR). CA-CFAR method averages the amplitudes of the adjacent cells and uses this mean value, where OS-CFAR method performs ranking and chooses the k^{th} ordered sample in determination of the threshold. CA-CFAR is the optimum method for operation in homogeneous Rayleigh clutter. OS-CFAR is appropriate when there are multiple targets and outliers [50].

The variants of the cell-averaging method, Greater of CA (GO-CA) and Smaller of CA (SO-CA) algorithms use the greater and smaller of the mean values of the samples in the leading and lagging sub-windows. These algorithms are appropriate for operation with clutter edges and multiple targets, respectively.

In non-Rayleigh clutter conditions, the above-mentioned methods designed for Rayleigh clutter are not successful in keeping the false alarm constant. Thus, some other methods are proposed. These are maximum-likelihood CFAR [46], variability-index CFAR [55], ordered-statistics for Weibull [63], [35] and log-t detector [29].

Temporal Methods

Temporal methods are also named as *clutter-map CFAR* methods. In these methods, clutter-maps are employed in order to store and update the clutter information such as distribution parameters, e.g. the power in Rayleigh clutter. These techniques are advantageous in that they can operate in any non-homogeneous clutter condition such as clutter edges. The performance of a temporal CFAR algorithm is measured according to:

- Settling time
- Probability of detection and false alarm
- Self masking of the targets
- Computational complexity

Some of the temporal CFAR methods are proposed in [38].

There are other methods that combine the clutter suppression, Doppler processing and thresholding operations simultaneously [34], [49], [27]. These are optimal detectors and in this thesis, special emphasis is given on this type of detection.

CHAPTER 3

NONCOHERENT CLUTTER ESTIMATION

Estimation of the clutter statistical distribution parameters is an essential part of the detection problem. Besides, clutter distribution parameter estimates can be used in classification and discrimination in Synthetic Aperture Radar and other radar imagery systems.

It is known that Weibull distribution and K-distribution provide a good description of clutter amplitude in high-resolution radars. In this chapter, some important estimation methods for Weibull and K-distribution parameters are considered.

3.1 Weibull Parameter Estimation

The Weibull distribution accurately represents the clutter distribution over a wide range of conditions. The Weibull PDF is defined as below:

$$f_W(x) = \frac{\beta}{\alpha}\left(\frac{x}{\alpha}\right)^{\beta-1} \exp\left\{-(x/\alpha)^{\beta}\right\} U(x), \qquad \alpha, \beta > 0 \tag{3.1}$$

where α and β are the scale and shape parameters, respectively. U(·) is the unit-step function.

The distribution function is

$$F_W(x) = 1 - \exp\left\{-(x/\alpha)^{\beta}\right\}. \tag{3.2}$$

There exist many methods for estimation of Weibull shape and scale parameters. Generally, estimation of the Weibull PDF parameters is a difficult task, since they require plotting, iteration or sorting. The most important estimation methods are method of moments and maximum-likelihood method, which are explained in the following subsections.

3.1.1 Method of Moments

In this method, moments of the distribution that are defined as a function of the distribution parameters are equated to the sample moments, and the parameter estimates are obtained by solving these equations. This method and its derivatives can also be found in [65] and the references therein.

For Weibull distribution, the following equations show the first and second raw moments:

$$E[x] = \Gamma(1+1/\beta), \qquad E[x^2] = \Gamma(1+2/\beta). \tag{3.3}$$

The sample moments are obtained from

$$\mu_k = \frac{1}{n}\sum_{i=1}^{n} x_i^k \,. \tag{3.4}$$

Equating the sample moments to analytical moments,

$$\frac{\mu_2}{\mu_1^2} = \frac{n\sum_{i=1}^{n} x_i^{\,2}}{\left[\sum_{i=1}^{n} x_i\right]^2} = \frac{\Gamma(1+2/\hat{\beta})}{\left(\Gamma(1+1/\hat{\beta})\right)^2}. \tag{3.5}$$

is obtained, where n is the number of samples, x_i's are the received signal amplitudes. Here, $\Gamma(\cdot)$ represents the Gamma Function.

The shape parameter, β, can be found iteratively using the expression given by (3.5). Having obtained this estimate, α can be calculated using the equation given below:

$$\hat{\alpha} = \frac{\sum_{i=1}^{n} x_i}{n\,\Gamma\left[1+1/\hat{\beta}\right]}. \tag{3.6}$$

Similar operations can be performed to obtain the parameter estimates, using the central moments instead of the raw ones.

It can be seen that these operations are computationally costly. Some simplifications may be performed by means of modifying the estimation method. It is known that logarithm of a Weibull distributed variable has a location-scale type distribution. This distribution is named as Gumbel distribution and is a special case of the Extreme-Value or Fisher-Tippett distribution. Using this property, the following estimates are found [11], [53]:

$$\hat{\alpha} = \exp\left\{\frac{1}{N}\sum_{i=1}^{N}\ln x_i + 0.5772\,\hat{\beta}^{-1}\right\}, \tag{3.7}$$

$$\hat{\beta} = \left\{\frac{6}{\pi^2}\frac{N}{N-1}\left[\frac{1}{N}\sum_{i=1}^{N}(\ln x_i)^2 - \left(\frac{1}{N}\sum_{i=1}^{N}\ln x_i\right)^2\right]\right\}^{-1/2}. \tag{3.8}$$

These estimators are rather simple and do not require iteration. However, they are suboptimal.

3.1.2 Maximum-Likelihood Estimation

It is known that the maximum likelihood estimates [33], [59] are the ones, which satisfy

$$\theta = \arg\max_{\theta} p(x|\theta), \tag{3.9}$$

where $\theta = [\alpha \quad \beta]^T$.

Maximizing the likelihood function given by (3.9) is equivalent to maximizing its logarithm, which is given as

$$\ln f_W(x) = \ln\beta - \beta\ln\alpha + (\beta-1)\ln(x) - x^{\beta}\alpha^{-\beta}. \tag{3.10}$$

For independent n samples, $\mathbf{x} \overset{\Delta}{=} \{x_i\}_{i=1}^n$, this function is

$$\ln f_W(\mathbf{x}) = \sum_{i=1}^{n} \ln f_W(x_i) = n\ln\beta - n\beta\ln\alpha + (\beta-1)\sum_{i=1}^{n}\ln x_i - \sum_{i=1}^{n} x_i^{\beta}\alpha^{-\beta}. \tag{3.11}$$

The partial derivatives of the function, which will be equated to zero in order to obtain the estimates, are found as

$$\frac{\partial}{\partial\alpha} f_W(x) = -n\beta\frac{1}{\alpha} + \beta\alpha^{-\beta-1}\sum_{i=1}^{n} x_i^{\beta}, \tag{3.12}$$

$$\frac{\partial}{\partial\beta} f_W(x) = \frac{n}{\beta} - n\ln\alpha + \sum_{i=1}^{n}\ln x_i - \sum_{i=1}^{n}\left(\frac{x_i}{\alpha}\right)^{\beta}\ln\left(\frac{x_i}{\alpha}\right). \tag{3.13}$$

Equating these expressions to zero, the estimates are obtained as given below. These results were also derived in [46].

$$\hat{\alpha}^{\hat{\beta}} = \frac{1}{n}\sum_{i=1}^{n} x_i^{\hat{\beta}}, \tag{3.14}$$

$$\hat{\beta} = \left(\frac{\sum_{i=1}^{n} x_i^{\hat{\beta}} \ln x_i}{\sum_{i=1}^{n} x_i^{\hat{\beta}}} - \frac{1}{n}\sum_{i=1}^{n} \ln x_i \right)^{-1}. \tag{3.15}$$

Having obtained the estimate $\hat{\beta}$, $\hat{\alpha}$ can be obtained easily using Equation (3.14). However, solution of Equation (3.15) is not trivial. At this point, some iterative methods should be utilized.

3.2 K-Distribution Parameter Estimation

K-distribution is described by the following probability density function:

$$f_K(x) = \frac{2b}{\Gamma(\nu)}\left(\frac{bx}{2}\right)^{\nu} K_{\nu-1}(bx)\,U(x), \qquad \nu > 0, \tag{3.16}$$

where $\Gamma(\cdot)$ is the Gamma function, $K_\nu(\cdot)$ is the modified Bessel function of order ν and b is a positive constant as defined before.

The distribution function is

$$F_K(x) = 1 - \frac{2}{\Gamma(\nu)}\left(\frac{bx}{2}\right)^{\nu} K_{\nu}(bx)\,U(x), \qquad \nu > 0. \tag{3.17}$$

The next two subsections describe the method of moments and maximum likelihood estimation methods. There are some other methods that can be found in [7] and [44].

3.2.1 Method of Moments

The moments of the K-distribution are expressed as follows [32]:

$$E\left[x^k\right]=\frac{\Gamma(0.5k+1)\,\Gamma(\nu+0.5k)}{\Gamma(\nu)}\left(\frac{2}{b}\right)^k. \tag{3.18}$$

The sample moments are obtained from

$$\mu_k=\frac{1}{n}\sum_{i=1}^{n}x_i^k. \tag{3.19}$$

The mean and the variance of the distribution are

$$\begin{aligned} E\left[x\right]&=\frac{\Gamma(1.5)\,\Gamma(\nu+0.5)}{\Gamma(\nu)}\frac{2}{b}\\ E\left[x^2\right]&=\frac{4}{b^2}\nu \end{aligned}. \tag{3.20}$$

Finding the parameters using Equations (3.20) requires solution of nonlinear equations. It is stated that for spiky radar clutter, higher order moments can be used [32]:

$$\nu=\frac{2}{\frac{\mu_4}{\mu_2^2}-2}. \tag{3.21}$$

After this, using the first order moment, the parameter b can be obtained using

$$b=\frac{\sqrt{\pi}\,\Gamma(\nu+0.5)}{\mu_1\,\Gamma(\nu)}. \tag{3.22}$$

3.2.2 Maximum-Likelihood Estimation

The maximum likelihood estimates can be obtained by maximizing the log-likelihood function defined by

$$\ln f_K(\mathbf{x}) = \sum_{i=1}^{n} \ln p_K(x_i) = n \ln\left(\frac{2b}{\Gamma(\nu)}\right) + \nu \sum_{i=1}^{n} \ln\left(\frac{b\,x_i}{2}\right) + \sum_{i=1}^{n} \ln\left[K_{\nu-1}(b\,x_i)\right]. \quad (3.23)$$

Taking the derivative with respect to the unknown parameters,

$$\frac{\partial}{\partial b} \ln f_K(x) = (1+\nu)\,\frac{n}{b} + \sum_{i=1}^{n} \frac{\frac{\partial}{\partial b} K_{\nu-1}(b\,x_i)}{K_{\nu-1}(b\,x_i)} \quad (3.24)$$

$$\frac{\partial}{\partial \nu} \ln f_K(x) = -n\left[\ln\left(\frac{2}{b}\right) + \Psi(\nu)\right] + \sum_{i=1}^{n} \ln(x_i) + \sum_{i=1}^{n} \frac{\frac{\partial}{\partial \nu} K_{\nu-1}(bx_i)}{K_{\nu-1}(bx_i)} \quad (3.25)$$

are obtained, where $\Psi(\cdot)$ is the digamma function given by

$$\Psi(u) = \frac{d}{du}\left[\ln \Gamma(u)\right] = \frac{\Gamma'(u)}{\Gamma(u)}. \quad (3.26)$$

The solution of the equations, obtained after equating these expressions to zero, requires nonlinear methods. In their work, Iskander et al [31] obtained the following estimate for the parameter *b*:

$$\hat{b} = \left(\frac{1}{2}\exp\left(\frac{\gamma_e - \Psi(\hat{\nu})}{2} + \frac{1}{n}\sum_{i=1}^{n} \ln(x_i)\right)\right)^{-1}, \quad (3.27)$$

where, γ_e is the Euler constant.

CHAPTER 4

NONCOHERENT THRESHOLDING

In classical radar detection, after clutter suppression and Doppler processing, the signal is envelope or square-law detected. Following this, a noncoherent CFAR operation is performed to set the threshold in order to keep the false alarm rate constant.

One of the most important problems that a thresholding operation must deal with is heterogeneity in interference characteristics. Many CFAR detectors for Weibull clutter [46], [53], [63] or range-heterogeneous Rayleigh clutter [9], [23], [25], [47] have been suggested before. However, both of the problems are not handled simultaneously. In this part of the study, three CFAR methods that are suitable for non-Rayleigh and range-heterogeneous clutter are designed.

The first method, *Goodness-of-Fit (GoF) CFAR*, firstly, determines the heterogeneity using a goodness-of-fit test. If it is decided to be heterogeneous, it estimates the position of the transition point and the distribution parameters of the clutter in the cell under test. The second method, *Expectation-Maximization (EM) CFAR*, uses Expectation-Maximization algorithm to identify the heterogeneous segments and determine their distribution parameters. The final method, named as *Clutter-Map (CM) CFAR* forms a map to store the distribution parameters and by this way, uses the information obtained from the previous radar scans. The final method is well suited to land-based radars, where the clutter parameters do not change significantly in time. In all of the methods, clutter distribution is assumed to be Weibull. The scale

and shape parameters of the distribution are assumed to be unknown, thus exact information on the shape parameter is not required.

4.1 Clutter Model

In this study, the range heterogeneity of the Weibull clutter is modeled as a sharp transition from one region to another with a different PDF scale and/or shape parameter. This model is general and suitable for clutter interfaces such as land to sea. Similar to the one made in similar works, the clutter is assumed to be dominant and the effect of thermal noise is neglected.

The heterogeneity scenario is illustrated in Figure 4.1. The transition represents a change in distribution parameters. Here, **x** is the observation vector, $f_{\mathbf{x}}(\mathbf{x}, \alpha_1, \beta_1)$ is the probability density function of the first clutter region and $f_{\mathbf{x}}(\mathbf{x}, \alpha_2, \beta_2)$ is the one of the second one. Parameters α_1, β_1 and α_2, β_2 represent the distribution parameters of region 1 and 2, respectively. The horizontal axis shows the range, through which the samples that form the observation vector, **x**, are obtained.

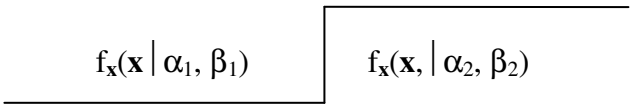

Figure 4.1 Clutter heterogeneity, PDF transition from $f_{\mathbf{x}}(\mathbf{x}, \alpha_1, \beta_1)$ to $f_{\mathbf{x}}(\mathbf{x}, \alpha_2, \beta_2)$

4.2 Goodness-of-Fit CFAR

Goodness-of-Fit CFAR method, firstly tests the heterogeneity of the window under test. If the window is found to be heterogeneous, the position of the transition point and the distribution parameters of the regions are estimated. Having determined the

transition point and the parameters, the threshold is set so as to yield the desired false alarm rate.

It is known that some methods designed for range-heterogeneous clutter may perform poorly when the clutter is homogeneous. This algorithm does not have this problem, as the test homogeneity situation is tested. If the data stemming from the clutter range is found to be homogeneous, threshold setting is done accordingly.

Assuming that the window is homogeneous, the shape and the scale parameters of the distribution are estimated using the method mentioned in [53]. This method is easy to implement and its performance is close to the Maximum Likelihood estimation, which requires iteration in Weibull case. Let the sample vector that will be used in estimation, obtained after discarding the cell under test and the guard cells, be $\mathbf{x} = [x_1 \; x_2 \cdots x_N]$. Then, the shape, β, and scale, α, parameters are estimated using the samples that form the CFAR window, using the formulas below:

$$\hat{\beta} = \left\{ \frac{6}{\pi^2} \frac{N}{N-1} \left[\frac{1}{N} \sum_{i=1}^{N} (\ln x_i)^2 - \left(\frac{1}{N} \sum_{i=1}^{N} \ln x_i \right)^2 \right] \right\}^{-1/2}, \tag{4.1}$$

$$\hat{\alpha} = \exp\left\{ \frac{1}{N} \sum_{i=1}^{N} \ln x_i + 0.5772 \; \hat{\beta}^{-1} \right\}. \tag{4.2}$$

Having obtained the estimates, a Weibull PDF goodness-of-fit test is performed. Anderson-Darling Goodness-of-fit test [3] for Weibull distribution is chosen here, as it is claimed to be more sensitive than the classical methods in the tail of the distribution. The test is defined as follows [22]:

$$A^2 = -N - \frac{1}{N} \sum_{i=1}^{N} (2i-1)\left[\ln(w_i) + \ln(1 - w_{n-i+1}) \right], \tag{4.3}$$

where

$$w_i = F(q_i) = 1 - \exp(-(\frac{q_i}{\hat{\alpha}})^{\hat{\beta}}) . \quad (4.4)$$

Here, q_i's are the ordered samples obtained by sorting x_i's in ascending order.

The test statistic is compared to a predetermined critical value given in [22], for various levels of significance. The level of significance is defined as the probability of committing a Type 1 error. In other words, for this case, it is the probability of deciding that the observation set is heterogeneous, while actually it is homogeneous. If the test statistic is smaller than the critical value, then it is decided that the distribution fits Weibull and the observations are from a homogeneous set.

$$A^2 \underset{H_0}{\overset{H_1}{>}} A^2_{crit} . \quad (4.5)$$

Critical values change with the number of samples used. The values used here which are given in Table 4.1 are valid for number of observation samples greater than 50. In this study, the significance level is chosen to be 0.01.

Table 4.1 Anderson-Darling Goodness-of-Fit Test Critical Values

Significance	0.1	0.05	0.025	0.01
A^2_{crit}	0.637	0.757	0.877	1.038

If the observation set is found to be heterogeneous, the transition position should be estimated in order to identify the different homogeneous regions. In estimation of the transition position, maximum-likelihood approach is used.

Using the independence of the Weibull distributed samples in the observation vector, the likelihood of the transition point to be at the m th position, is obtained as

$$L_m(\mathbf{x},\hat{\alpha}_1,\hat{\beta}_1,\hat{\alpha}_2,\hat{\beta}_2)=\prod_{i=1}^{m}\frac{\hat{\beta}_1}{\hat{\alpha}_1}\left(\frac{x_i}{\hat{\alpha}_1}\right)^{\hat{\beta}_1-1}\exp\left\{-\left(x_i/\hat{\alpha}_1\right)^{\hat{\beta}_1}\right\}\times \prod_{i=m+1}^{N}\frac{\hat{\beta}_2}{\hat{\alpha}_2}\left(\frac{x_i}{\hat{\alpha}_2}\right)^{\hat{\beta}_2-1}\exp\left\{-\left(x_i/\hat{\alpha}_2\right)^{\hat{\beta}_2}\right\}, \tag{4.6}$$

where $\hat{\alpha}_1,\hat{\beta}_1$ and $\hat{\alpha}_2,\hat{\beta}_2$ are the estimates obtained from the two observation vectors (vectors that are formed by the samples to the left and right of m), respectively. These estimates can be found using Equations (4.1) and (4.2) for each value of m.

The transition point, M, is declared to be the position m that maximizes the likelihood function:

$$M=\arg\max_m L_m(\mathbf{x},\hat{\alpha}_1,\hat{\beta}_1,\hat{\alpha}_2,\hat{\beta}_2). \tag{4.7}$$

If the parameters of the distribution are known exactly, then the detection threshold, T, can be easily set as

$$T=\alpha\left(-\ln P_{FA}\right)^{1/\beta} \tag{4.8}$$

However, the parameters that are used in the test are not exactly known but they are estimated using a limited number of samples making the actual false alarm rate different from the desired one. As the estimates are random variables, so is the false

alarm probability. Due to this fact, the threshold can be set to make the expected value of this false alarm probability equal to the desired one:

$$E\{P_{FA}'\} = E\{\exp[-(T'/\alpha)^{\beta}]\} = P_{FA}\,. \tag{4.9}$$

Next, a coefficient q is found to set the threshold as $T' \stackrel{\Delta}{=} q^{1/\hat{\beta}}\hat{\alpha}$, with the purpose of simplifying the operation. Unfortunately, when the shape parameter of Weibull distribution is not known but estimated, a closed form expression for the distribution of P_{FA} cannot be obtained. Thus, the parameter q can be found using Monte-Carlo simulations to yield the desired false alarm probability. Since the desired values are small, it is necessary to perform a large number of simulations. In our case, a closed form expression for P_{FA}, in terms of the estimated parameters, exists and simulation is required only to find the parameter estimates. After the simulation performed to find the estimates, P_{FA} can be calculated analytically. This greatly reduces the sufficient number of simulations.

In this work, for $P_{FA}=10^{-5}$, the coefficients are found for various number of samples. The threshold values for different number of samples are given in Figure 4.2. It is verified that as the number of samples increases, the value approaches to $-ln\ P_{FA}$. Figure 4.3 shows the change of the threshold parameter with false alarm probability and number of samples used in estimation. Threshold parameters are determined by this method and are tabulated. Then these parameters are used in setting the threshold to yield the desired value of the mean probability of false alarm.

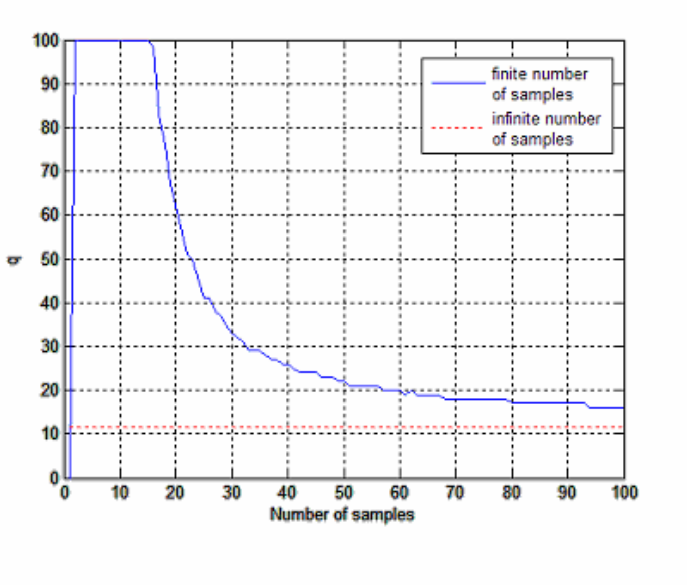

Figure 4.2 Threshold parameter for Weibull distribution versus different number of samples, $P_{FA} = 10^{-5}$

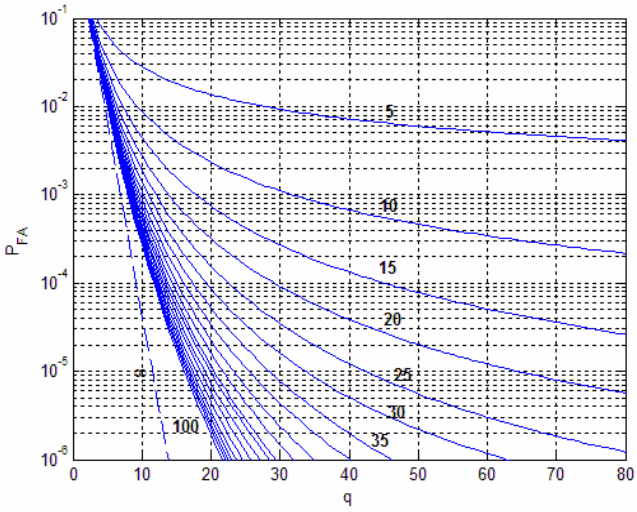

Figure 4.3 Probability of false alarm versus threshold parameter for Weibull distribution for different number of samples

A target is declared if the signal amplitude in the *Cell Under Test* (CUT) is greater than the threshold:

$$CUT = y_{N/2+1} > T \tag{4.10}$$

In order to determine the threshold parameter, T, the region of the cell under test is identified. It is decided that the target is in the first region if the transition point index is smaller than $N / 2$. Otherwise the threshold is set according to the second region distribution parameters. For the first region, the threshold is $T = q_M{}^{1/\hat{\beta}_1}\hat{\alpha}_1$; and for the second one, it is $T = q_{N-M}{}^{1/\hat{\beta}_2}\hat{\alpha}_2$.

Next, performance of the Goodness-of-Fit CFAR is presented. Performance evaluation is done using Monte Carlo simulations. The simulations are executed at 50000 points and then averaging is performed.

The first result, presented in Table 4.2, is on the capability of the goodness-of-fit test in homogeneous/heterogeneous region identification. The whole observation vector is divided into 8 segments each of which are composed of 100 samples. The transition occurs in the 4th segment, for which a high test-statistics is found by using the goodness-of-fit test. This high-statistics exceeds the critical value and that segment is declared to be heterogeneous.

Next, performance of transition point estimation using Equation (4.7) is presented. Figure 4.4 shows the performance of finding the correct position of the transition. The two segments differ in scale parameters, i.e. SCR (Signal-to-Clutter power Ratio) values and shape parameters. Here, the signal (target) is kept at unit power and the clutter power is determined accordingly. The target experiences a Swerling-1 type fluctuation. As it can be seen in the figure, the estimation performance is poor when the transition point is close to the beginning of the range. The reason for this is that the parameter estimation degrades at that point, since the number of samples to the left of the window is not sufficient. Performance degradation at the end of the

range is not that much, in view of the fact that the clutter is less spiky and the estimator performance is better at the second region. A remedy for the estimation in end points is using a sliding window and work on the range samples within this window. By this way, each range sample will be covered and the parameter of each sample will be estimated successfully.

Table 4.2 Anderson-Darling GoF Test performance in heterogeneity identification
α changes from 5 to 1, β changes from 1.5 to 2

Segment index	**Parameter estimates**		**Test statistics**	**Fit**
	α	**β**		
1	4.92	1.54	0.35	1
2	5.27	1.39	0.48	1
3	4.92	1.46	0.35	1
4	**1.93**	**1.29**	**14.58**	**0**
5	0.99	1.88	0.21	1
6	0.98	2.01	0.30	1
7	0.95	2.11	0.26	1
8	1.01	2.01	0.27	1

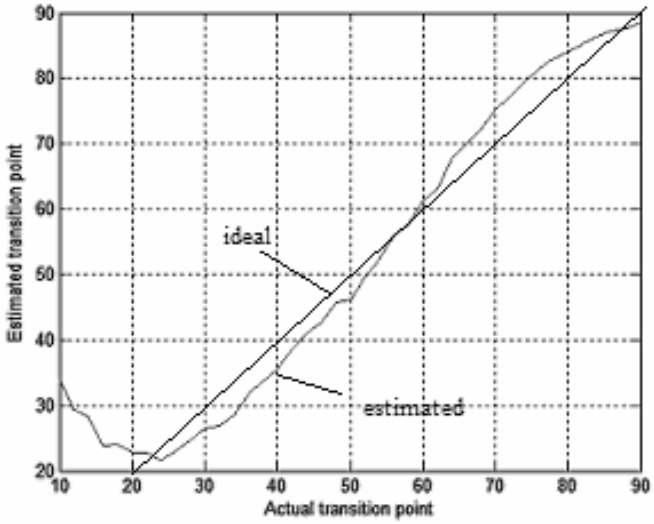

Figure 4.4 GoF-CFAR, performance of transition point estimation
SCR_1 = 20dB, SCR_2 = 30dB; β_1=1, β_2=2

Figure 4.5 shows the detection probability versus signal to clutter power ratio for different shape parameter values, in homogeneous clutter. The dotted lines show the performance that can be obtained by the exact knowledge of parameters. Difference between the solid and dotted curves shows the CFAR loss. Due to the quality of estimation obtained with 800 samples, the loss is negligible. As expected, the performance deteriorates with decreasing shape parameter (β), which means more spikiness. Spiky clutter causes an increase in the threshold, which, in turn, causes a reduction in false alarm probability.

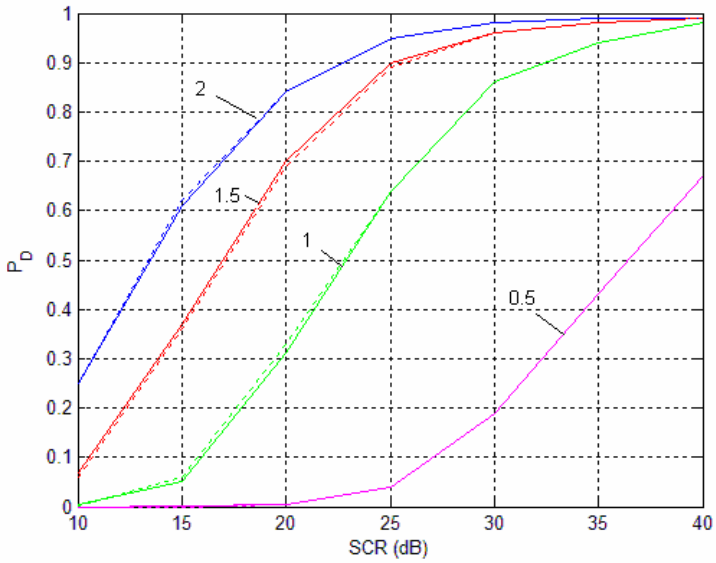

Figure 4.5 GoF-CFAR, probability of detection versus SCR in homogeneous clutter for various shape parameters.

$P_{FA} = 10^{-5}$. Range-heterogeneous CFAR (solid curves), ideal thresholding (dotted curves)

It is known that when conventional CFAR methods are operated in Weibull clutter, false alarm rate increases due to clutter spikes. Together with this effect, the

performance under range-heterogeneous clutter is analyzed. Two of the classical methods, Greatest-of-Cell-Averaging (GO-CA) and Ordered-Statistics (OS) CFAR methods, which are known to be suitable for heterogeneous Rayleigh clutter are compared with the proposed method in a heterogeneous Weibull clutter environment. The number of samples used in estimation is 100. The result is illustrated in Figure 4.6. The two methods are unable to perform well in this situation, since the clutter distribution deviates from Rayleigh and becomes spikier in the second region. GoF-CFAR does not suffer from false alarms and yields a threshold close to the ideal threshold at the transition point.

Performance of the proposed method is also compared with ML algorithm for Weibull clutter. This method calculates the Maximum-Likelihood parameter estimates to set the threshold. In spite of its computational complexity, this method has good performance in a homogeneous Weibull clutter environment. However, in a heterogeneous environment, the existence of the transition region causes erroneous estimation and the method yields target masking at the low-power clutter region. The performance analysis result is shown by Figure 4.7. At the homogeneous parts, the ML method performs well. The conventional methods experience either target masking or excessive false alarms at the clutter edge. As it can be seen, GoF-CFAR enables the detection of the target, which is very close to the clutter edge. At the second region, where the shape parameter is 2 and the Weibull PDF is identical to Rayleigh PDF, all of the methods generate almost the same threshold and perform similarly.

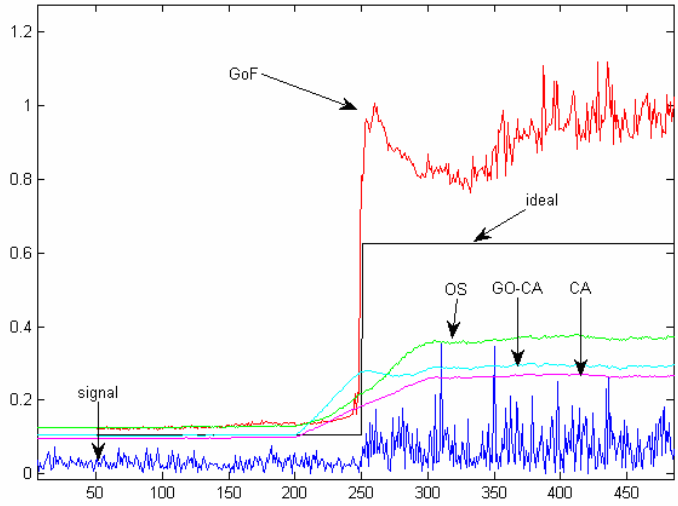

Figure 4.6 GoF-CFAR, signal variation in range-heterogeneous clutter and threshold levels for various CFAR methods – no target

$P_{FA} = 10^{-5}$, no target, $\beta_1=2$, $\beta_2=1.2$, 20 simulations

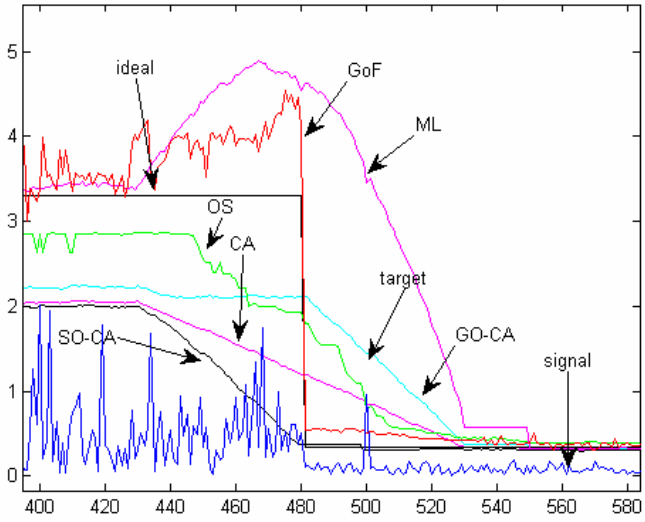

Figure 4.7 Amplitude variation with range of range-heterogeneous clutter and threshold levels for various CFAR methods - target

$P_{FA} = 10^{-5}$, $SCR_1 = 3dB$, $SCR_2 = 20dB$; $\beta_1=1.5$, $\beta_2=2$, 20 simulations

The detection probabilities in heterogeneous clutter, obtained with various methods are given in Table 4.3 through Table 4.5 The results are obtained via Monte-Carlo simulations. In the analysis, there exists 100 samples (range cells) and transition occurs at the 40^{th} range cell. The target is located at the 50^{th} range cell. The number of simulations is 20000. The thresholds are set so as to keep the false alarm rate at 10^{-5}. Table 4.3 shows the probability of detection in homogeneous clutter. The algorithms designed for range-heterogeneous clutter may cause some performance loss in homogeneous clutter environment. As it can be seen, when that shape parameter is 2, the clutter becomes Rayleigh distributed and the CA-CFAR algorithm is optimum. The ML algorithm also determines the parameters correctly and performs very well. In this case, as expected, OS algorithm performs well, too. When the shape parameter decreases, which means more spikiness, CA-CFAR has a drastic performance loss, especially in low SCR case. In this case, the loss of OS-CFAR is smaller. GoF CFAR performs close to the ML algorithm in high SCR scenario. However, some loss is observed when the SCR is low. This loss is due to the errors of detecting transitions while the environment is homogeneous.

Table 4.3 GoF-CFAR, probability of detection in homogeneous case

SCR(dB)	β	Ideal	GoF	ML	CA	OS
40	2	0.99	0.99	0.99	0.99	0.99
40	1	0.99	0.99	0.99	0.98	0.98
30	1	0.93	0.86	0.93	0.88	0.92
20	1	0.53	0.32	0.52	0.30	0.43

Table 4.4 shows the probability of detection in heterogeneous clutter, where the shape parameter changes. In this case, CA and OS-CFAR algorithms have a drastic loss in detection probability. The ML algorithm still performs well in this case, where the SCR is kept constant. GoF algorithm performs better than the ML algorithm when the SCR is high; however it performs worse in low SCR case.

Detection performance, when both the SCR and shape parameter change, is shown in Table 4.5. GoF CFAR performance is the one that is closest to the ideal performance. The loss of the ML algorithm is higher when the SCR gets lower. OS and CA algorithms yield lower detection probabilities when the shape parameter and/or the SCR decrease.

Table 4.4 GoF-CFAR, probability of detection in non-homogeneous case- Same SCR, different shape parameters

$SCR_1 \rightarrow SCR_2$	$\beta_1 \rightarrow \beta_2$	Ideal	GoF	ML	CA	OS
40→40	2→1.5	0.99	0.99	0.99	0.98	0.98
40→40	1→2	0.99	0.99	0.98	0.98	0.98
40→40	1→1.5	0.99	0.99	0.98	0.98	0.98
30→30	2→1.5	0.97	0.96	0.98	0.84	0.88
30→30	1→2	0.98	0.94	0.97	0.85	0.89
30→30	1→1.5	0.97	0.93	0.96	0.85	0.89
20→20	2→1.5	0.80	0.75	0.84	0.18	0.30
20→20	1→2	0.89	0.66	0.76	0.19	0.33
20→20	1→1.5	0.81	0.52	0.70	0.22	0.36

Table 4.5 GoF-CFAR, probability of detection in non-homogeneous case- Different SCR, different shape parameters

$SCR_1 \rightarrow SCR_2$	$\beta_1 \rightarrow \beta_2$	Ideal	GoF	ML	CA	OS
40→30	2→1.5	0.97	0.96	0.97	0.91	0.94
40→30	1→2	0.99	0.92	0.96	0.89	0.94
40→30	1→1.5	0.97	0.89	0.95	0.90	0.94
40→20	2→1.5	0.81	0.62	0.55	0.41	0.62
40→20	1→2	0.89	0.78	0.32	0.32	0.59
40→20	1→1.5	0.81	0.38	0.31	0.42	0.63
20→30	2→1.5	0.97	0.84	0.82	0.50	0.63
20→30	1→2	0.99	0.96	0.81	0.72	0.70
20→30	1→1.5	0.97	0.87	0.76	0.70	0.71

Part of this work was presented in [17].

Due to its disadvantages in Weibull and heterogeneous clutter environment, the OS-CFAR method is not recommended. On the other hand, it is known that it has some advantages such as decreasing masking effect in multiple-target situation. Using the approach of OS that eliminates the outliers, an improvement can be obtained in the proposed method in multiple-target case.

4.3 Expectation-Maximization CFAR

The second method that is proposed for range-heterogeneous Weibull clutter uses the Expectation-Maximization algorithm [39] in determination of the differing regions and estimation of the distribution parameters of clutter in these regions.

This method assumes that the sample vector under test is formed by a mixture of signals with different distribution parameters. Adopting this model, the problem can be viewed as the *problem of finite mixture distributions* [58]. Here, the aim is to estimate the occurrence probability of each distribution and the parameters of them. The algorithm starts with initial values for the distribution parameters and the a-priori PDF of each distribution. Then, using the observation signal, a-posteriori probabilities of each sample having each distribution is calculated. By choosing the maximum of these probabilities, the distribution estimate of each sample is obtained. Then, using this information, distribution parameters are re-estimated. These steps are performed iteratively to obtain the final decision on distributions of each sample and the distribution parameters. This information is then used in determination of transition and the detection threshold. Using this approach, Streit, et al., have performed the transient signal detection for exponential distributed random signals [57]. Following this, Chen, et al., employed this method in radar CFAR analysis [9]. However, as mentioned above, these studies were performed on exponential distribution, which was the classical assumption for the distribution of magnitude squared Gaussian signal. In this study, the method is extended to non-Gaussian, Weibull-amplitude signal.

Part of this work was presented in [19].

This work consists of two parts: Design of the two level and multi-level algorithms. In the design of the former algorithm, existence of two different distributions is assumed. In the latter one, the multi-level algorithm, the derivations for two-level algorithm are generalized to cover more than two distributions. The motivation in the design of the second method is simplifying the operation by means of eliminating the need for estimation of the shape parameter of the Weibull distribution.

4.3.1 Two-Level Algorithm

Similar to the symbolic illustration used in the previous section, range heterogeneity is modeled as shown in Figure 4.8. Here, **x** is the observation vector, $f_{\mathbf{x}}(\mathbf{x}, \alpha_1, \beta_1)$ is the probability density function of the first clutter region and $f_{\mathbf{x}}(\mathbf{x}, \alpha_2, \beta_2)$ is the one of the second region. Hidden random variables, Z_i, are introduced here, which associate each of the range samples x_i with one of the two distributions.

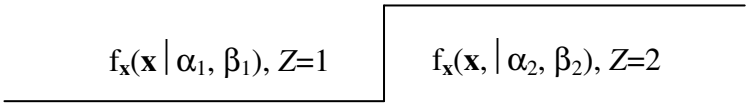

Figure 4.8 Clutter heterogeneity, PDF transition from $f_{\mathbf{x}}(\mathbf{x}, \alpha_1, \beta_1)$ to $f_{\mathbf{x}}(\mathbf{x}, \alpha_2, \beta_2)$

The a-priori probabilities of a sample having the distributions 1 and 2, i.e. Z_i=1 and 2 are given by

$$P[Z=1] = 1-q, \quad P[Z=2] = q\,. \tag{4.11}$$

Since, it is assumed that there are two distributions, Z has a binomial distribution.

Seeing that the observations depend on a hidden random variable, they are not complete and without the knowledge of Z_i's, i.e. the transition point, the maximum-likelihood estimates of the distribution parameters can not be performed. In this case, the Expectation Maximization algorithm can be employed. It is known that EM algorithm is an efficient computational procedure for maximum-likelihood estimation, where observations are incomplete.

EM algorithm is performed by iteration of two steps, E and M:

***E-Step**:* Form the expectation

Let the test parameters and the initial (guessed) parameters at the beginning of the iteration be represented by $\boldsymbol{\theta} = [\alpha_1\ \beta_1\ \alpha_2\ \beta_2\ q]^T$ and $\boldsymbol{\theta}' = [\alpha_1'\ \beta_1'\ \alpha_2'\ \beta_2'\ q']^T$, respectively. $\omega_i(c, x_i, \boldsymbol{\theta}') \stackrel{\Delta}{=} P(Z_i = c | \boldsymbol{\theta}', x_i)$ is the a-posterior probability of Z being c for the i^{th} range cell given the observation x_i and the assumed distribution parameters $\boldsymbol{\theta}'$.

Then the expectation function is

$$Q(\mathbf{x}, \boldsymbol{\theta}, \boldsymbol{\theta}') = \sum_{Z=1}^{2} \ln p_{\mathbf{x}}(\mathbf{x}|Z, \boldsymbol{\theta})\ P_Z(Z|\mathbf{x}, \boldsymbol{\theta}')\,. \tag{4.12}$$

***M-Step**:* Maximize the expectation

$$\boldsymbol{\theta}^* = \arg\max_{\boldsymbol{\theta}} Q(\mathbf{x}, \boldsymbol{\theta}, \boldsymbol{\theta}')\,. \tag{4.13}$$

At the end of each iteration, $\boldsymbol{\theta}'$ is replaced by $\boldsymbol{\theta}^*$**.** The algorithm is known to be convergent at least to a local maximum of the likelihood function $p_{\mathbf{x}|\boldsymbol{\theta}}(\mathbf{x}|\boldsymbol{\theta})$, if it is bounded [9]. The stopping criterion for the iterations can be a predefined small difference between the estimates of consecutive iterations.

For Weibull distribution, the algorithm can be derived as follows:

The expectation function can be written as

$$Q(\mathbf{x}, \boldsymbol{\theta}, \boldsymbol{\theta}') = \sum_{Z} \ln p_{\mathbf{x}|Z,\boldsymbol{\theta}}(\mathbf{x}|Z, \boldsymbol{\theta}) P(Z|\mathbf{x}, \boldsymbol{\theta}') \tag{4.14}$$

$$= \ln p_{\mathbf{x}|Z,\boldsymbol{\theta}}(\mathbf{x}|Z=1, \boldsymbol{\theta}) P(Z=1|\mathbf{x}, \boldsymbol{\theta}') + \ln p_{\mathbf{x}|Z,\boldsymbol{\theta}}(\mathbf{x}|Z=2, \boldsymbol{\theta}) P(Z=2|\mathbf{x}, \boldsymbol{\theta}')$$

Noting that for N range samples, which are statistically independent,

$$\ln p_{\mathbf{x}|Z,\boldsymbol{\theta}}(\mathbf{x}|Z=c,\boldsymbol{\theta}) = \sum_{i=1}^{N} \ln p_x(x_i|Z_i=c,\boldsymbol{\theta}) \ , \tag{4.15}$$

the expectation function can be written as

$$\begin{aligned} Q(\mathbf{x},\boldsymbol{\theta},\boldsymbol{\theta}') = \sum_{i=1}^{N} & \ln p_x(x_i|Z_i=1,\boldsymbol{\theta})\ \omega_i(Z_i=1,x_i,\boldsymbol{\theta}') \\ & + \ln p_x(x_i|Z_i=2,\boldsymbol{\theta})\ \omega_i(Z_i=2,x_i,\boldsymbol{\theta}') \end{aligned} . \tag{4.16}$$

For the Weibull density function, the cost function becomes

$$\begin{aligned} Q(\mathbf{x},\boldsymbol{\theta},\boldsymbol{\theta}') = \sum_{i=1}^{N} & [\ln(1-q) + \ln\beta_1 - \beta_1 \ln\alpha_1 + (\beta_1 - 1)\ln x_i - (x_i/\alpha_1)^{\beta_1}]\ \omega_i(1,x_i,\boldsymbol{\theta}') \\ & + [\ln(q) + \ln\beta_2 - \beta_2 \ln\alpha_2 + (\beta_2 - 1)\ln x_i - (x_i/\alpha_2)^{\beta_2}]\ \omega_i(2,x_i,\boldsymbol{\theta}') \end{aligned} . \tag{4,17}$$

The a-posterior probabilities are written as

$$\begin{aligned} \omega_i(1,x_i,\boldsymbol{\theta}') = P(Z_i=1|x_i,\boldsymbol{\theta}') &= \frac{P(Z_i=1)\ P(x_i,\boldsymbol{\theta}'|Z_i=1)}{P(x_i,\boldsymbol{\theta}')} \\ &= \frac{(1-q')\beta_1'\alpha_1'^{-\beta_1'} x_i^{\beta_1'-1} \exp\{-(x_i/\alpha_1')^{\beta_1'}\}}{(1-q')\beta_1'\alpha_1'^{-\beta_1'} x_i^{\beta_1'-1} \exp\{-(x_i/\alpha_1')^{\beta_1'}\} + q'\beta_2'\alpha_2'^{-\beta_2'} x_i^{\beta_2'-1} \exp\{-(x_i/\alpha_2')^{\beta_2'}\}} \end{aligned} \tag{4.18}$$

$$\begin{aligned} \omega_i(2,x_i,\boldsymbol{\theta}) = P(Z_i=2|x_i,\boldsymbol{\theta}') &= \frac{P(Z_i=2)\ P(x_i,\boldsymbol{\theta}'|Z_i=2)}{P(x_i,\boldsymbol{\theta}')} \\ &\frac{q'\beta_2'\alpha_2'^{-\beta_2'} x_i^{\beta_2'-1} \exp\{-(x_i/\alpha_2')^{\beta_2'}\}}{(1-q')\beta_1'\alpha_1'^{-\beta_1'} x_i^{\beta_1'-1} \exp\{-(x_i/\alpha_1')^{\beta_1'}\} + q'\beta_2'\alpha_2'^{-\beta_2'} x_i^{\beta_2'-1} \exp\{-(x_i/\alpha_2')^{\beta_2'}\}} \end{aligned} \tag{4.19}$$

Here, it should be noted that $\omega_i(1,x_i,\boldsymbol{\theta}) = 1 - \omega_i(2,x_i,\boldsymbol{\theta})$.

The expectation function is maximized in order to obtain the parameter estimates, by equating the gradient to zero:

$$\nabla_{\boldsymbol{\theta}}\, Q(\mathbf{x}, \boldsymbol{\theta}, \boldsymbol{\theta}') = \mathbf{0}\,. \tag{4.20}$$

Performing the operations, the estimates of a-priori probabilities and distribution parameters are found as follows.

The a-priori probability estimate of the second distribution is

$$\hat{q} = \frac{1}{N}\sum_{i=1}^{N} \omega_i(2, x_i, \boldsymbol{\theta}')\,. \tag{4.21}$$

The estimates of the scale parameters of the two distributions are

$$\hat{\alpha}_1 = \left[\frac{\sum_{i=1}^{N} (x_i)^{\hat{\beta}_1}\, \omega_i(1, x_i, \boldsymbol{\theta}')}{\sum_{i=1}^{N} \omega_i(1, x_i, \boldsymbol{\theta}')}\right]^{1/\hat{\beta}_1}, \qquad \hat{\alpha}_2 = \left[\frac{\sum_{i=1}^{N} (x_i)^{\hat{\beta}_2}\, \omega_i(2, x_i, \boldsymbol{\theta}')}{\sum_{i=1}^{N} \omega_i(2, x_i, \boldsymbol{\theta}')}\right]^{1/\hat{\beta}_2}. \tag{4.22}$$

The shape parameter estimates are obtained by solution of the equations,

$$\begin{aligned}
\sum_{i=1}^{N} \ln\left(\frac{x_i}{\alpha_1}\right) \omega_i(1, x_i, \boldsymbol{\theta}') &= \beta_1 \sum_{i=1}^{N} \left(\frac{x_i}{\alpha_1}\right)^{\beta_1} \ln\left(\frac{x_i}{\alpha_1}\right) \omega_i(1, x_i, \boldsymbol{\theta}') \\
&\qquad\qquad . \\
\sum_{i=1}^{N} \ln\left(\frac{x_i}{\alpha_2}\right) \omega_i(2, x_i, \boldsymbol{\theta}') &= \beta_2 \sum_{i=1}^{N} \left(\frac{x_i}{\alpha_2}\right)^{\beta_2} \ln\left(\frac{x_i}{\alpha_2}\right) \omega_i(2, x_i, \boldsymbol{\theta}')
\end{aligned} \tag{4.23}$$

Equations (4.23) cannot be solved easily and they require iteration. However, when these estimates are obtained, posterior probabilities and the scale parameters can be calculated easily.

In summary, the algorithm is,

1. Initialize $\mathbf{\theta'} = \{\alpha_1', \beta_1', \alpha_2', \beta_2', q'\}$ to some moderate values,
2. Compute $\omega_i(1, x_i, \mathbf{\theta'})$ using $\mathbf{\theta'}$ and find $\omega_i(2, x_i, \mathbf{\theta'}) = 1 - \omega_i(1, x_i, \mathbf{\theta'})$ for each x_i,
3. Update $\hat{\mathbf{\theta}} = \{\hat{\alpha}_1, \hat{\beta}_1, \hat{\alpha}_2, \hat{\beta}_2, \hat{q}\}$ using Equations (4.21) to (4.23),
4. Replace $\mathbf{\theta'} = \{\alpha_1', \beta_1', \alpha_2', \beta_2', q'\}$ by the new estimates $\hat{\mathbf{\theta}} = \{\hat{\alpha}_1, \hat{\beta}_1, \hat{\alpha}_2, \hat{\beta}_2, \hat{q}\}$,
5. Check the stopping criterion, i.e. the smallness of the magnitude of the difference between the previous and current estimates. If the magnitude of the difference is smaller than a predefined value, stop, otherwise, return to step 2.

Performance

In this subsection, some performance results are shown. Due to the fact that the closed form expressions for the shape parameter estimates can not be found, here, the shape parameters are assumed to be known and the performance under scale parameter changes is searched. A simulation result is shown in Figure 4.9. In this simulation, the outputs of 500 simulation runs are averaged. The first plot shows the change of the scale parameter with range. The second plot shows the a-posteriori probability of distribution 2.

The posterior probabilities have an important role in the EM-CFAR algorithm, since they determine the probability of each sample's distribution. The distribution with higher probability is selected as the distribution of the range cell under investigation.

It can be seen from the simulation output that by putting a threshold at 0.5, the differing regions can be successfully determined.

The estimation output for scale parameters and the priori probability of PDF 2 is shown in Table 4.6. It is observed that the scale parameter estimates, 0.48, 4.98 are very close to the actual ones, 0.5 and 5. The probability of PDF 2 is 0.6, which is estimated as 0.61. It can be concluded that the algorithm can identify the regions and estimate their parameters successfully.

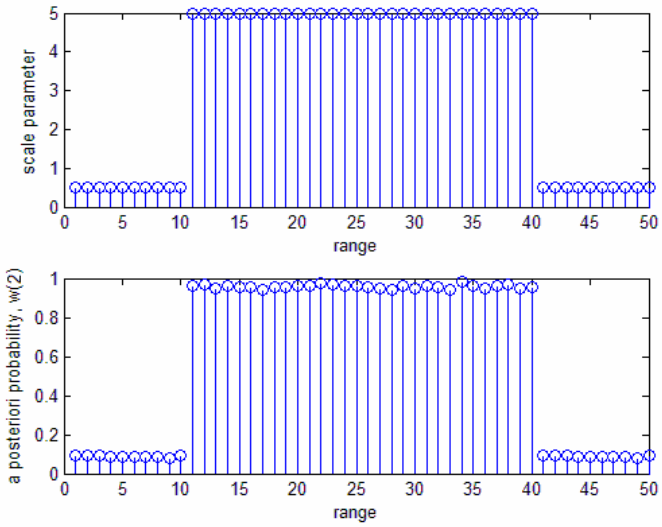

Figure 4.9 Posterior-probability estimate of EM-CFAR algorithm.
α_1=0.5, α_2=5, β_1=β_2=2, q=0.6, average of 500 simulations

Table 4.6 EM estimator outputs for scale parameters of two levels and a prior probability of PDF 2

α_0	α_1	q
0.48	4.98	0.61

In the derivation of the algorithm, it is assumed that there exists two differing distributions that the observation samples have. However, it is probable that the observation consist of homogeneous samples. As an improvement, the existence of two distributions, i.e. the transition, can be detected initially. In homogeneous case, because there is no hidden quantity, the EM algorithm is not needed and the estimates can be obtained by means of an appropriate algorithm, such as the one given by Equations (4.1) and (4.2). The homogeneity can be tested by means of an algorithm such as the Goodness of Fit test described above.

After determination of the distribution of the clutter in the cell under test and its distribution parameter estimates, the threshold can be set in order to yield the desired false alarm probability. The distribution of the clutter in the cell under test can be estimated by performing a majority check in the neighboring cell distributions.

4.3.2 Multi-Level Algorithm

The complexity of the Equations (4.23) makes the implementation of the algorithm explained in the previous section difficult, in unknown-shape parameter case. Thus, in this subsection, an algorithm is proposed to eliminate the need to estimate the shape parameter.

If the shape parameters are known or can be obtained from a clutter map, as it is assumed in some studies in the literature, the two-level algorithm can be easily extended for known shape parameter values and cover many transitions between multiple parameter levels.

The shape parameter of the Weibull radar clutter has a limited range determined by some parameters such as the depression angle, terrain type, radar resolution and wavelength. So, a set of shape parameter values can be assumed that covers the

probable terrain types. Using these assumed shape parameters, a set of PDF's, with single parameter, the scale parameter, is obtained.

Multi-distribution form of the method described above is derived as shown below.

The expression for the k^{th} PDF is (Z_i=c) (c=*1, 2, …, M*)

$$f_{W,c}(x,\alpha_c) = \beta_c^A \, \alpha_c^{-\beta_c^A} \, x^{\beta_c^A - 1} \exp(-(x/\alpha_k)^{\beta_c^A}) . \tag{4.24}$$

Here, β_c^A refers to the assumed shape parameter of the c^{th} distribution.

Carrying out similar operations that were performed in the previous section, the estimate of the occurrence probability of c^{th} distribution is obtained as

$$P[Z_i = c] = q_c, \quad \sum_{k=0}^{M-1} q_c = 1 \tag{4.25}$$

A-posterior probability of Z_i being c is

$$\omega_i(c, x_i, \boldsymbol{\theta}') = P(Z_i = c | \boldsymbol{\theta}', x_i) = \frac{\hat{q}_c \, f_c(x_i)}{\sum_{l=0}^{M-1} \hat{q}_l \, f_l(x_i)} . \tag{4.26}$$

Performing the operations, we obtain expressions for parameter estimates that are similar to the ones derived before:

$$\hat{q}_c = \frac{1}{N} \sum_{i=1}^{N} \omega_i(c, x_i, \boldsymbol{\theta}') , \tag{4.27}$$

$$\hat{\alpha}_c = \left[\frac{\sum_{i=1}^{N} x_i^{\beta_c^A} \omega_i(c, x_i, \boldsymbol{\theta}')}{\sum_{i=1}^{N} \omega_i(c, x_i, \boldsymbol{\theta}')} \right]^{1/\beta_c^A} \tag{4.28}$$

The question to be answered next is the selection of the shape parameter or the PDF set.

It is well known that the variance of the estimation error is bounded by the Cramer-Rao Lower Bound. Any estimator yields an estimation error variance greater than this value. Thus, it is not meaningful to work on parameter values that are close to each other more than the value determined by the bound. Thus, the Cramer-Rao lower bound is utilized in determination of the values in the assumed shape parameter set.

The CRB bounds for Weibull distribution shape and scale parameters estimation errors are derived as follows.

The error variance is denoted by $\sigma_{\varepsilon,i}{}^2$. Then the CRB for this variance is [59]

$$\sigma_{\varepsilon,i}{}^2 = Var\left[\hat{\theta}_i(\mathbf{x}) - \theta_i\right] \geq J^{ii}, \tag{4.29}$$

where J^{ii} is the i,i^{th} element of the inverse of the Fisher Information matrix (FIM), J. The FIM is defined as

$$J = -E\left\{\nabla_{\boldsymbol{\theta}}\left\{\nabla_{\boldsymbol{\theta}} \ln P_{\mathbf{x}|\boldsymbol{\theta}}(\mathbf{x}|\boldsymbol{\theta})\right\}^T\right\}. \tag{4.30}$$

The logarithm of the PDF can be written as

$$\ln P_{\mathbf{x}|\boldsymbol{\theta}}(\mathbf{x}|\boldsymbol{\theta}) = N\ln\beta - \beta N\ln\alpha + (\beta-1)\sum_{i=0}^{N-1}\ln x_i - \sum_{i=0}^{N-1}(x_i/\alpha)^{\beta}, \tag{4.31}$$

where the parameter vector is $\boldsymbol{\theta} = [\alpha\ \beta]^T$. The gradient of the function is

$$\nabla_{\boldsymbol{\theta}} \ln P_{\mathbf{x}|\boldsymbol{\theta}}(\mathbf{x}|\boldsymbol{\theta}) = \begin{bmatrix} -\beta N\dfrac{1}{\alpha} + \beta\alpha^{-\beta-1}\displaystyle\sum_{i=0}^{N-1}(x_i)^{\beta} \\ \dfrac{N}{\beta} - N\ln\alpha + \displaystyle\sum_{i=0}^{N-1}\ln x_i - \sum_{i=0}^{N-1}(x_i/\alpha)^{\beta}\ln(x_i/\alpha) \end{bmatrix}. \tag{4.32}$$

Taking the partial derivatives again, the matrix becomes

$$\begin{bmatrix} \dfrac{\beta N}{\alpha^2} - \alpha^{-\beta-2}\beta(1+\beta)\displaystyle\sum_{i=0}^{N-1}x_i^{\beta} & -\dfrac{N}{\alpha} + \displaystyle\sum_{i=0}^{N-1}x_i^{\beta}\alpha^{-\beta-1}(1+\beta\ln x_i - \beta\ln\alpha) \\ -\dfrac{N}{\alpha} + \displaystyle\sum_{i=0}^{N-1}x_i^{\beta}\alpha^{-\beta-1}(1+\beta\ln x_i - \beta\ln\alpha) & -\dfrac{N}{\beta^2} - \displaystyle\sum_{i=0}^{N-1}(\frac{x_i}{\alpha})^{\beta}\left[\ln\left(\frac{x_i}{\alpha}\right)\right]^2 \end{bmatrix}. \tag{4.33}$$

Evaluating the expectation of the matrix, the FIM is obtained as

$$J = N\begin{bmatrix} \left(\dfrac{\beta}{\alpha}\right)^2 & \dfrac{m}{\alpha} \\ \dfrac{m}{\alpha} & \dfrac{k}{\beta^2} \end{bmatrix}, \tag{4.34}$$

where

$$m \overset{\Delta}{=} \gamma_e - 1, \text{ and } k \overset{\Delta}{=} 1 + \gamma_e(\gamma_e - 2) + \frac{\pi^2}{6}. \tag{4.35}$$

Here, γ_e is the Euler constant which is approximately, 0.5772.

The inverse matrix is

$$J^{-1} = \frac{1}{N}\begin{bmatrix} \dfrac{k\alpha^2}{(k-m^2)\beta^2} & \dfrac{m\alpha}{(m^2-k)} \\ \dfrac{m\alpha}{(m^2-k)} & \dfrac{\beta^2}{(k-m^2)} \end{bmatrix}. \tag{4.36}$$

Hence, the variances for the scale and shape parameter estimation errors are,

$$\sigma_\alpha^2 \geq \frac{1}{N}\frac{k\alpha^2}{(k-m^2)\beta^2}, \quad \sigma_\beta^2 \geq \frac{1}{N}\frac{\beta^2}{(k-m^2)}. \tag{4.37}$$

Substituting the constants, the error variances for scale and shape parameters,

$$\sigma_\alpha^2 \geq \frac{1}{N}\frac{\alpha^2}{\beta^2}(1.1086) \quad \text{and} \quad \sigma_\beta^2 \geq \frac{1}{N}\frac{\beta^2}{(1.6449)}, \tag{4.38}$$

are found.

As an example, if the shape parameter is assumed to have values from the set $\beta \in [0.1, 2]$, for N=20 range samples, the standard deviations of the errors are found to be

$\sigma_\beta \geq 0.017$ for $\beta = 0.1$; $\sigma_\beta \geq 0.122$ for $\beta = 0.7$; $\sigma_\beta \geq 0.246$ for $\beta = 1$; $\sigma_\beta \geq 0.348$ for $\beta = 2$.

In CFAR operation, the difference between the estimated shape parameter and the actual one effects the detection and false alarm probabilities. The actual false alarm probability, in terms of the desired (design) false alarm probability, assumed shape parameter and the actual shape parameter, is given by the following formula:

$$P_{FA,actual} = \exp\left(-\left(\ln\frac{1}{P_{FA,design}}\right)^{\beta/\beta_{assumed}}\right) \tag{4.39}$$

Figure 4.10 shows the change of the false alarm probability versus the ratio of the actual and designed shape parameters. It is observed that the false alarm probability is very sensitive to the ratio between the actual and assumed parameters. In thresholding operation, it is important to keep the false alarm rate at the desired value. Any probability that is smaller than this value also decreases the detection probability.

It can be seen from Equation (4.37) that the standard deviation of the shape parameter estimation error is directly proportional to the actual value of it. Thus, the steps of the assumed parameters should be non-uniform. The step size should increase with increasing shape parameter.

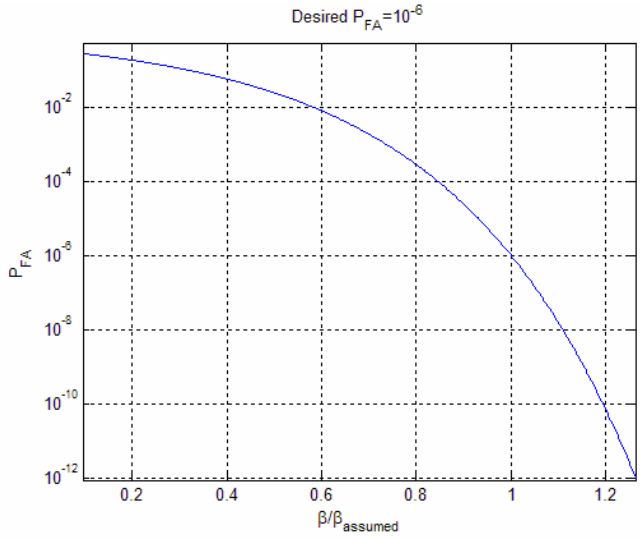

Figure 4.10 Change of probability of false alarm with the ratio of actual and estimated shape parameters

The standard deviation of the error is given by

$$\sigma_\beta \geq \frac{\beta}{\sqrt{N\gamma}}. \tag{4.40}$$

Hence, the minimum value of the n^{th} step size is

$$\Delta\beta_n \overset{\Delta}{=} \beta_{n+1} - \beta_n \geq \sigma_{n+1} + \sigma_n = \frac{\beta_{n+1} + \beta_n}{\sqrt{N\gamma}}. \tag{4.41}$$

Introducing a new parameter

$$\lambda \overset{\Delta}{=} \frac{\sqrt{N\gamma}+1}{\sqrt{N\gamma}-1}, \tag{4.42}$$

and representing the minimum shape parameter by β_0, n^{th} shape parameter value in the set will be

$$\beta_n = \beta_0 \, \lambda^n. \tag{4.43}$$

The maximum value of the shape parameter is limited at 2, which corresponds to the Rayleigh distribution.

Figure 4.11 shows a parameter set when the number of range samples is 40. The starting parameter is set to 0.3. The elements of the set are placed non-uniformly and are 0.30, 0.38, 0.49, 0.63, 0.80, 1.03, 1.32, 1.70, 2.17 and 2.00.

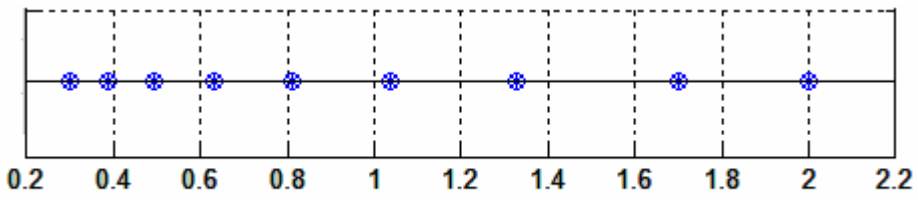

Figure 4.11 Designed shape parameter set for the multi-level EM-CFAR algorithm

Defining a set with more elements is not necessary, as no estimation method can yield better results and generate estimates closer to the actual values.

Performance

In performance analysis, the a-priori probabilities and assumed shape parameters are chosen as shown in Table 4.7. The four assumed parameters form four different distributions.

Table 4.7 EM-CFAR test scenario 1, assumed shape parameters and a priori probabilities

	PDF_1	PDF_2	PDF_3	PDF_4
Assumed shape parameter, β	0.5	0.75	1.4	2
A priori probability, q	0	0	0.6	0.4

The actual scenario is as shown in Table 4.8. The first 20 range samples are land echoes, next 60 samples are echoes from river and the last 20 samples are again from land.

The simulation results of the multi-level algorithm are shown in Figure 4.12. The four plots show the a-posterior probabilities of the four distributions at each sample. The results are obtained as a result of 500 trials.

Table 4.8 EM-CFAR test scenario 1, actual distribution parameters

	20 samples (Land)	60 samples (River)	20 samples (Land)
α	2	7	2
β	2 (PDF_4)	1.4 (PDF_3)	2 (PDF_4)

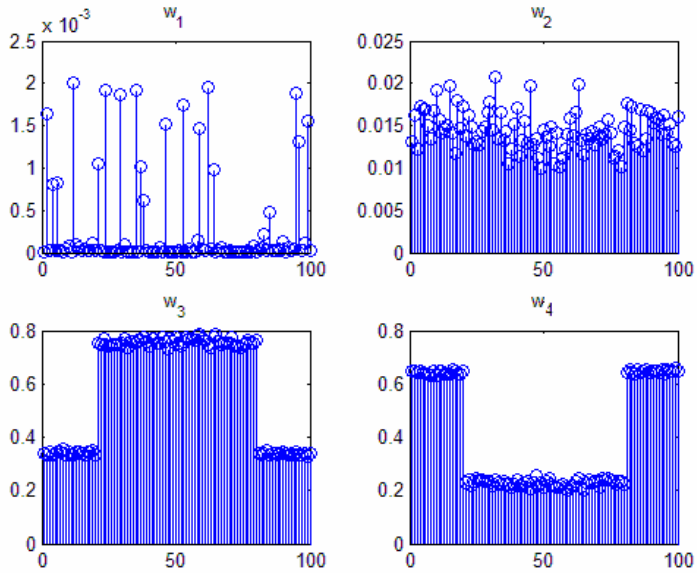

Figure 4.12 EM-CFA, a posteriori probabilities of the assumed distributions

By choosing the maximum-of the a-posteriori probabilities at each range sample, the most likely distribution of each sample can be found. Hence, the distributions are obtained for each range sample, as shown by Table 4.9. Apparently, the actual probabilities are found correctly.

Table 4.9 EM-CFAR, estimated distributions

	20 samples	60 samples	20 samples
PDF	PDF_4	PDF_3	PDF_4

The scale parameter and a-priori PDF estimates are obtained as by-products of the algorithm and they are shown in Table 4.10. The scale parameters of the 3rd and 4th distributions are estimated successfully. However, as there are no samples from the 1st and 2nd distributions in the range, the parameter estimates for these distributions are not useful. The occurrence probabilities of the distributions are also estimated correctly.

Table 4.10 EM-CFAR, estimated distribution parameters and a priori probabilities.

	PDF_1	PDF_2	PDF_3	PDF_4
Scale parameter estimate : $\hat{\alpha}$	2.98	3.80	7.05	2.01
Actual scale parameter	1	1	7	2
A-priori probability estimate : $\hat{q}$	0.00	0.01	0.59	0.40

In some of the cases, scale parameters that are estimated using the probabilistic mixture defined above, are not very close to the actual values. As an improvement, the estimation can be performed among the members of the specific PDF. This data is referred to as *training data*. This may be viewed as a conversion to the deterministic mixture. Having determined the training data for a given PDF and assuming it has the shape parameter assumed previously, the ML estimate of the scale parameter can be found using Equation (3.14) instead of the estimate obtained by the algorithm:

$$\hat{\alpha}_c = \left(\frac{1}{n} \sum_{i \in dist\, c} x_i^{\beta_c^A} \right)^{1/\beta_c^A} \tag{4.44}$$

The estimates, obtained using the training data and the ML estimation method, are given in Table 4.11. As it can be seen, the estimates using ML method performed over the training data are better. The improvement is more apparent in severe conditions.

Table 4.11 Parameter estimation using EM-CFAR algorithm and improved algorithm which uses ML estimation

	PDF_0	PDF_1	PDF_2	PDF_3
Classical algorithm estimate : $\hat{\alpha}$	2.98	3.80	7.05	2.01
Training data and ML estimate	-	-	7.02	2.00
Actual scale parameter	1	1	7	2

The next analysis shows the performance in a situation where, again, both of the scale and shape parameters change. In the first region, SCR is 25dB and in the second one, it is 10dB. This corresponds to the case where the scale parameter changes from 0.03 to 0.26, while the target signal has unit power. Shape parameters are set to 0.8 and 1.2, respectively. This is shown in Table 4.12. A target is located at the 21st range bin.

Table 4.12 EM-CFAR test scenario 2, actual distribution parameters

	40 samples	40 samples
α	0.03	0.26
β	0.8	1.2

Figure 4.13 shows the scale parameter estimates of the two regions obtained at each of the 200 simulation points. The estimated values are very close to the actual ones at most of the simulations.

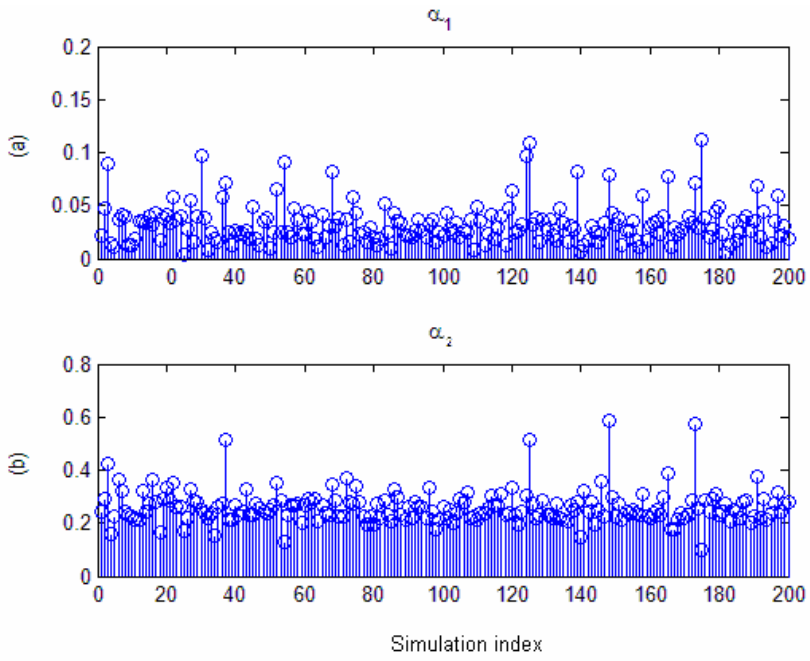

Figure 4.13 EM-CFAR, scale parameter estimates for each simulation point
(a) First distribution, (b) Second distribution

After determination of the parameters, the threshold is set easily using Equation (4.8). For the example given above, the amplitude of the observation and the threshold generated by the algorithm is shown in Figure 4.14. The first figure shows a single run and the second one shows the average of the 200 simulations. It can be seen that the threshold follows the signal successfully and the target can be detected while alleviating the false alarms. The threshold obtained with homogeneous Rayleigh clutter assumption yields many false alarms.

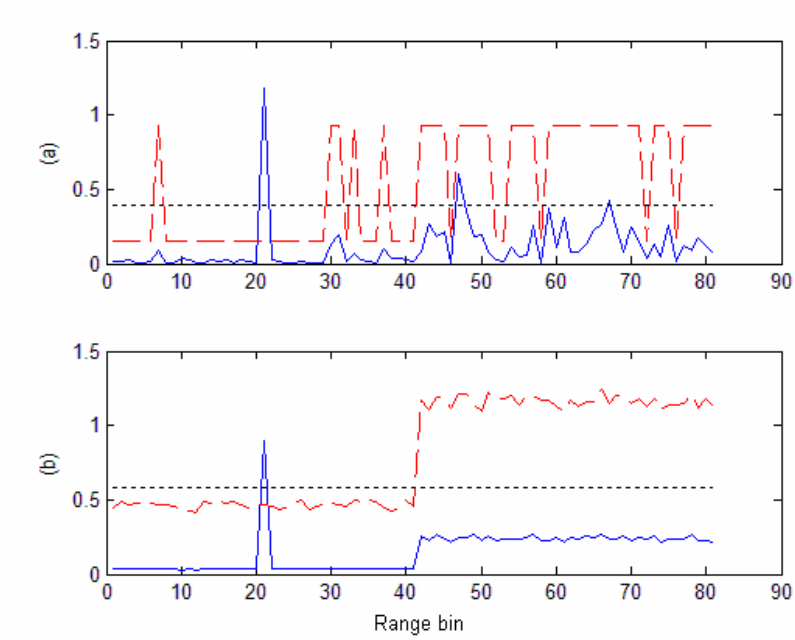

Figure 4.14 Amplitude of the signal and the threshold values obtained with EM-CFAR algorithm

(a) Single simulation, (b) Average of the simulations, dashed: EM-CFAR threshold, dotted: Threshold obtained with homogeneous Rayleigh amplitude assumption, solid: Signal amplitude, SCR=25dB

4.4 Clutter-Map CFAR

The methods explained above are designed with the assumption that the clutter changes significantly in time so that a clutter map can not be formed, that is the previous clutter information can not be exploited in estimation of the current one. However, when the environment does not change significantly, as in the case of land-based radars, a map can be formed that stores the previous clutter information and enables its use in current estimation. Clutter map is regularly updated in order to track the mild changes in clutter state.

In the clutter environment under consideration, the map stores the shape and scale parameters of the Weibull clutter and updates this information at each new data arrival.

It is known that the methods for estimation of Weibull distribution parameters require the entire observation data. However, in most of the radar applications, it is desired to obtain the estimate without waiting the arrival of the whole data set. Moreover, in radar applications, the previous observations form a huge amount of data and storage requirement is enormous. Therefore, in this study, a *recursive estimation* method, which updates the estimates with each new observation and does not require the previous data, is designed. The method is very advantageous due to the following reasons:

- The estimation does not require the whole observation data in update of the clutter map,
- The method is computationally efficient when compared to the other methods, so it is suitable for radar applications,
- The method can adapt to the changing clutter environment, which may occur, for instance, in changing wind conditions.

Two estimation algorithms, namely the method of scoring and the recursive least squares estimation are considered.

4.4.1 Method of Scoring

In this method, the recursions in estimation maximize the relative entropy at each iteration step. It is declared that the resulting estimates often share some of the desirable properties of ML estimates [10]. Therefore, this method seems to meet the needs.

In a recent work, this method was implemented for K-distribution [10]. However, Weibull distribution case was not encountered in the literature survey.

The method can be summarized as follows:

Let $\{x_1, x_2, \cdots\}$ be the observation samples and $\boldsymbol{\theta} = [\alpha\ \beta]^T$ be the parameter vector to be estimated. The update equation that uses the new arriving sample and previous estimate is

$$\boldsymbol{\theta}_{n+1} = \boldsymbol{\theta}_n + \varepsilon_n \mathbf{F}_n \boldsymbol{\gamma}(x_{n+1}, \boldsymbol{\theta}_n), \qquad n = 0,1,\cdots \tag{4.45}$$

where $\boldsymbol{\theta}_n$ is the estimate obtained after n observations, $\mathbf{F}_n$ is a gain matrix and ε_n is the step size. The score vector represented by $\boldsymbol{\gamma}(x_n, \boldsymbol{\theta}_n)$ is

$$\boldsymbol{\gamma}(x_n, \boldsymbol{\theta}_n) = \nabla_{\boldsymbol{\theta}} \ln(p(x_n|\boldsymbol{\theta}))_{|\boldsymbol{\theta}=\boldsymbol{\theta}_n}. \tag{4.46}$$

The form of the gain matrix affects the convergence property of the recursion. The inverse of the information matrix, $\mathbf{I}(\boldsymbol{\theta}_n)$, of the observed data is a common choice:

$$\mathbf{F}_n = \mathbf{I}^{-1}(\boldsymbol{\theta}_n). \tag{4.47}$$

$$\mathbf{I}(\boldsymbol{\theta}_n) = E\left\{\boldsymbol{\gamma}(x_n, \boldsymbol{\theta}_n)\boldsymbol{\gamma}(x_n, \boldsymbol{\theta}_n)^T\right\} \tag{4.48}$$

For Weibull case, the derivations are done to yield the elements of the information matrix

$$I(\theta_n) = E\left\{\gamma(x_n, \theta_n)\gamma(x_n, \theta_n)^T\right\} \tag{4.49}$$

as

$$I_{1,1}(\theta_n) = E\left\{\left(-\beta_n \frac{1}{\alpha_n} + \beta_n \alpha_n^{-\beta_n - 1} x_n^{\beta_n} \right)^2 \right\} = (\frac{\beta_n}{\alpha_n})^2 , \tag{4.50}$$

$$I_{1,2}(\theta_n) = E\left\{\left(\frac{1}{\beta_n} - \ln \alpha_n + \ln x_n - \left(\frac{x_n}{\alpha_n} \right)^{\beta_n} \ln(\frac{x_n}{\alpha_n}) \right)\left(-\beta_n \frac{1}{\alpha_n} + \beta_n \alpha_n^{-\beta_n - 1} x_n^{\beta_n} \right)\right\}, \tag{4.51}$$

$$= \frac{-1+\gamma_e}{\alpha_n} = \frac{-0.4228}{\alpha_n}$$

$$I_{2,1}(\theta_n) = I_{1,2}(\theta_n) , \tag{4.52}$$

and

$$I_{2,2}(\theta_n) = E\left\{\left(\frac{1}{\beta_n} - \ln \alpha_n + \ln x_n - \left(\frac{x_n}{\alpha_n} \right)^{\beta_n} \ln(\frac{x_n}{\alpha_n}) \right)^2 \right\} = \frac{6(-1+\gamma_e)^2 + \pi^2}{6\beta_n^{\,2}} = \frac{1.8237}{\beta_n^{\,2}} . \tag{4.53}$$

$$\gamma(x_{n+1}, \theta_n) = \left[\left(-\beta_n \frac{1}{\alpha_n} + \beta_n \alpha_n^{-\beta_n - 1} x_{n+1}^{\beta_n} \right) \left(\frac{1}{\beta_n} - \ln \alpha_n + \ln x_{n+1} - \left(\frac{x_{n+1}}{\alpha_n} \right)^{\beta_n} \ln(\frac{x_{n+1}}{\alpha_n}) \right) \right]^T \tag{4.54}$$

A common choice for step parameter is

$$\varepsilon_n = an^{-b}, \text{ where } \; a > 0, \quad 0.5 < b \le 1 . \tag{4.55}$$

Actually, these recursions converge to the estimates that maximize the likelihood function and at the same time make the score vector zero. The Newton-Raphson method can also be employed in solution of the equation. In Newton-Raphson iteration, the general update expression is

$$\varphi_{n+1} = \varphi_n + \alpha_n \frac{L'(\varphi_n)}{L''(\varphi_n)} \tag{4.56}$$

The denominator may be viewed as the Hessian of the likelihood function for multivariable case. In Fisher's method of scoring, this Hessian is replaced with its expected value.

$$\varphi_{n+1} = \varphi_n + \alpha_n \frac{L'(\varphi_n)}{I(\varphi_n)} \tag{4.57}$$

The performance of estimation using Method of Scoring is shown next. Figure 4.15 shows the histogram of the estimates when the scale parameter is 1 and the shape parameter is 1.5. The algorithm starts with the initial values of α_0=1.5, β_0=2. It is seen that the estimator performs well.

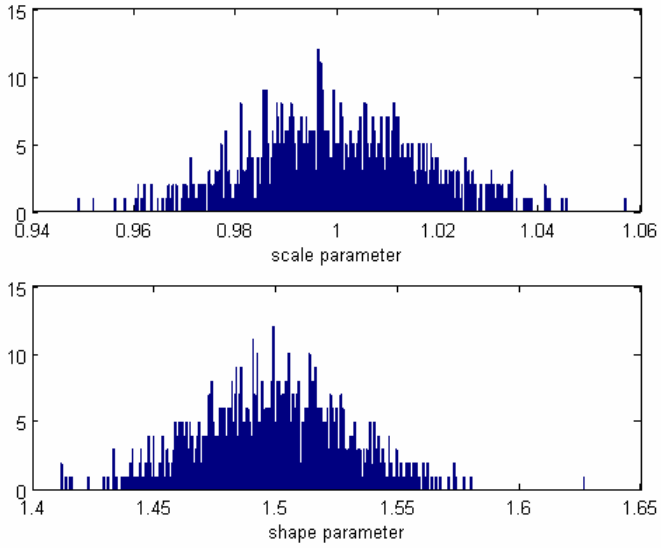

Figure 4.15 Histograms of estimates obtained with method of scoring
Actual values: α=1, β=1.5; initial values: α_0=1.5, β_0=2, 1000 simulations

However, a problem with this method is that in about 1% of the trials (rate is dependent on the Weibull parameters), divergence occurs. As a remedy to this problem, censoring is performed. It is known that for radar clutter, Weibull shape parameter has a limited range.

With the aim of simplifying the expressions obtained above and eliminating the divergence problems, estimation for Gumbel distribution (log-weibull) is also considered. However, exactly the same expressions were obtained for this distribution. So, no simplifications could be performed.

This work was presented in [17].

4.4.2 RLS Estimation

It is expected that the estimation method derived in the previous section can be improved by employing Recursive Least Squares (RLS) algorithm.

As observed from the update equation, when "$\varepsilon_n \; F_n \; \gamma(x_{n+1}, \theta_n)$" expression equates to zero, which is equivalent to maximizing the likelihood, the convergence is obtained:

$$\boldsymbol{\theta}_{n+1} = \boldsymbol{\theta}_n + \varepsilon_n \; \mathbf{F}_n \; \gamma(x_{n+1}, \boldsymbol{\theta}_n). \qquad n = 0,1,\cdots \tag{4.58}$$

In RLS algorithm, the cost function to be minimized is defined as

$$J(n) = \sum_{i=1}^{n} \lambda^{n-i} \; |e(i)|^2 \; . \tag{4.59}$$

Here, λ is the forgetting factor. Referring to the previous section, the cost function may be written as

$$J(n) = \sum_{i=1}^{n} \lambda^{n-i} \left\| \boldsymbol{\gamma}(x_i, \boldsymbol{\theta}_n) \right\|^2 . \tag{4.60}$$

However, in multi-parameter case, one of the parameters may be emphasized over the other. Hence, the following cost function is proposed:

$$J(n) = \sum_{i=1}^{n} \lambda^{n-i} \left\| \mathbf{F}_n \ \gamma(x_i, \boldsymbol{\theta}_n) \right\|^2 . \tag{4.61}$$

Since the gain matrix, $\mathbf{F}_n$ normalizes the powers of the two variables, decoupling of the two parameters is satisfied and in this case, no emphasis on one of the parameters is expected. When the distribution has one parameter, there is no such problem in estimation.

Gaussian RLS Estimation

Firstly, the derivation is performed for Gaussian PDF case. The Gaussian PDF is

$$p_x(x) = \frac{1}{\sqrt{2\pi}\sigma} e^{-x^2 / 2\sigma^2} . \tag{4.62}$$

Here, the estimated parameter θ is σ^2. The score vector is obtained as

$$\gamma(x, \theta) = \frac{\partial}{\partial \theta} \ln p_x(x, \theta) = \frac{1}{\sigma^3} (x^2 - \sigma^2) . \tag{4.63}$$

Thus, the cost function is

$$J(n) = \sum_{i=1}^{n} \lambda^{n-i} \frac{1}{\sigma_n^{\ 6}} (x_i^{\ 2} - \sigma_n^{\ 2})^2 . \tag{4.64}$$

Taking the derivative with respect to the parameter to be estimated and equating to zero,

$$\frac{\partial}{\partial\theta}J(n)=\sum_{i=1}^{n}\lambda^{n-i}2(x_i^{\,2}-\sigma_n^{\,2})2\sigma_n=0 \qquad (\sigma_n\neq 0) \tag{4.65}$$

is obtained, which can be written as

$$\sum_{i=1}^{n}\lambda^{n-i}x_i^{\,2}=\sum_{i=1}^{n}\lambda^{n-i}\sigma_n^{\,2}\,. \tag{4.66}$$

Solving for σ^2,

$$\sigma_n^{\,2}=\frac{\sum_{i=1}^{n}\lambda^{n-i}x_i^{\,2}}{\sum_{i=1}^{n}\lambda^{n-i}} \tag{4.67}$$

is found.

With λ=1, the estimate becomes

$$\sigma_n^{\,2}=\frac{\sum_{i=1}^{n}x_i^{\,2}}{n}\,, \tag{4.68}$$

which is the expected result, the ML estimate of the power.

In this case, the recursion has the following form:

$$\sigma_{n+1}^{\,2}=\frac{n}{n+1}\sigma_n^{\,2}+\frac{1}{n}x_{n+1}^{\,2} \tag{4.69}$$

This result is similar to the well-known clutter map update for Rayleigh envelope, also named as the exponential filtering, with time varying coefficients.

Weibull RLS Estimation

The derivations are repeated for Weibull case. In this case, the multivariable update form is used. The cost function is

$$J(n)=\sum_{i=1}^{n}\lambda^{n-i}\left\|\boldsymbol{\chi}(x_i,\boldsymbol{\theta}_n)\right\|^2 . \tag{4.70}$$

The error vector is found to be

$$\boldsymbol{\chi}(x,\boldsymbol{\theta}_n)=\mathbf{F}_n\,\boldsymbol{\gamma}(x,\boldsymbol{\theta}_n)=\begin{bmatrix}\alpha[-\frac{\mu}{\beta}+((\frac{x}{\alpha})^{\beta}-1)(\frac{\rho}{\beta}+\mu\ln(\frac{x}{\alpha}))]\\ \beta[1+((\frac{x}{\alpha})^{\beta}-1)(-\mu-\beta\ln(\frac{x}{\alpha}))]\end{bmatrix} \tag{4.71}$$

Taking the derivatives with respect to scale and shape parameters,

$$\begin{aligned}&\frac{\partial}{\partial\alpha}J(n)=\sum_{i=1}^{n}\lambda^{n-i}\,[-\frac{1}{\beta^2}(2\alpha(-\mu+((\frac{x_i}{\alpha})^{\beta}-1)\rho+((\frac{x_i}{\alpha})^{\beta}-1)\beta\mu\ln(\frac{x_i}{\alpha}))\\&(\mu-\beta\mu+\rho+\beta\mu\ln(\frac{x_i}{\alpha})+(\frac{x_i}{\alpha})^{\beta}(-\rho+\beta(\mu+\rho)+(1-\beta)\beta\mu\ln(\frac{x_i}{\alpha})))]=0\end{aligned}, \tag{4.72}$$

and

$$\begin{aligned}&\frac{\partial}{\partial\beta}J(n)=\sum_{i=1}^{n}\lambda^{n-i}\,[\frac{1}{\beta^3}(2\alpha^2(-\mu+((\frac{x_i}{\alpha})^{\beta}-1)\rho+((\frac{x_i}{\alpha})^{\beta}-1)\beta\mu\ln(\frac{x_i}{\alpha}))\\&(\mu+\rho+(\frac{x_i}{\alpha})^{\beta}(-\rho+\beta\ln(\frac{x_i}{\alpha})(\rho+\beta\mu\ln(\frac{x_i}{\alpha})))))]=0\end{aligned} \tag{4.73}$$

are obtained.

Unfortunately, the update equations shown above cannot be solved explicitly. The results are computationally costly and are not appropriate for implementation.

Performance

Firstly, the performance of parameter estimation and change in detection probability with changing number of scans (or clutter map update rate) is investigated. When the shape parameter $\beta=1.5$, SCR=20dB and the desired false alarm probability is $P_{FA}=10^{-3}$, the detection probability reaches 0.8 at 100^{th} scan and approximates 0.9 at 150^{th} scan, which is the value that can be obtained when the parameters are exactly known.

Change of detection probability with signal to clutter ratio is shown in Figure 4.16. The dotted and the solid curves show the performance obtained with the proposed method and with the exact knowledge of the parameters, respectively. There is a 2-3dB SCR loss when compared to the performance obtained with the knowledge of the parameters. Some performance degradation occurs when the clutter becomes spikier.

The next result shows the performance under a time-varying condition. In this scenario, the shape parameter is 2 at the beginning and starts decreasing linearly at the 400^{th} scan and reaches the value of 1 at the 700^{th}, after which it remains constant. The detection and false alarm probabilities obtained in this case are shown in Figure 4.17 and Figure 4.18. The dotted curves show the performance when the correct threshold is used. As expected, when the shape parameter gets smaller (after 400^{th} scan), the difference between the detection probabilities obtained with the proposed method and the ideal one increases. The proposed method performs well in keeping the false alarm rate constant, as can be seen in Figure 4.18. In this scenario, the classical one-parameter clutter-map method yields a false alarm rate of 10^{-1}.

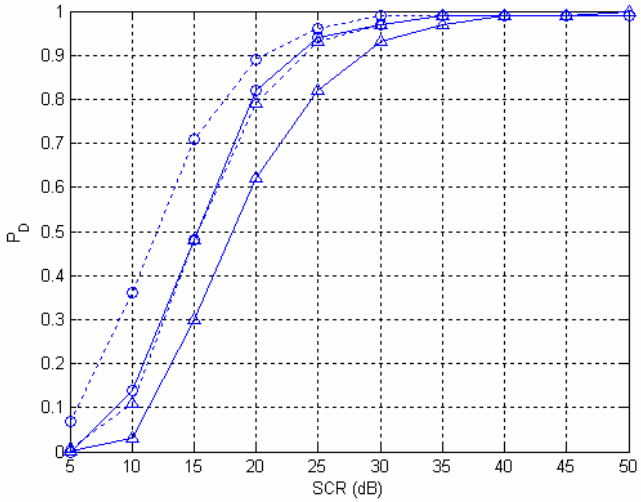

Figure 4.16 CM-CFAR, change of detection probability with SCR for different shape parameter values

N=100, 10^4 simulations, desired $P_{FA}=10^{-3}$

o:β=1.5, Δ:β=1, …: Exact knowledge of the parameters

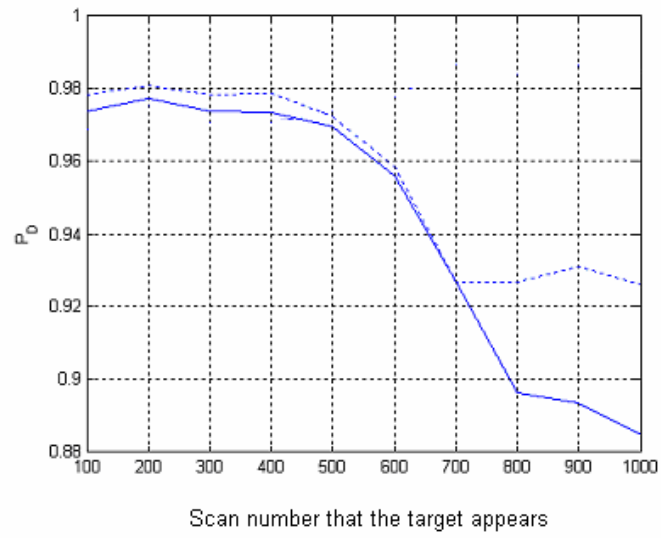

Figure 4.17 CM-CFAR, probability of detection in the time-varying scenario

SCR=25dB, 10^4 simulations

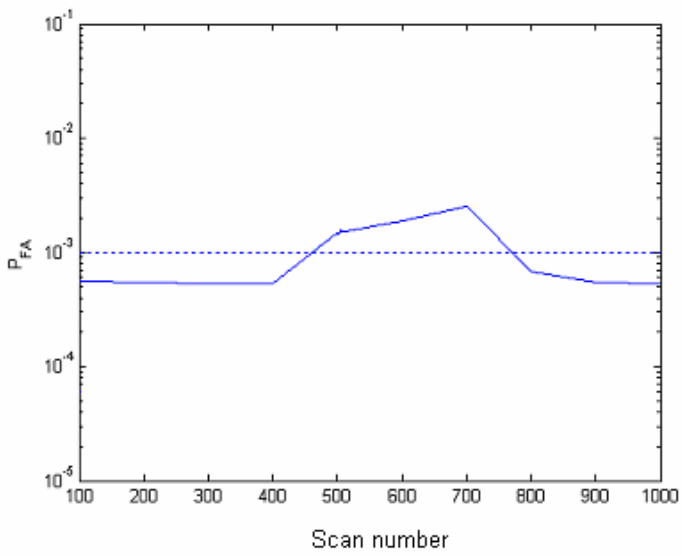

Figure 4.18 CM-CFAR, probability of false alarm in the time-varying scenario 10^4 simulations, desired $P_{FA}=10^{-3}$

CHAPTER 5

COHERENT CLUTTER ESTIMATION

In this chapter, coherent clutter estimators are derived which are used in coherent detection of signals in non-Gaussian interference environment. The estimation can also be used in threshold determination for CFAR operation or segmentation and classification in SAR images.

As explained in Section 2.2.2, Compound Gaussian Clutter can be represented as the product of two independent random variables, the speckle and the texture. The texture component is a slowly varying parameter and is a measure of the clutter power. In this study, it is assumed that the speckle covariance matrix is exactly known and the texture component is estimated. For instance, for land-based radars, speckle covariance matrix can be formulated as a function of the radar system parameters such as antenna rotation period, beamwidth and beamshape.

The texture component may have different correlation characteristics, depending on the clutter nature. It may be identical or independent in all of the range cells under consideration. The partial correlation case, which is an intermediate case between full and no-correlation cases, is also considered. For each of the scenarios, both ML and MAP estimators are derived.

5.1 Compound-Gaussian Clutter Notation

In this section, the notation for compound Gaussian model for multiple range cells is given. The notation can also be extended to represent the signal received from multiple antennas as in the case of STAP.

Let the observation signal, which is composed of samples from N pulses of M range cells, be

$$\begin{aligned}\mathbf{r} &\stackrel{\Delta}{=} [\mathbf{r_1}^T \quad \mathbf{r_2}^T \quad \cdots \quad \mathbf{r_M}^T] \\ &= \left[\sqrt{\tau_1}(x_{11} \quad x_{12} \quad \cdots \quad x_{1N}) \quad \sqrt{\tau_2}(x_{21} \quad x_{22} \quad \cdots \quad x_{2N}) \quad \cdots\cdots \quad \sqrt{\tau_M}(x_{M1} \quad x_{M2} \quad \cdots \quad x_{MN})\right]^T\end{aligned} \tag{5.1}$$

Here, τ is the texture parameter. The texture components may be correlated, uncorrelated or partially correlated from range cell to range cell. Distribution of the texture component determines the distribution of the clutter. x_{ij}'s are speckle parameters and have zero-mean complex Gaussian distribution. They are correlated within the same range cell, and are uncorrelated among different range cells.

Speckle component of i'th range cell can be denoted by

$$\mathbf{x_i} \stackrel{\Delta}{=} [x_{i1} \quad x_{i2} \quad x_{i3} \quad \cdots \quad x_{iN}]^T . \tag{5.2}$$

The PDF of $\mathbf{x_i}$ can be written as given below:

$$p_{\mathbf{x}}(\mathbf{x_i}) = \frac{1}{\pi^N |\mathbf{M_x}|} \exp[-\mathbf{x_i}^H \mathbf{M_x}^{-1} \mathbf{x_i}] . \tag{5.3}$$

Here, $\mathbf{M}_{\mathbf{x}} = E\{\mathbf{x}\,\mathbf{x}^{\mathbf{H}}\}$ is the covariance matrix of the elements of the speckle component of the signal from a range cell. The elements in the speckle component are highly correlated.

The PDF of $\mathbf{r}$, conditioned on the texture parameter vector, $\mathbf{T} = [\tau_1 \quad \tau_2 \quad \cdots \quad \tau_M]^T$, is

$$p_{\mathbf{r}|\mathbf{T}}(\mathbf{r}|\mathbf{T}) = \frac{1}{\pi^{NM}|\mathbf{M}_{\mathbf{r}}|}\exp[-\mathbf{r}^H\mathbf{M}_{\mathbf{r}}{}^{-1}\mathbf{r}], \tag{5.4}$$

where $\mathbf{M_r}$ is the covariance matrix.

The marginal PDF of the texture component was given before but is repeated here for the sake of completeness. For K-distributed clutter, the texture has a Gamma distribution:

$$p_{\tau}(\tau) = \frac{1}{\Gamma(\nu)}\left(\frac{\nu}{\mu}\right)^{\nu}\tau^{\nu-1}\exp(-\frac{\nu}{\mu}\tau). \tag{5.5}$$

Next, the PDF for partially-correlated texture components of range cells will be given. The joint PDF of the complex clutter can be written in terms of the texture component as [8]

$$p(\mathbf{r_1},\mathbf{r_2},\cdots\mathbf{r_M}) = \int_0^{\infty}\cdots\int_0^{\infty} p_{\mathbf{T}}(\mathbf{T})\frac{1}{\pi^{NM}|M_s|^M}\prod_{n=1}^{M}\frac{1}{\tau_n{}^N}\exp(-\frac{1}{\tau_n}\mathbf{r}_n{}^H M_s^{-1}\mathbf{r}_n)\,d\tau_1\cdots d\tau_M\,. \tag{5.6}$$

Correlation structure of the texture component is inherent in $p_{\mathbf{T}}(\mathbf{T})$. The expressions for a general correlation structure are found to be too complex, so to simplify the analysis, a first-order Markov structure is assumed [36]:

$$p_{\mathbf{T}}(\mathbf{T}) = p_{\tau_2|\tau_1}(\tau_M|\tau_{M-1})\; p_{\tau_2|\tau_1}(\tau_{M-1}|\tau_{M-2})\cdots p_{\tau_2|\tau_1}(\tau_2|\tau_1), \tag{5.7}$$

$$p_{\tau_1|\tau_0}(\tau_m|\tau_{m-1}) = \frac{\nu}{\mu}\frac{1}{\rho_\tau^{(\nu-1)/2}(1-\rho_\tau)}\left(\frac{\tau_m}{\tau_{m-1}}\right)^{\frac{\nu-1}{2}} \tag{5.8}$$

$$\times\exp\left[-\frac{\nu}{\mu}\frac{\tau_m+\rho_\tau\tau_{m-1}}{1-\rho_\tau}\right] I_{\nu-1}\left[\frac{\nu}{\mu}\frac{1}{(1-\rho_\tau)}\sqrt{\rho_\tau\tau_m\tau_{m-1}}\right],$$

where ρ_τ is the one-lag correlation coefficient.

When the order parameter v can be written as $v=(k+1)/2$, k=0,1,2, the gamma distribution reduces to the chi-square distribution which can be written as the sum of squares of $2v$ zero-mean independent Gaussian processes, g_i. In generation of the correlated gamma distributed signal, correlated Gaussian processes can be used [3]:

$$\tau_j = \sum_{i=1}^{2\nu} g_{ij}^{\,2}, \qquad j=1,2. \tag{5.9}$$

Thus, each of the texture components has chi-squared distribution with $2v$ degrees of freedom. Given g_{i1}, g_{i2} can be generated using

$$g_{i2} = \rho_g\, g_{i1} + z_i\sqrt{1-\rho_g^{\,2}}, \tag{5.10}$$

where z_i is a zero-mean Gaussian random variable with unit variance.

Correlation coefficient between the texture components is square of the one between the Gaussian components that generate them:

$$\rho_\tau = \rho_g^{\,2} \tag{5.11}$$

The signal is generated as follows: Firstly, spatially partial-correlated texture components for each range cell are generated using the procedure defined above. Then, for each range cell, decorrelated from the other range cells, correlated speckle components are generated. The autocorrelation function of the elements of the speckle component is assumed to have an exponential structure with correlation coefficient ρ_s. Additive noise, with variance σ^2, is also simulated.

Waveform examples of the generated signal are given in Figure 5.1 through Figure 5.3. The signal is simulated to stem from 20 range cells and 8 pulses. The first figure shows the magnitude of vector **r** shown in Equation (5.1). Vector **r** and the video signal have the same elements. The video signal consists of the samples ordered in time. That is, the samples that stem from each pulse are grouped together. However, in vector **r**, the samples from each range cell are grouped together. This can be seen by comparing Figure 5.1 and Figure 5.2. As shown in Figure 5.1, the first N=8 samples are obtained from the first range cell, the following N samples are obtained from the second range cell, and so on. In Figure 5.3, a spikier clutter signal is shown. This corresponds to a lower order parameter, υ of the Gamma distribution. The elements of the speckle component are highly correlated and there is partial correlation between the texture components of different range cells.

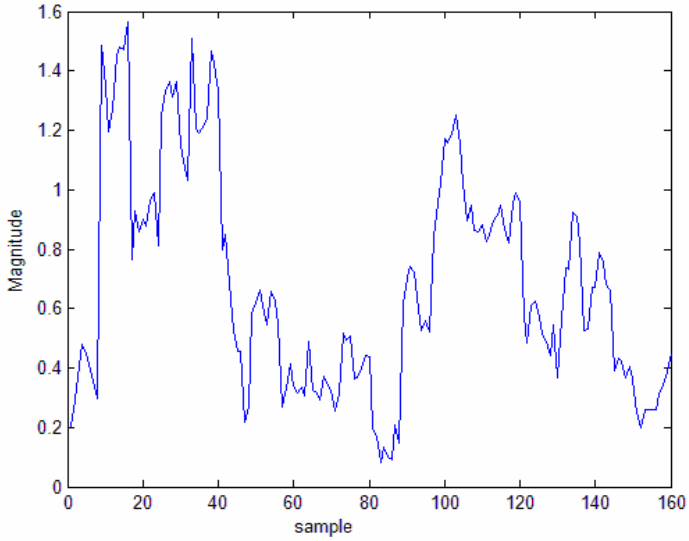

Figure 5.1 Received vector illustration

$M = 20, N = 8, \nu = 2, \mu = 1, \rho_s = 0.99, \rho_t = 0.8, \sigma^2 = 0$

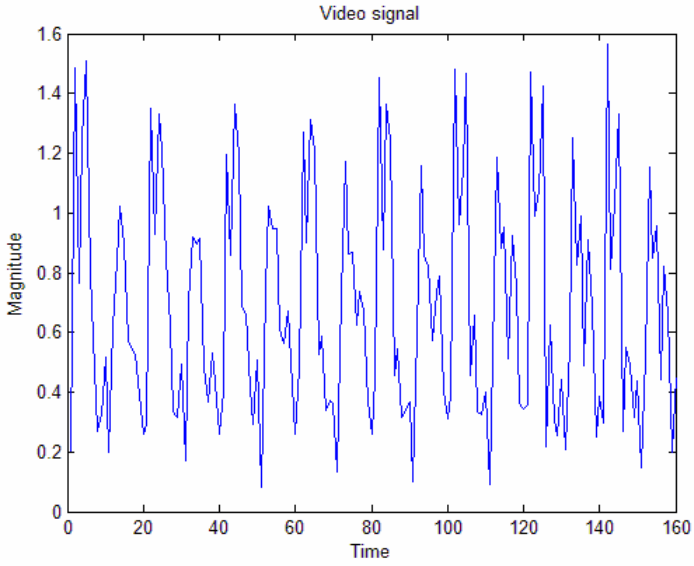

Figure 5.2 Video signal, moderate clutter

$M = 20, N = 8, \nu = 2, \mu = 1, \rho_s = 0.99, \rho_t = 0.8, \sigma^2 = 0$

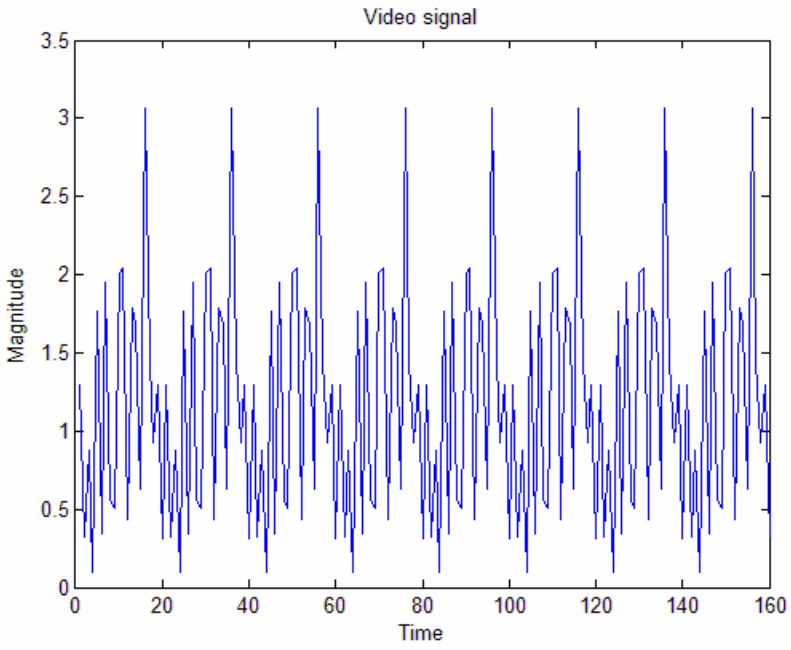

Figure 5.3 Video signal, spiky clutter

$M = 20, N = 8, \nu = 0.5, \mu = 1, \rho_s = 0.99, \rho_t = 0.8, \sigma^2 = 0$

5.2 ML Estimation

In this section, Maximum Likelihood Estimator of the texture component is derived. ML estimate of the texture vector is the one that maximizes the conditional PDF:

$$\mathbf{T}_{\mathrm{ML}} = \arg\max_{\mathbf{T}} \ln p_{\mathbf{r}}(\mathbf{r}|\mathbf{T}) \tag{5.12}$$

Two ML estimators are derived. The first one assumes no-correlation and the second one assumes full-correlation between the texture components.

To be used in evaluating the estimation performance, firstly the Cramer Rao Lower Bound for nonrandom texture parameter estimates is derived.

5.2.1 Cramer-Rao Lower Bound for Nonrandom Texture Parameters

By deriving the Cramer Rao Lower Bound for nonrandom parameter case, performance of the ML estimator can be analyzed.

For the uncorrelated case, the error variance is

$$\sigma_{\hat{\tau}_i}^2 \stackrel{\Delta}{=} Var\left[\hat{\tau}_i(\mathbf{r}) - \tau_i\right] \geq J^{ii} \tag{5.13}$$

where J^{ii} is the ii^{th} element in the matrix J^{-1}.

$$J_{ij} \stackrel{\Delta}{=} -E\left\{\frac{\partial^2 \ln p_{\mathbf{r}|\mathbf{T}}(\mathbf{r}|\mathbf{T})}{\partial\tau_i \partial\tau_j}\right\} \tag{5.14}$$

The partial derivatives are

$$\begin{aligned}\frac{\partial}{\partial\tau_l}\frac{\partial}{\partial\tau_k}\ln p_{\mathbf{r}|\mathbf{T}}(\mathbf{r}|\mathbf{T}) &= \frac{N}{\tau_k^2} - 2\frac{1}{\tau_k^3}\mathbf{r_k}^H\mathbf{M}_x^{-1}\mathbf{r_k} \qquad \text{if } k = l \\ &= 0 \qquad\qquad\qquad\qquad\qquad\quad \text{otherwise}\end{aligned} \tag{5.15}$$

Taking the expectation yields

$$\begin{aligned}E\left\{\frac{\partial^2 \ln p_{\mathbf{r}|\mathbf{T}}(\mathbf{r}|\mathbf{T})}{\partial\tau_k^2}\right\} &= \frac{N}{\tau_k^2} - 2\frac{1}{\tau_k^3}E\left\{\mathbf{r_k}^H\mathbf{M}_x^{-1}\mathbf{r_k}\right\} \\ &= \frac{N}{\tau_k^2} - 2\frac{1}{\tau_k^3}\tau_k E\left\{\mathbf{x_k}^{\mathbf{H}}\mathbf{M_x}^{-1}\mathbf{x_k}\right\} \\ &= \frac{N}{\tau_k^2} - 2\frac{1}{\tau_k^2}N \\ &= -\frac{N}{\tau_k^2}.\end{aligned} \tag{5.16}$$

Hence, the error variance is

$$\sigma_{\tau_k}^{\ 2} \geq \frac{\tau_k^{\ 2}}{N} \tag{5.17}$$

For the full-correlated case, the bound is derived as follows:

Taking the derivative and the expectation yields

$$\begin{aligned} E\left\{\frac{\partial^2 \ln p_{\mathbf{r}|\mathbf{T}}(\mathbf{r}|\mathbf{T})}{\partial \tau^2}\right\} &= \frac{MN}{\tau^2} - 2\frac{1}{\tau^3} E\left\{\mathbf{r_k}^H \mathbf{M}_x^{-1} \mathbf{r_k}\right\} \\ &= \frac{MN}{\tau^2} - 2\frac{1}{\tau^3} \tau\, M\; E\left\{\mathbf{x_k}^{\mathbf{H}} \mathbf{M_x}^{-\mathbf{1}} \mathbf{x_k}\right\} \\ &= -\frac{MN}{\tau^2}. \end{aligned} \tag{5.18}$$

Thus, the error variance is

$$\sigma_{\tau}^{\ 2} \geq \frac{\tau^2}{NM} \tag{5.19}$$

It is expected and can be seen here that the error variance is smaller in fully-correlated case as the number of useful observations increases.

5.2.2 No Spatial Correlation

The conditional PDF of the clutter is

$$p_{\mathbf{r}|\mathbf{T}}(\mathbf{r}|\mathbf{T}) = \frac{1}{\pi^{NM}\left|\mathbf{M_r}\right|} \exp[-\mathbf{r}^H \mathbf{M_r}^{-1} \mathbf{r}] \tag{5.20}$$

If there exists no spatial correlation between the texture components and the correlation structure of the speckle components is identical from range cell-to-range cell, the autocovariance of the clutter is given by:

$$\mathbf{M}_{\mathbf{r}} = \begin{bmatrix} \tau_1 \mathbf{M}_{\mathbf{x}} & 0 & \cdots & 0 \\ 0 & \tau_2 \mathbf{M}_{\mathbf{x}} & \ddots & 0 \\ 0 & 0 & \ddots & 0 \\ 0 & 0 & \cdots & \tau_M \mathbf{M}_{\mathbf{x}} \end{bmatrix}. \tag{5.21}$$

Determinant of the matrix is

$$\left|\mathbf{M}_{\mathbf{r}}\right| = \left(\prod_{i=1}^{M} {\tau_i}^N \right) \left|\mathbf{M}_{\mathbf{x}}\right|^M . \tag{5.22}$$

The inverse of the autocovariance matrix is

$$\mathbf{M}_{\mathbf{r}}^{-1} = \begin{bmatrix} \frac{1}{\tau_1}\mathbf{M}_{\mathbf{x}}^{-1} & 0 & \cdots & 0 \\ 0 & \frac{1}{\tau_2}\mathbf{M}_{\mathbf{x}}^{-1} & \ddots & 0 \\ 0 & 0 & \ddots & 0 \\ 0 & 0 & \cdots & \frac{1}{\tau_2}\mathbf{M}_{\mathbf{x}}^{-1} \end{bmatrix}. \tag{5.23}$$

Maximization of the PDF is equivalent to maximization of its logarithm, which is given by

$$\begin{aligned} \ln p_{\mathbf{r}|\mathbf{T}}(\mathbf{r}|\mathbf{T}) &= -NM \ln \pi - \ln\left|\mathbf{M}_{\mathbf{r}}\right| - \mathbf{r}^H \mathbf{M}_{\mathbf{r}}^{-1} \mathbf{r} \\ &= -NM \ln \pi - N\sum_{i=1}^{M} \ln \tau_i - M\left|\mathbf{M}_{\mathbf{x}}\right| - \sum_{i=1}^{M} \frac{1}{\tau_i} \mathbf{r}_{\mathbf{i}}^H \mathbf{M}_{\mathbf{x}}^{-1} \mathbf{r}_{\mathbf{i}} \end{aligned}. \tag{5.24}$$

Taking the gradient and equating to zero we get the equations given below:

$$\frac{\partial}{\partial \tau_k} \ln p_{\mathbf{r}|\mathbf{T}}(\mathbf{r}|\mathbf{T}) = -\frac{N}{\tau_k} + \frac{1}{{\tau_k}^2} \mathbf{r}_{\mathbf{k}}^H \mathbf{M}_x^{-1} \mathbf{r}_{\mathbf{k}} \tag{5.25}$$

$$-\frac{N}{\tau_{k,ML}}+\frac{1}{\tau_{k,ML}^{\ 2}}\mathbf{r_k}^H\mathbf{M}_x^{-1}\mathbf{r_k}=0\,. \tag{5.26}$$

Hence, the ML estimate can be found using

$$\tau_{k,ML}=\frac{\mathbf{r_k}^H\mathbf{M}_x^{-1}\mathbf{r_k}}{N}\,. \tag{5.27}$$

We can see that expected value of the ML estimate is equal to the actual value:

$$E\{\tau_{k,ML}\}=\frac{E\{\mathbf{r_k}^H\mathbf{M}_x^{-1}\mathbf{r_k}\}}{N}=\frac{\tau_k\ E\{x_\mathbf{k}^H\mathbf{M}_x^{-1}x_\mathbf{k}\}}{N}=\tau_k\,. \tag{5.28}$$

Hence, the estimate is unbiased.

As it can be seen in Figure 5.4, ML estimator can successfully estimate the texture parameters. The first figure shows the ML estimates and the actual values, which are almost equal. The second figure shows the error variance and the CRB. The average value of the error variance is almost equal to the Cramer-Rao-Lower bound in 500 simulations. The third figure shows all of the estimates in 500 simulations, the ensemble. The mean and standard deviation of the estimation is shown in the last figure.

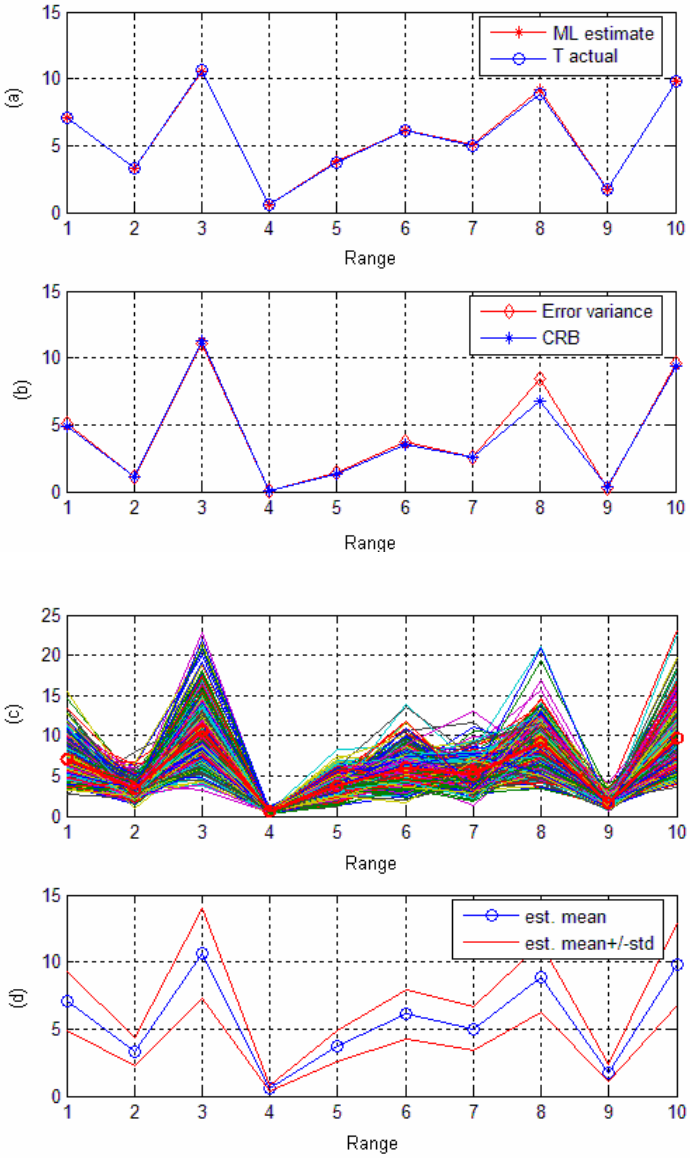

Figure 5.4 Performance of texture parameter estimation

(a) Actual values of texture parameters and their ML estimates, (b) Obtained error variance and CRLB, (c) Ensemble of the estimations, (d) Error mean and standard deviation

M = 10, N = 10, MC = 500, $\nu = 2$, $\mu = 5$, $\sigma^2 = 0$, $\rho_s = 0.5$

5.2.3 Full Spatial Correlation

If the texture components are fully-correlated, i.e. they are identical; the expressions are obtained as follows:

$$\mathbf{r} = \sqrt{\tau}[(x_{11} \quad x_{12} \quad \cdots \quad x_{1N}) \quad (x_{21} \quad x_{22} \quad \cdots \quad x_{2N}) \quad \cdots\cdots \quad (x_{M1} \quad x_{M2} \quad \cdots \quad x_{MN})]^T, \tag{5.29}$$

$$p_{\mathbf{r}|\tau}(\mathbf{r}|\tau) = \frac{1}{\pi^{NM}|\mathbf{M}_\mathbf{r}|}\exp[-\mathbf{r}^H \mathbf{M}_\mathbf{r}^{-1}\mathbf{r}]. \tag{5.30}$$

When there the texture components and the correlation structure of the speckle components is identical from range cell-to-range cell, the autocovariance of the clutter is given by

$$\mathbf{M}_\mathbf{r} = \tau\begin{bmatrix} \mathbf{M}_\mathbf{x} & 0 & \cdots & 0 \\ 0 & \mathbf{M}_\mathbf{x} & \ddots & 0 \\ 0 & 0 & \ddots & 0 \\ 0 & 0 & \cdots & \mathbf{M}_\mathbf{x} \end{bmatrix}. \tag{5.31}$$

Determinant of the matrix is

$$|\mathbf{M}_\mathbf{r}| = \tau^{MN}\,|\mathbf{M}_\mathbf{x}|^M. \tag{5.32}$$

The inverse of the autocovariance matrix is

$$\mathbf{M}_\mathbf{r}^{-1} = \frac{1}{\tau}\begin{bmatrix} \mathbf{M}_\mathbf{x}^{-1} & 0 & \cdots & 0 \\ 0 & \mathbf{M}_\mathbf{x}^{-1} & \ddots & 0 \\ 0 & 0 & \ddots & 0 \\ 0 & 0 & \cdots & \mathbf{M}_\mathbf{x}^{-1} \end{bmatrix}. \tag{5.33}$$

$$\ln p_{\mathbf{r}|\tau}(\mathbf{r}|\tau) = K - MN\ln\tau - M\ln|\mathbf{M}| - \frac{1}{\tau}\mathbf{r}^H\mathbf{M}^{-1}\mathbf{r} \tag{5.34}$$

Taking the gradient and equating to zero we get the equations given below:

$$\frac{\partial}{\partial\tau}\ln p_{\mathbf{r}|\tau}(\mathbf{r}|\tau) = -\frac{MN}{\tau} + \frac{1}{\tau^2}\mathbf{r}^H\mathbf{M}^{-1}\mathbf{r} = 0 \tag{5.35}$$

Hence, the ML estimate can be found using

$$\tau_{ML} = \frac{\sum_{k=1}^{M}\mathbf{r_k}^H\mathbf{M}_x^{-1}\mathbf{r_k}}{NM}. \tag{5.36}$$

This result is expected: It can be interpreted as first finding the power of each cell and then averaging it over all of the range cells. This is equivalent to Cell-Averaging CFAR, which is known to be optimal for homogeneous Rayleigh clutter, or fully correlated texture components.

As expected, the estimate is unbiased:

$$E\{\tau_{ML}\} = \frac{\sum_{k=1}^{M}E\{\mathbf{r_k}^H\mathbf{M}_x^{-1}\mathbf{r_k}\}}{NM} = \frac{\tau\sum_{k=1}^{M}E\{\mathbf{x_k}^H\mathbf{M}_x^{-1}\mathbf{x_k}\}}{MN}. \tag{5.37}$$

$$= \frac{\tau\sum_{k=1}^{M}N}{MN} = \frac{\tau\,MN}{MN} = \tau$$

5.2.4 ML Estimation in Additive Noise Case

The clutter signal contaminated by additive white Gaussian noise can be written as

$$\mathbf{r_i} = \sqrt{\tau_i}\mathbf{x_i} + \mathbf{n_i}\,. \tag{5.38}$$

In this case, the ML estimator derived in Section 5.2.1, for independent texture components yields the expression given below:

$$\begin{aligned}\tau_{k,ML} &= \frac{\mathbf{r_k}^H \mathbf{M}_x^{-1} \mathbf{r_k}}{N} = \frac{\left(\sqrt{\tau_k}\,\mathbf{x_k}^{\mathbf{H}} + n_{\mathbf{k}}{}^H\right)\mathbf{M_x}^{-1}\left(\sqrt{\tau_k}\,\mathbf{x_k} + n_{\mathbf{k}}\right)}{N} \\ &= \frac{\tau_k\left(\mathbf{x_k}^{\mathbf{H}}\mathbf{M_x}^{-1}\mathbf{x_k}\right) + n_{\mathbf{k}}{}^H\mathbf{M_x}^{-1}n_{\mathbf{k}}}{N}\end{aligned} \tag{5.39}$$

The expected value is

$$\begin{aligned}E\{\tau_{k,ML}\} &= \frac{\tau_k E\{\mathbf{x_k}^{\mathbf{H}}\mathbf{M_x}^{-1}\mathbf{x_k}\} + E\{n_{\mathbf{k}}{}^H\mathbf{M_x}^{-1}n_{\mathbf{k}}\}}{N} \\ &= \tau_k + \frac{\sigma^2}{N}Tr(\mathbf{M_x}^{-1})\,,\end{aligned} \tag{5.40}$$

where, σ^2 is the variance of the additive white Gaussian noise.

It can be seen that the estimate has a bias which is not a function of the estimated parameter. Also, assuming that the noise power and speckle covariance matrix are known, it can be calculated and subtracted from the estimate easily.

The equation that is derived for finding the ML estimate for the noisy case is

$$\begin{aligned}&-\frac{1}{2}[-\frac{1}{\tau_k{}^2}\mathbf{r_k}^H\mathbf{M}_x^{-1}\mathbf{r_k} + \sigma^2\mathbf{r_k}^H\left(\mathbf{M}_x^{-1}\right)^2\mathbf{r_k}\,\frac{2\tau_k + \sigma^2 tr(\mathbf{M}_x^{-1})}{[\tau_k{}^2 + \sigma^2\tau_k tr(\mathbf{M}_x^{-1})]^2} \\ &+\frac{e_1(\prod_{i=2}^{N}(\tau_k e_i + \sigma^2)) + (\tau_k e_1 + \sigma^2)(e_2(\prod_{i=3}^{N}(\tau_k e_i + \sigma^2) + (\tau_k e_2 + \sigma^2)(e_3(\prod_{i=4}^{N}\cdots))}{\prod_{i=1}^{N}(\tau_k e_i + \sigma^2)}] \\ &= 0\quad,\end{aligned} \tag{5.41}$$

where, e_i is the i^{th} eigenvalue of $\mathbf{M_x}$.

As seen in Equation (5.41), the expressions are computationally rather complex. In the noisy case, using the ML estimate that was derived in Section 5.2.1, for noiseless case may be preferable since the estimator for noisy case is complex and the bias due to the noise can be subtracted easily from the estimate, as shown by Equation (5.40).

5.3 MAP Estimation

In this section, maximum-a-posteriori estimator of the texture component is derived. For this estimation, the probability density function of the texture process must be available. In the first part, assuming that there exists no spatial correlation between the components, the estimator is obtained. In the second part, full-correlation is assumed. The reason of performing these derivations is their simplicity. They will also be used in verification of the results obtained for partial-correlation, which covers these as special cases.

The Cramer-Rao lower bound for random texture parameter is derived first, with aim of MAP estimator performance evaluation.

5.3.1 Cramer-Rao Lower Bound for Random Texture Parameter

When the estimated parameter is a random variable with known PDF, the mean-square error satisfies the inequality below [59].

$$E\left\{\left|\hat{\tau}(\mathbf{r})-\tau\right|^2\right\}\geq J_T^{ii} \tag{5.42}$$

where J_T^{ii} is the ii^{th} diagonal of the inverse information matrix. The information matrix consists of two parts

$$J_T = J_D + J_P, \tag{5.43}$$

where J_D is the information matrix obtained from the data as given by Equation (5.14). The matrix J_P represents the a-priori information given by the PDF.

Firstly, the bound is derived for no-spatial-correlation case:

$$J_{P,ij} \stackrel{\Delta}{=} -E\left\{\frac{\partial^2 \ln p_{\mathbf{T}}(\mathbf{T})}{\partial \tau_i \partial \tau_j}\right\} \tag{5.44}$$

$$J_{P,ij} \stackrel{\Delta}{=} \begin{cases} -E\left\{(1-\nu)\dfrac{1}{\tau_i^{\,2}}\right\} & i=j, \\ 0 & \text{otherwise} \end{cases} = \begin{cases} (\nu-1)\dfrac{\nu^2}{\mu^2}\dfrac{\Gamma(\nu-2)}{\Gamma(\nu)} & i=j, \\ 0 & \text{otherwise} \end{cases} \tag{5.45}$$

Using Equation (5.43), the information matrix is obtained as

$$J_{T,ii} = \frac{N}{\tau_i^{\,2}} + (\nu-1)\frac{\nu^2}{\mu^2}\frac{\Gamma(\nu-2)}{\Gamma(\nu)} \tag{5.46}$$

Hence, the bound is

$$E\left\{\left|\hat{\tau}_k(\mathbf{r}) - \tau_k\right|^2\right\} \geq \frac{1}{\dfrac{N}{\tau_k^{\,2}} + (\nu-1)\dfrac{\nu^2}{\mu^2}\dfrac{\Gamma(\nu-2)}{\Gamma(\nu)}} \tag{5.47}$$

Similarly, for the full-correlated case, the bound is derived to be:

$$E\left\{\left|\hat{\tau}(\mathbf{r}) - \tau\right|^2\right\} \geq \frac{1}{\dfrac{NM}{\tau^2} + (\nu-1)\dfrac{\nu^2}{\mu^2}\dfrac{\Gamma(\nu-2)}{\Gamma(\nu)}}. \tag{5.48}$$

5.3.2 No Spatial Correlation

ML estimate of the texture vector is the one that maximizes the a-posteriori PDF [59]:

$$\mathbf{T}_{\mathbf{MAP}} = \arg\max_{\mathbf{T}} \ln p_{\mathbf{T}|\mathbf{r}}(\mathbf{T}|\mathbf{r}) \tag{5.49}$$

Logarithm of the a-posteriori PDF is

$$\ln p_{\mathbf{T}|\mathbf{r}}(\mathbf{T}|\mathbf{r}) = \ln p_{\mathbf{r}|\mathbf{T}}(\mathbf{r}|\mathbf{T}) + \ln p_{\mathbf{T}}(\mathbf{T}) - \ln p_{\mathbf{r}}(\mathbf{r}) . \tag{5.50}$$

The last term does not depend on the texture parameter, so it is neglected in maximization.

The logarithm of the texture PDF is

$$\ln p_{\tau}(\tau) = \ln\left[\frac{1}{\Gamma(\nu)}\left(\frac{\nu}{\mu}\right)^{\nu}\right] + (\nu-1)\ln\tau - \frac{\nu}{\mu}\tau , \tag{5.51}$$

derivative of which is

$$\frac{\partial}{\partial\tau}\ln p_{\tau}(\tau) = \frac{(\nu-1)}{\tau} - \frac{\nu}{\mu} .$$

Hence, the partial derivative of the a-posteriori PDF is

$$\frac{\partial}{\partial\tau_k}\ln p_{\mathbf{T}|\mathbf{r}}(\mathbf{T}|\mathbf{r}) = \frac{1}{{\tau_k}^2}\mathbf{r_k}^H\mathbf{M}_x^{-1}\mathbf{r_k} + (\nu-1-N)\frac{1}{\tau_k} - \frac{\nu}{\mu} . \tag{5.52}$$

By equating this expression to zero,

$$\frac{1}{{\tau_{k,MAP}}^2}\mathbf{r_k}^H\mathbf{M}_x^{-1}\mathbf{r_k} + (\nu-1-N)\frac{1}{\tau_{k,MAP}} - \frac{\nu}{\mu} = 0 , \tag{5.53}$$

and solving the equation for the MAP estimate,

$$\tau_{k,MAP} = \frac{\mu}{2\nu}(\nu - N - 1) + \frac{1}{2\nu}\sqrt{\mu\,(\mu\,(N+1-\nu)^2 + 4\nu\,\mathbf{r_k}^H \mathbf{M}_x^{-1}\mathbf{r_k}} \qquad (5.54)$$

is obtained.

The term $\mathbf{r_k}^H \mathbf{M}_x^{-1}\mathbf{r_k}$ has a central chi-squared distribution with degree of freedom *N*. Then, the expected value of the MAP estimate is evaluated as

$$E\{\tau_{k,MAP}\} = \frac{\sqrt{2B}\,\Gamma(\frac{N+1}{2})\;{}_1F_1(-\frac{1}{2},\frac{1-N}{2},\frac{A}{2B})}{\Gamma(\frac{N}{2})} \qquad (5.55)$$
$$-\frac{1}{\sqrt{\pi}}(2^{-1-N/2}\sqrt{A}(\frac{A}{B})^{N/2}\Gamma(-\frac{N+1}{2})_1F_1(\frac{N}{2},\frac{3-N}{2},\frac{A}{2B}) \;,$$

where

$$A \overset{\Delta}{=} (\mu(N+1-\nu))^2,$$

$$B \overset{\Delta}{=} 4\mu\tau\nu\,.$$

Here, $\Gamma(\cdot)$ is the Gamma function and ${}_1F_1(\cdot)$ is the Hypergeometric function.

5.3.3 Full Spatial Correlation

In the fully-correlated case, logarithm of the a-posteriori PDF can be obtained as follows:

$$\frac{\partial}{\partial\tau}\ln p_{\tau|\mathbf{r}}(\tau|\mathbf{r}) = \frac{1}{\tau^2}\sum_{k=1}^{M}\mathbf{r_k}^H\mathbf{M}_x^{-1}\mathbf{r_k} + (\nu - 1 - NM)\frac{1}{\tau} - \frac{\nu}{\mu}. \qquad (5.56)$$

Equating this to zero,

$$\frac{1}{\tau_{MAP}^{\ 2}}\sum_{k=1}^{M}\mathbf{r_k}^{H}\mathbf{M}_x^{-1}\mathbf{r_k}+(\nu-1-NM)\frac{1}{\tau_{MAP}}-\frac{\nu}{\mu}=0, \tag{5.57}$$

and solving the equation, the MAP estimate is obtained as

$$\tau_{MAP}=\frac{\mu}{2\nu}(\nu-NM-1)+\frac{1}{2\nu}\sqrt{\mu\,(\mu\,(NM+1-\nu)^2+4\nu\sum_{k=1}^{M}\mathbf{r_k}^{H}\mathbf{M}_x^{-1}\mathbf{r_k}}\ . \tag{5.58}$$

5.3.4 Partial Spatial Correlation

The PDF expressions of the received vector and the partially-correlated texture component, which were given by Equations (5.6), (5.7) and (5.8), are repeated here for convenience:

$$p(\mathbf{r_1},\mathbf{r_2},\cdots\mathbf{r_M})=\int_0^\infty\cdots\int_0^\infty p_{\mathbf{T}}(\mathbf{T})\frac{1}{(2\pi)^M|\mathbf{M_s}|}\prod_{n=1}^{M}\frac{1}{\tau_n}\exp(-\frac{1}{2\tau_n}\mathbf{r}_n^{\ H}\mathbf{M_s^{-1}}\mathbf{r}_n)\,d\tau_1\cdots d\tau_M \tag{5.59}$$

Correlation structure of the texture component is inherent in

$$p_{\mathbf{T}}(\mathbf{T})=p_{\tau_2|\tau_1}(\tau_M|\tau_{M-1})\;p_{\tau_2|\tau_1}(\tau_{M-1}|\tau_{M-2})\cdots p_{\tau_2|\tau_1}(\tau_2|\tau_1), \tag{5.60}$$

where

$$\begin{aligned}p_{\tau_1|\tau_0}(\tau_m|\tau_{m-1})=&\frac{\nu}{\mu}\frac{1}{\rho_\tau^{(\nu-1)/2}(1-\rho_\tau)}(\frac{\tau_m}{\tau_{m-1}})^{\frac{\nu-1}{2}}\\&\times\exp[-\frac{\nu}{\mu}\frac{\tau_m+\rho_\tau\tau_{m-1}}{1-\rho_\tau}]\,I_{\nu-1}[\frac{\nu}{\mu}\frac{1}{(1-\rho_\tau)}\sqrt{\rho_\tau\tau_m\tau_{m-1}}]\end{aligned}. \tag{5.61}$$

In these expressions, ρ_τ is the one-lag correlation coefficient.

Substituting equation (5.61) in (5.60), the following expression is obtained:

$$
\begin{aligned}
p_T(T) = {} & A^{M-1}\rho_\tau^{(M-1)(1-\nu)/2}\left(\frac{\tau_M}{\tau_1}\right)^{\frac{\nu-1}{2}}\exp[-A\sum_{i=2}^{M}\tau_i+\rho_\tau\tau_{i-1}] \\
& \times I_{\nu-1}[A\sqrt{\rho_\tau\tau_M\tau_{M-1}}]\times I_{\nu-1}[A\sqrt{\rho_\tau\tau_{M-1}\tau_{M-2}}]\times\cdots\times I_{\nu-1}[A\sqrt{\rho_\tau\tau_2\tau_1}] \\
& \times\frac{1}{\Gamma(\nu)}\left(\frac{\nu}{\mu}\right)^{\nu}\tau_1^{\nu-1}\exp[-\frac{\nu}{\mu}\tau_1]
\end{aligned}
\tag{5.62}
$$

where $A\overset{\Delta}{=}\frac{\nu}{\mu}\frac{1}{(1-\rho_\tau)}$.

Logarithm of this expression is

$$
\begin{aligned}
\ln p_T(T) = {} & K+\frac{\nu-1}{2}[\ln\tau_M-\ln\tau_1]-A\sum_{i=2}^{M}(\tau_i+\rho_\tau\tau_{i-1}) \\
& +\sum_{i=2}^{M}\ln I_{\nu-1}[A\sqrt{\rho_\tau\tau_i\tau_{i-1}}]+(\nu-1)\ln\tau_1-\frac{\nu}{\mu}\tau_1 \quad .
\end{aligned}
\tag{5.63}
$$

Next the gradient of the expression is evaluated. Due to asymmetry of the expressions, derivatives with respect to τ_m, for m=1, m=M and the other intermediate components are taken separately:

$$
\frac{\partial}{\partial\tau_1}\ln p_T(T)=\frac{\nu-1}{2\,\tau_1}-A\rho_\tau-\frac{\nu}{\mu}+\frac{A\,\tau_2\rho_\tau I_{\nu-2}[A\sqrt{\rho_\tau\tau_1\tau_2}]+I_\nu[A\sqrt{\rho_\tau\tau_1\tau_2}]}{4\sqrt{\rho_\tau\tau_1\tau_2}\;I_{\nu-1}[A\sqrt{\rho_\tau\tau_1\tau_2}]}; \tag{5.64}
$$

$$
\frac{\partial}{\partial\tau_M}\ln p_T(T)=\frac{\nu-1}{2\,\tau_M}-A+\frac{A\,\tau_{M-1}\rho_\tau I_{\nu-2}[A\sqrt{\rho_\tau\tau_M\tau_{M-1}}]+I_\nu[A\sqrt{\rho_\tau\tau_M\tau_{M-1}}]}{4\sqrt{\rho_\tau\tau_M\tau_{M-1}}\;I_{\nu-1}[A\sqrt{\rho_\tau\tau_M\tau_{M-1}}]}; \tag{5.65}
$$

$$
\begin{aligned}
\frac{\partial}{\partial\tau_m}\ln p_T(T) = {} & -A+\rho_\tau+\frac{1}{4}A\rho_\tau[\frac{\tau_{m-1}\;I_{\nu-2}[A\sqrt{\rho_\tau\tau_m\tau_{m-1}}]+I_\nu[A\sqrt{\rho_\tau\tau_m\tau_{m-1}}]}{\sqrt{\rho_\tau\tau_m\tau_{m-1}}\;I_{\nu-1}[A\sqrt{\rho_\tau\tau_m\tau_{m-1}}]} \\
& +\frac{\tau_{m+1}\;I_{\nu-2}[A\sqrt{\rho_\tau\tau_m\tau_{m+1}}]+I_\nu[A\sqrt{\rho_\tau\tau_m\tau_{m+1}}]}{\sqrt{\rho_\tau\tau_m\tau_{m+1}}\;I_{\nu-1}[A\sqrt{\rho_\tau\tau_m\tau_{m+1}}]}] \quad ,
\end{aligned}
\tag{5.66}
$$

for m=2,3,…, M-1.

Now, in order to maximize the a-posteriori PDF, the set of equations given below should be solved:

$$-\frac{N}{\tau_{m,MAP}}+\frac{1}{\tau_{m,MAP}^{\ 2}}\mathbf{r}_m^{\ H}\mathbf{M}_x^{\ -1}\mathbf{r}_m+\frac{\partial}{\partial\tau_m}\ln p_{\mathbf{T}}(\mathbf{T})\Big|_{\tau_m=\tau_{m,MAP}}=0 \tag{5.67}$$

for m=1,2,…,M.

Solution of the above set of equations is not trivial. For this purpose, Newton's Method [39] is utilized. In this method, the following iteration is carried out to find the MAP estimate of the texture vector, $\mathbf{T}_{MAP}$:

$$\mathbf{T}_{MAP,(n+1)}=\mathbf{T}_{MAP,(n)}-\left[F'(\mathbf{T}_{MAP,(n)})\right]^{-1}F(\mathbf{T}_{MAP,(n)}), \tag{5.68}$$

where

$$F(\mathbf{T})=\begin{bmatrix}-\frac{N}{\tau_1}+\frac{1}{\tau_1^{\ 2}}\mathbf{r}_1^{\ H}\mathbf{M}_x^{\ -1}\mathbf{r}_1+\frac{\partial}{\partial\tau_1}\ln p_{\mathbf{T}}(\mathbf{T})\\ \vdots\\ -\frac{N}{\tau_M}+\frac{1}{\tau_M^{\ 2}}\mathbf{r}_M^{\ H}\mathbf{M}_x^{\ -1}\mathbf{r}_M+\frac{\partial}{\partial\tau_M}\ln p_{\mathbf{T}}(\mathbf{T})\end{bmatrix}\overset{\Delta}{=}\begin{bmatrix}f_1\\ \vdots\\ f_M\end{bmatrix} \tag{5.69}$$

is the function roots of which are to be found. The matrix $F'(\mathbf{T})$ is determined from

$$F'(\mathbf{T})\overset{\Delta}{=}\begin{bmatrix}\partial f_1/\partial\tau_1 & \partial f_1/\partial\tau_2 & \cdots & \partial f_1/\partial\tau_M\\ \partial f_2/\partial\tau_1 & \partial f_2/\partial\tau_2 & \cdots & \partial f_2/\partial\tau_M\\ \vdots & \vdots & \ddots & \vdots\\ \partial f_M/\partial\tau_1 & \partial f_M/\partial\tau_2 & \cdots & \partial f_M/\partial\tau_M\end{bmatrix}. \tag{5.70}$$

5.4 Performance Analysis

In this section, performance analyses of the estimators are presented. The simulations are performed by generating N_T texture vectors and N_S speckle components for each texture vector. The parameter ρ_s is the correlation coefficient of the speckle and ρ_t is the correlation coefficient of the texture.

Figure 5.5 shows the performance in a different scenario, where a large number of simulations are performed for the speckle and the texture generation. Here, 1dB average improvement is obtained by using MAP estimate.

The next simulation shows the improvement of MAP over ML in fully correlated texture scenario. The result can be seen in Figure 5.6. The bounds on the estimation error variance are also given in the figure. As expected, the MAP yields better estimation than the ML estimate. The ML estimate is closer to the CRB derived for nonrandom parameters when compared to the MAP estimate, the error of which is rather higher than the CRB for random parameters.

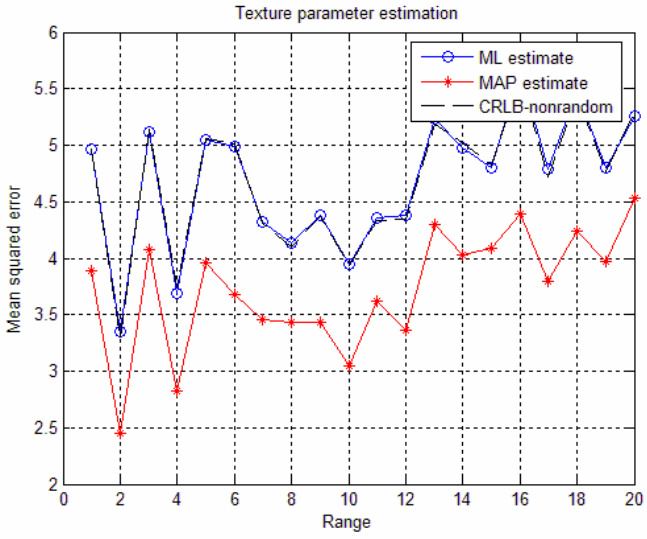

Figure 5.5 Mean squared estimation error (no correlation)

M = 20, N = 8, N_S = 1000, N_T = 100, ν = 2, μ = 5, σ^2 = 0, ρ_s = 0.5, ρ_t= 0

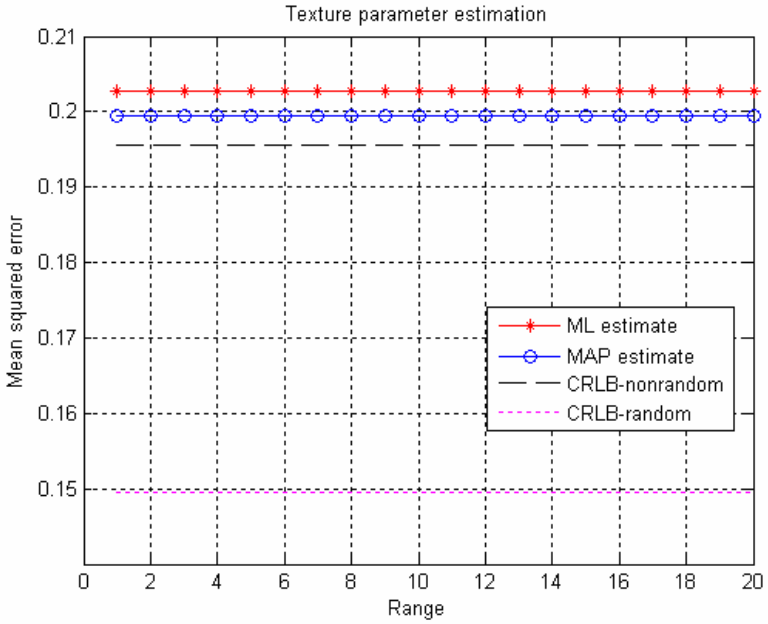

Figure 5.6 Mean squared estimation error (full correlation)

M = 20, N = 8, N_S = 1000, N_T = 100, ν = 2, μ = 5, σ^2 = 0, ρ_s = 0.5, ρ_t= 1

Performance of the MAP estimator for partial spatial correlation developed in Section 5.3.4 was obtained through simulations. Improvement obtained by using MAP instead of ML in partial correlated texture scenario can be seen in Figure 5.7. On the other hand, in partial correlation case, in some cases, the estimator diverges. In order to avoid this behavior, some checks are performed during the estimation process. The first one is the check for the condition of the matrix in the Newton's method. If it is found to be ill-conditioned, the estimation is equated to the ML estimate. The second check is on the magnitude of the estimates, if they are greater than a predetermined value; the estimation is equated to the ML estimate. Additionally, the initial point of the Newton's iteration is ML estimates.

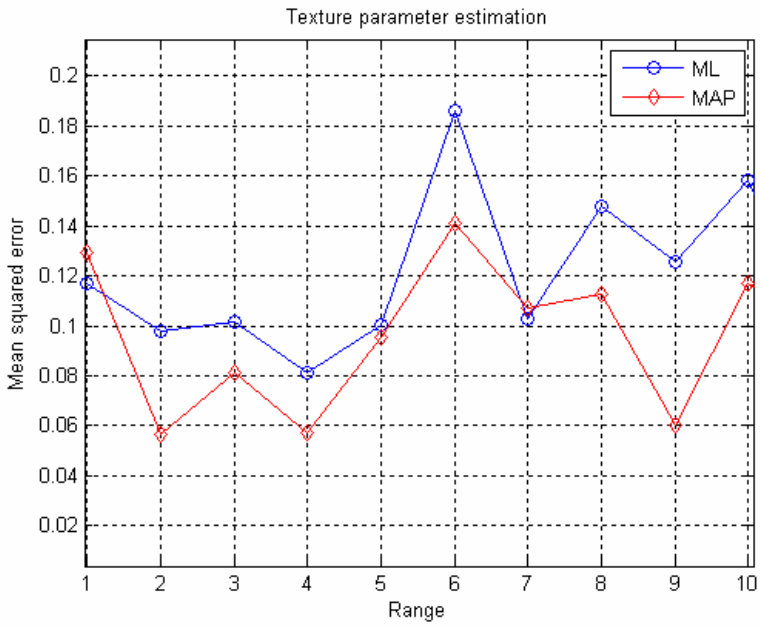

Figure 5.7 Mean squared estimation error (partial correlation)

M = 20, N = 8, N_S = 1000, N_T = 100, ν = 2, μ = 1, σ^2 = 0, ρ_s = 0.5, ρ_t= 0.5

CHAPTER 6

COHERENT DETECTION

Coherent detection of targets in a correlated non-Gaussian clutter environment is an important problem that draws much attention of the radar community. This method makes use of the phase information and yields better results than the classical incoherent detection techniques. On the other hand, the main difficulties in design of a detector are modeling the disturbance and the mathematical tractability of the detector.

In this chapter, adopting the compound Gaussian model and the notation given in Section 2.2.2, detectors are derived. The detectors use the samples from all of the range cells and perform clutter suppression, Doppler processing and CFAR operations simultaneously. The detectors are derived for no-spatial correlation, full-spatial correlation and partial-correlation scenarios. The correlation structure of the speckle component is assumed to be known and the texture parameter is estimated using the methods derived in the previous chapter.

In the design of the detectors, the clutter signal is assumed to be dominant and the thermal noise is neglected. This is a common assumption made in the works on detection in clutter. Although the effect of the noise may be important when the clutter and noise have comparable powers, since the signal that is input to the coherent detector contains unsuppressed clutter, this may still be a valid assumption.

6.1 Detector

Assuming that the radar transmits N pulses and the receiver demodulates and samples the echo signal forming M range cells, the received clutter vector will be:

$$\mathbf{r} = \left[\sqrt{\tau_1}\left(x_{11} \quad x_{12} \quad \cdots \quad x_{1N}\right) \quad \sqrt{\tau_2}\left(x_{21} \quad x_{22} \quad \cdots \quad x_{2N}\right) \quad \cdots \quad \sqrt{\tau_M}\left(x_{M1} \quad x_{M2} \quad \cdots \quad x_{MN}\right)\right]^T \quad (6.1)$$

Here, τ_i and x_{ij}'s are the texture and speckle parameters, respectively as defined in the previous chapter.

Let the received signals under no target hypothesis (H_0) and target existence hypothesis (H_1) be represented as

$$H_0: \quad \mathbf{r}_i = \sqrt{\tau_i}\ \mathbf{x}_i \quad . \qquad (6.2)$$

$$H_1: \quad \mathbf{r}_i = \sqrt{\tau_i}\ \mathbf{x}_i + \mathbf{s}_i \qquad (6.3)$$

The target signal is assumed to be located in one range cell, at the L^{th} range bin:

$$\begin{aligned} \mathbf{s} &\overset{\Delta}{=} \left[\mathbf{0} \quad \mathbf{0} \quad \cdots \quad \mathbf{s}_L \quad \cdots \mathbf{0}\right]^T \\ \mathbf{s}_L &\overset{\Delta}{=} \alpha \mathbf{p}^{\mathbf{T}} \end{aligned} \qquad (6.4)$$

where α represents the complex return from the target and $\mathbf{p}$ represents the Doppler steering vector:

$$\begin{aligned} \mathbf{p} &\overset{\Delta}{=} \left[p_0 \quad p_1 \quad \cdots \quad p_{N-2} \quad p_{N-1}\right]^T \\ p_i &= \exp(j2\pi\, i\, f_D T) \end{aligned} \qquad (6.5)$$

The likelihood-ratio test is [59]

$$\Lambda(\mathbf{r}) = \frac{p_{\mathbf{r}|H_1}(\mathbf{r}|H_1)}{p_{\mathbf{r}|H_0}(\mathbf{r}|H_0)} \underset{H_0}{\overset{H_1}{\gtrless}} \gamma \quad . \tag{6.6}$$

The likelihood function (conditional PDF) of the received signal conditioned on H_0 is

$$p_{\mathbf{r}|H_0}(\mathbf{r}|H_0) = \frac{1}{\pi^{NM}|\mathbf{M}_\mathbf{r}|} \exp[-\mathbf{r}^H \mathbf{M}_\mathbf{r}^{-1} \mathbf{r}] . \tag{6.7}$$

Here, $\mathbf{M_r}$ is the covariance matrix of the received signal.

In the following subsections, the detectors for uncorrelated, partially-correlated and fully-correlated texture cases are derived.

Although it changes depending on the detector, the threshold parameter is represented by the same symbol for convenience.

6.1.1 No Spatial Correlation

In spatially-independent texture case, the covariance matrix, $\mathbf{M_r}$, its inverse and determinant are given by Equations (5.21) - (5.23).

The log-likelihood functions under hypotheses H_0 and H_1 are

$$\begin{aligned} \ln p_{\mathbf{r}|\mathbf{T},H_0}(\mathbf{r}|\mathbf{T},H_0) &= -NM \ln \pi - \ln|\mathbf{M}_r| - \mathbf{r}^H \mathbf{M}_r^{-1} \mathbf{r} \\ &= -NM \ln \pi - N\sum_{i=1}^{M} \ln \tau_i - M|\mathbf{M}_\mathbf{x}| - \sum_{i=1}^{M} \frac{1}{\tau_i} \mathbf{r_i}^H \mathbf{M_x}^{-1} \mathbf{r_i} \quad , \end{aligned} \tag{6.8}$$

$$\begin{aligned}\ln p_{\mathbf{r}|\mathbf{T},H_1}(\mathbf{r}|\mathbf{T},H_1) &= -NM\ln\pi - \ln|\mathbf{M}_r| - (\mathbf{r}-\mathbf{s})^H \mathbf{M}_r^{-1}(\mathbf{r}-\mathbf{s}) \\ &= -NM\ln\pi - N\sum_{i=1}^{M}\ln\tau_i - M|\mathbf{M}_\mathbf{x}| \\ &\quad -\sum_{\substack{i=1\\ i\neq L}}^{M}\frac{1}{\tau_i}\mathbf{r_i}^H\mathbf{M}_\mathbf{x}^{-1}\mathbf{r_i} - \frac{1}{\tau_L}(\mathbf{r}_L-\mathbf{s}_L)^H\mathbf{M}_\mathbf{x}^{-1}(\mathbf{r}_L-\mathbf{s}_L) \quad .\end{aligned} \tag{6.9}$$

The Log-Likelihood Ratio Test is

$$\ln p_{\mathbf{r}|\mathbf{T},H_1}(\mathbf{r}|\mathbf{T},H_1) - \ln p_{\mathbf{r}|\mathbf{T},H_0}(\mathbf{r}|\mathbf{T},H_0) \underset{H_0}{\overset{H_1}{\gtrless}} \gamma. \tag{6.10}$$

If the texture component is known, the test becomes,

$$-(\mathbf{r}_L-\mathbf{s}_L)^H\mathbf{M}_r^{-1}(\mathbf{r}_L-\mathbf{s}_L) + \mathbf{r}_L{}^H\mathbf{M}_r^{-1}\mathbf{r}_L \underset{H_0}{\overset{H_1}{\gtrless}} \gamma \tag{6.11}$$

which is equivalent to

$$2\,\mathrm{Re}\left\{\mathbf{s}_L{}^H\mathbf{M}_x^{-1}\mathbf{r}_L\right\} \underset{H_0}{\overset{H_1}{\gtrless}} \mathbf{s}_L{}^H\mathbf{M}_x^{-1}\mathbf{s}_L + \gamma. \tag{6.12}$$

The left-hand-side of the above test is a whitening-matched filter and the right hand side is a fixed threshold.

When the texture component is a random parameter with known density function, the LRT can be written as follows:

$$\frac{p_{\mathbf{r}|H_1}(\mathbf{r}|H_1)}{p_{\mathbf{r}|H_0}(\mathbf{r}|H_0)} = \frac{\int_0^\infty p_{\mathbf{r}|H_1}(\mathbf{r}|H_1)\; p_\tau(\tau)\, d\tau}{\int_0^\infty p_{\mathbf{r}|H_0}(\mathbf{r}|H_0)\; p_\tau(\tau)\, d\tau} \underset{H_0}{\overset{H_1}{\gtrless}} \lambda\,. \tag{6.13}$$

This LRT is usually difficult to evaluate and it is optimum only for the density function used in the design time, which is not suitable for signals with different density functions.

However, if the texture component is assumed to be an unknown nonrandom parameter and is estimated using ML estimation, the test is called Generalized Likelihood Test (GLRT) [59]. This derivation is more general as the clutter may have a different distribution than the one assumed in the design time.

For the fully-correlated texture case, the GLRT can be written as

$$\Lambda_g(\mathbf{r}) = \frac{\max_{\tau_1} p_{\mathbf{r}|\tau_1,H_1}(\mathbf{r}|\tau_1,H_1)}{\max_{\tau_0} p_{\mathbf{r}|\tau_0,H_0}(\mathbf{r}|\tau_0,H_0)} \underset{H_0}{\overset{H_1}{\gtrless}} \gamma\,. \tag{6.14}$$

The ML estimate of the texture parameter under H_0 for independent texture case was derived in Section 5.2.1 and is written here for convenience:

$$\tau_{L,ML,0} = \frac{\mathbf{r}_L{}^H \mathbf{M}_x{}^{-1} \mathbf{r}_L}{N}\,. \tag{6.15}$$

Under H_1, taking the gradient of the likelihood function and equating it to zero we get the equation

$$\frac{\partial}{\partial \tau} \ln p_{\mathbf{r}|\tau_L,H_1}(\mathbf{r}|\tau_L,H_1) = -\frac{MN}{\tau_L} + \frac{1}{\tau_L{}^2}(\mathbf{r}_L - \mathbf{s}_L)^H \mathbf{M}^{-1}(\mathbf{r}_L - \mathbf{s}_L)\Big|_{\tau_L=\tau_{L,ML,1}} = 0\,. \tag{6.16}$$

Hence, the ML estimate at H_1 can be found as

$$\tau_{L,ML,1} = \frac{(\mathbf{r}_L - \mathbf{s}_L)^H \mathbf{M}_x^{-1} (\mathbf{r}_L - \mathbf{s}_L)}{N}. \tag{6.17}$$

For the compound-Gaussian case, when the texture parameters are estimated the LRT given by Equation (6.10) yields the GLRT:

$$-\left[NM \ln(\tau_{L,ML,1} / \tau_{L,ML,0})\right] \underset{H_0}{\overset{H_1}{\gtrless}} \gamma. \tag{6.18}$$

It is interesting to see that the ratio of the estimates under the hypothesis 0 and 1 is a sufficient statistics. Obviously, the estimates are not perfect and the ratio can discriminate between the two hypotheses, otherwise, the test would be useless.

Substituting the estimates and simplifying, the following test is obtained:

$$\frac{\mathbf{r}_L{}^H \mathbf{M}_x^{-1} \mathbf{r}_L}{(\mathbf{r}_L - \alpha \mathbf{p})^H \mathbf{M}_x^{-1} (\mathbf{r}_L - \alpha \mathbf{p})} \underset{H_0}{\overset{H_1}{\gtrless}} \gamma. \tag{6.19}$$

Equation (6.19) is equivalent to

$$\frac{\mathbf{r}_L{}^H \mathbf{M}_x^{-1} \mathbf{r}_L}{\mathbf{r}_L{}^H \mathbf{M}_x^{-1} \mathbf{r}_L + |\alpha|^2 \mathbf{p}^H \mathbf{M}_x^{-1} \mathbf{p} - 2\,\mathrm{Re}\left\{\alpha^* \mathbf{p}^H \mathbf{M}_x^{-1} \mathbf{r}_L\right\}} \underset{H_0}{\overset{H_1}{\gtrless}} \gamma. \tag{6.20}$$

Assuming that the Doppler steering vector is known but the complex target return is unknown, ML estimate of the complex target return can be substituted to obtain the GLRT. Steering vector can be known in radar systems, since generally a bank of Doppler detectors is used. If this is not done, a suitable method must be used in order

to estimate the Doppler also. It should be noted that the estimation of the texture and target returns do not depend on each other and this estimation is equivalent to joint estimation of the parameters.

Taking derivative with respect to the target return and equating to zero,

$$\frac{\partial}{\partial \alpha}[-(\mathbf{r}_L - \alpha \mathbf{p})^H \mathbf{M}_x^{-1}(\mathbf{r}_L - \alpha \mathbf{p})]\Big|_{\alpha=a_{ML}} = 0\,, \tag{6.21}$$

$$-(-\mathbf{r}_L^H \mathbf{M}_x^{-1}\mathbf{p} + \alpha^* \mathbf{p}^H \mathbf{M}_x^{-1}\mathbf{p})\Big|_{\alpha=a_{ML}} = 0\,, \tag{6.22}$$

the ML estimate of the target return is found as

$$\alpha_{ML} = \frac{\mathbf{p}^H \mathbf{M}_x^{-1}\mathbf{r}_L}{\mathbf{p}^H \mathbf{M}_x^{-1}\mathbf{p}}\,. \tag{6.23}$$

Substituting this estimate in the test given by Equation (6.20) yields

$$\frac{\left|\mathbf{p}^H \mathbf{M}_x^{-1}\mathbf{r}_L\right|^2}{(\mathbf{r}_L^H \mathbf{M}_x^{-1}\mathbf{r}_L)\,(\mathbf{p}^H \mathbf{M}_x^{-1}\mathbf{p})} \underset{H_0}{\overset{H_1}{\gtrless}} \gamma\,. \tag{6.24}$$

This detector is identical to the one derived before in [26] and [14] for a single-range cell. However, for multiple-range cells, the multiple-cell detector is general and advantageous.

6.1.2 Full Spatial Correlation

In this part, it is assumed that the texture component is identical (fully-correlated) in each range cell, that is $\tau_1 = \tau_2 = \cdots = \tau_M \overset{\Delta}{=} \tau$. This is a valid assumption, for small range cell sizes.

In fully-correlated (identical) texture case, the covariance matrix, $\mathbf{M_r}$, the inverse matrix and the determinant are given by Equations (5.31)-(5.33).

The logarithms of the likelihood functions are

$$\ln p_{\mathbf{r}|\tau,H_0}(\mathbf{r}|\tau,H_0) = -MN\ln\pi - \ln|\mathbf{M}_r| - \mathbf{r}^H\mathbf{M}_r^{-1}\mathbf{r}, \tag{6.25}$$

$$\ln p_{\mathbf{r}|\tau,H_1}(\mathbf{r}|\tau,H_1) = -MN\ln\pi - \ln|\mathbf{M}_r| - (\mathbf{r}-\mathbf{s})^H\mathbf{M}_r^{-1}(\mathbf{r}-\mathbf{s}). \tag{6.26}$$

If the texture component is known, the Log-Likelihood Ratio Test (LRT) is

$$-(\mathbf{r}-\mathbf{s})^H\mathbf{M}_r^{-1}(\mathbf{r}-\mathbf{s}) + \mathbf{r}^H\mathbf{M}_r^{-1}\mathbf{r} \underset{H_0}{\overset{H_1}{\gtrless}} \gamma. \tag{6.27}$$

However, since the texture component is unknown, it should be estimated. The ML estimate of the texture component under H_0 for fully-correlated case was derived in Section 5.2.2 and is repeated here for convenience:

$$\tau_{ML,0} = \frac{\sum_{i=1}^{M}\mathbf{r}_i^H\mathbf{M}_x^{-1}\mathbf{r}_i}{NM}. \tag{6.28}$$

Under H_1, taking the gradient of the likelihood function and equating it to zero we get the equations given below:

$$\frac{\partial}{\partial\tau}\ln p_{\mathbf{r}|\tau,H_1}(\mathbf{r}|\tau,H_1) = -\frac{MN}{\tau} + \frac{1}{\tau^2}(\mathbf{r}-\mathbf{s})^H\mathbf{M}^{-1}(\mathbf{r}-\mathbf{s})\Big|_{\tau=\tau_{ML,1}} = 0. \tag{6.29}$$

Hence, the ML estimate under H_1 can be found as

$$\tau_{ML,1} = \frac{\sum_{i=1,i\neq L}^{M} \mathbf{r}_i^H \mathbf{M}_x^{-1} \mathbf{r}_i + (\mathbf{r}_L - \alpha \mathbf{p})^H \mathbf{M}_x^{-1} (\mathbf{r}_L - \alpha \mathbf{p})}{NM}. \tag{6.30}$$

Hence, the GLRT is obtained as

$$\tau_{ML,0} / \tau_{ML,1} \underset{H_0}{\overset{H_1}{\gtrless}} \gamma. \tag{6.31}$$

This detector is equivalent to the one given by Equation (6.18) and uses the ratio of the estimates for the two hypotheses.

Substituting the estimates, the following test is obtained:

$$\frac{\sum_{i=1}^{M} \mathbf{r}_i^H \mathbf{M}_x^{-1} \mathbf{r}_i}{\sum_{i=1,i\neq L}^{M} \mathbf{r}_i^H \mathbf{M}_x^{-1} \mathbf{r}_i + (\mathbf{r}_L - \alpha \mathbf{p})^H \mathbf{M}_x^{-1} (\mathbf{r}_L - \alpha \mathbf{p})} \underset{H_0}{\overset{H_1}{\gtrless}} \gamma, \tag{6.32}$$

which is equivalent to

$$\frac{\sum_{i=1}^{M} \mathbf{r}_i^H \mathbf{M}_x^{-1} \mathbf{r}_i}{\sum_{i=1}^{M} \mathbf{r}_i^H \mathbf{M}_x^{-1} \mathbf{r}_i + |\alpha|^2 \mathbf{p}^H \mathbf{M}_x^{-1} \mathbf{p} - 2\,\mathrm{Re}\left\{\alpha^* \mathbf{p}^H \mathbf{M}_x^{-1} \mathbf{r}_L\right\}} \underset{H_0}{\overset{H_1}{\gtrless}} \gamma. \tag{6.33}$$

The ML estimate of the complex target return was given in the previous section by Equation (6.23). When it is substituted in the detector given in Equation (6.33), the detector is obtained as

$$\frac{\left|\mathbf{p}^H \mathbf{M}_x^{-1} \mathbf{r}_L\right|^2}{(\sum_{i=1}^{M} \mathbf{r}_i^H \mathbf{M}_x^{-1} \mathbf{r}_i)(\mathbf{p}^H \mathbf{M}_x^{-1} \mathbf{p})} \underset{H_0}{\overset{H_1}{\gtrless}} \gamma. \tag{6.34}$$

As expected, for a single range cell, M=1, the detector derived above is equivalent to the one in the independent-texture case:

$$\frac{\left|\mathbf{p}^H \mathbf{M}_x^{-1} \mathbf{r}_L\right|^2}{(\mathbf{p}^H \mathbf{M}_x^{-1} \mathbf{p})(\mathbf{r}_L^H \mathbf{M}_x^{-1} \mathbf{r}_L)} \underset{H_0}{\overset{H_1}{\gtrless}} \gamma. \tag{6.35}$$

The detectors are summarized in Table 6.1. It should be noted that in the listed detectors, the threshold parameters, γ's, are not equal.

The multiple-cell detector has an advantage over the single cell detector by since it averages the returns of all of the range cells and improves the estimation.

Next, performance of the detector is analyzed. In the first part of the simulations, Swerling 0 target is considered. In the second part, Swerling 1 target case is simulated. The clutter is assumed to have K-distribution. Although the distribution is not exploited in derivation of the detector, it is used in generation of the simulation signals.

Table 6.1 Summary of detectors

Whitening matched filter	$\left\|\mathbf{p}^H\mathbf{M}_x^{-1}\mathbf{r}_L\right\|^2 \underset{H_0}{\overset{H_1}{>}} \gamma \times \text{CA - CFAR power estimate}$
ML estimate of the target return	$\alpha_{ML} = \dfrac{\mathbf{p}^H\mathbf{M}_x^{-1}\mathbf{r}_L}{\mathbf{p}^H\mathbf{M}_x^{-1}\mathbf{p}}$
GLRT-single cell	$\left\|\alpha_{ML}\right\|^2 \underset{H_0}{\overset{H_1}{>}} \gamma \dfrac{\mathbf{r}_L^H\mathbf{M}_x^{-1}\mathbf{r}_L}{\mathbf{p}^H\mathbf{M}_x^{-1}\mathbf{p}}$
GLRT-multiple cell	$\left\|\alpha_{ML}\right\|^2 \underset{H_0}{\overset{H_1}{>}} \gamma \dfrac{\sum_{i=1}^{M}\mathbf{r}_i^H\mathbf{M}_x^{-1}\mathbf{r}_i}{\mathbf{p}^H\mathbf{M}_x^{-1}\mathbf{p}}$

The first simulation shows the performance improvement over the single-cell detector obtained by using neighboring range cells. As the clutter is assumed to be fully-correlated, exploitation of multiple range cells yields a significant improvement. As it can be seen in Figure 6.1, detection probability increases apparently when *M=5* cells are used instead of a single range cell. The SCR gain is about 2 dB in this case. Increasing the number of secondary cells to *M=15* causes an additional 0.2dB.

The performance of the detector is significantly dependent on the speckle correlation coefficient. This effect is shown in Figure 6.2 for two different numbers of pulses used. Small number of pulses experiences more performance loss in low-correlated speckle condition. Detection performance versus Doppler frequency for different number of pulses is given in Figure 6.3. As expected, increasing the number of pulses increases the detection performance considerably and performance loss occurs at lower Doppler values, where the clutter is dominant and suppressed.

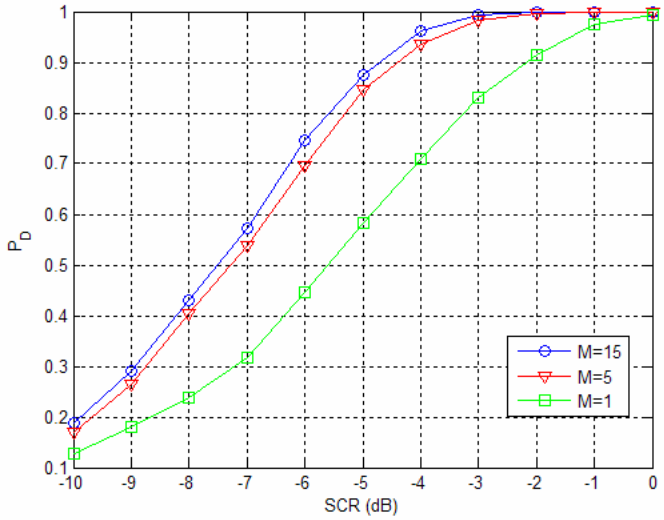

Figure 6.1 Detection performance versus SCR, various number of range cells

$P_{FA}=10^{-3}$, N = 5, MC = 2000, $\nu = 2$, $\mu = 5$, $\sigma^2 = 0$, $\rho_s = 0.8$, $\rho_T = 1$, $f_D/PRF = 0.5$

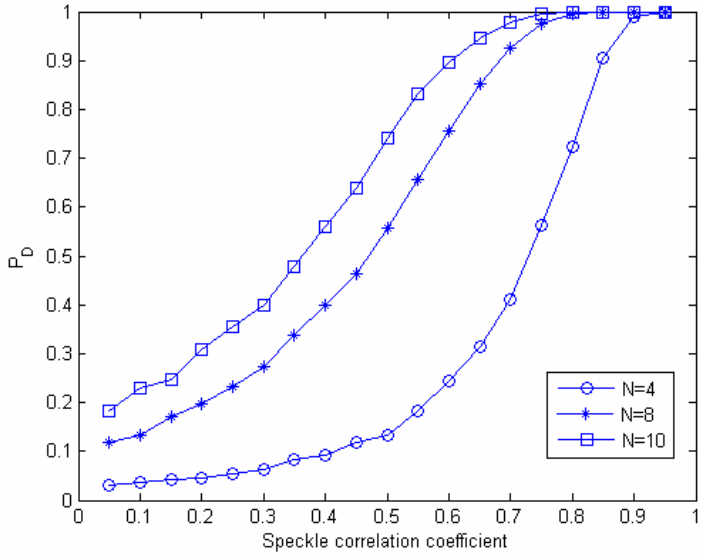

Figure 6.2 Detection performance versus speckle correlation coefficient, various number of pulses

$P_{FA}=10^{-3}$, M = 15, MC = 2000, $\nu = 2$, $\mu = 5$, $\sigma^2 = 0$, $\rho_T = 1$, SCR=-5dB, $f_D/PRF = 0.5$

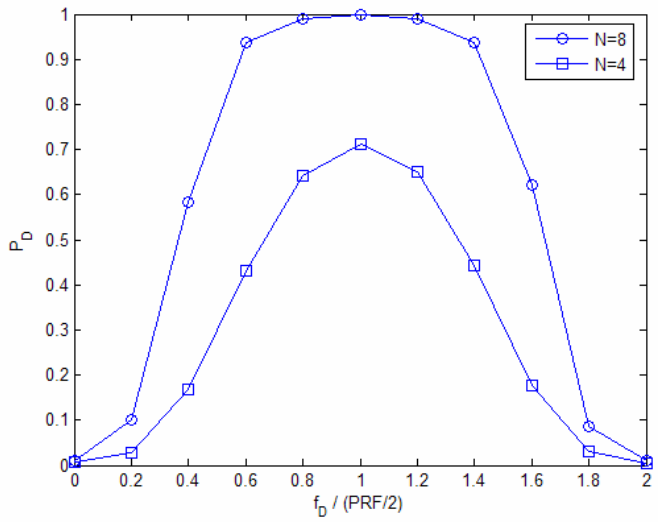

Figure 6.3 Detection performance versus Doppler frequency, various number of pulses

$P_{FA}=10^{-3}$, M = 15, MC = 2000, $\nu = 2$, $\mu = 5$, $\sigma^2 = 0$, $\rho_s = 0.8$, $\rho_T = 1$, SCR=-5dB

The remaining part of the simulations shows the performance for a Swerling 1 fluctuating target. Similar performance improvement with using the information in all of the range cells can be seen in this situation also (Figure 6.4). Some loss is observed here since the target fluctuates. For smaller number of pulses, the simulation is repeated to obtain Figure 6.5. Reducing the number of pulses from 8 to 4, a loss is incurred. Detection probability change with target Doppler frequency is shown in Figure 6.7. Due to the fact that the clutter signal is highly correlated and is a low-frequency signal, its suppression requires placing a notch at the low frequencies. This, in turn, causes a loss in detection probability at low Doppler frequencies.

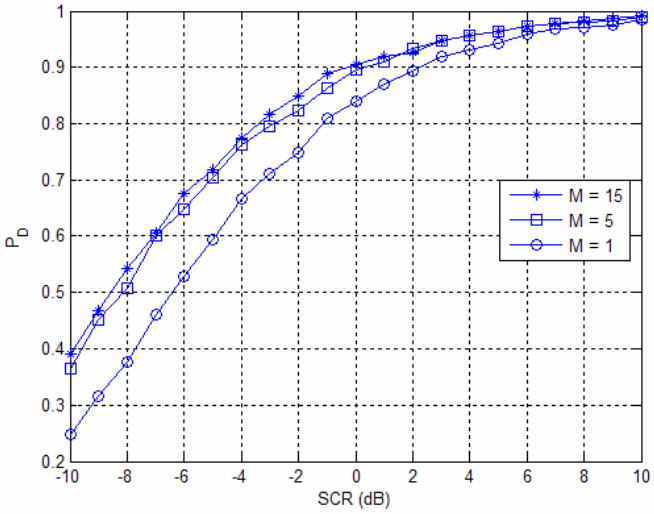

Figure 6.4 Detection performance versus SCR, various number of range cells, large number of pulses

$P_{FA}=10^{-3}$, N=8, ν=2, μ=5, ρ_s= 0.8, f_D=0.5 PRF, 10000 trials.

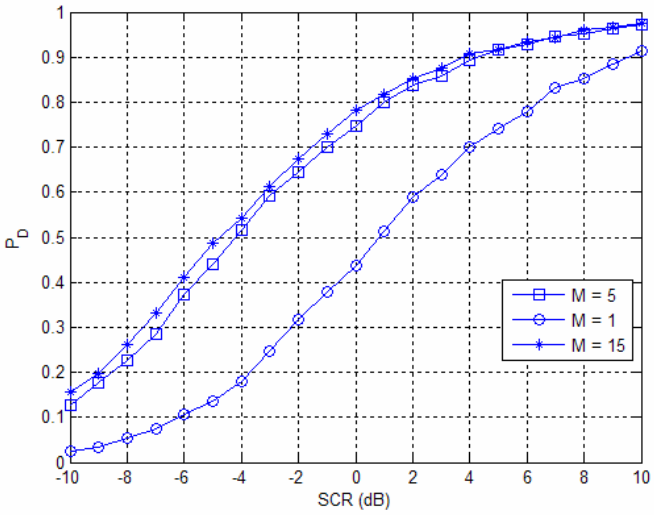

Figure 6.5 Detection performance, various number of range cells, small number of pulses

$P_{FA}=10^{-3}$, N=4, ν=2, μ=5, ρ_s= 0.8, f_D=0.5 PRF, 10000 trials.

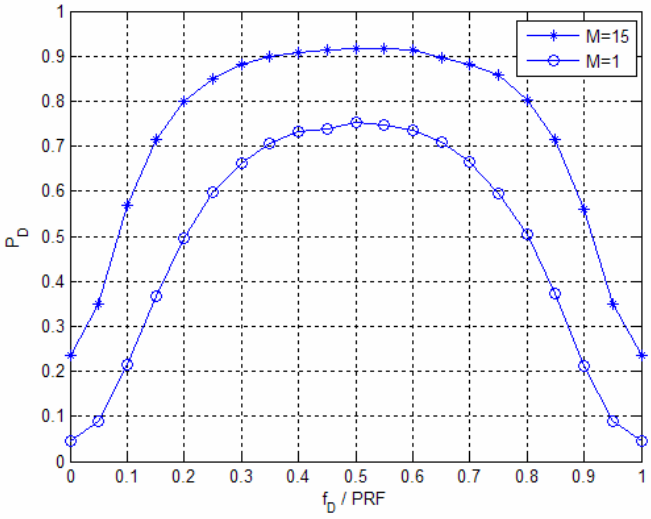

Figure 6.6 Detection performance versus Doppler frequency, various number of range cells

$P_{FA}=10^{-3}$, N=4, ν=2, μ=5, ρ_s=0.8, SCR=5dB, 10000 trials

Part of this work will be presented in [20].

6.1.3 Partial Spatial Correlation

When the spatial partial correlation coefficient of the texture component is known, this information can be used in the derivation of the detector, by means of using the estimation given in Section 5.3.4. However, this method is mathematically complex.

In this section, the performance of the detector derived for fully-correlated texture is analyzed when there is partial spatial correlation among neighboring range-cells.

Figure 6.7 shows the performance for various spatial correlation coefficients. As it can be seen, even if there is low correlation such as 0.4, it is advantageous to use the multiple range-cell detector when compared to the single-cell detector.

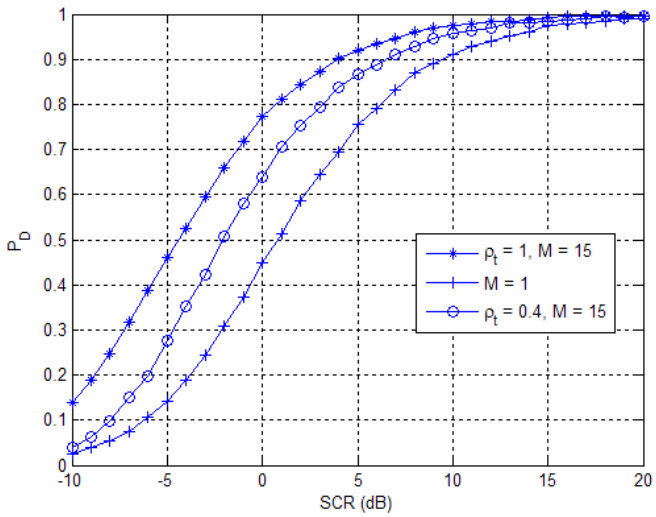

Figure 6.7 Detection performance versus SCR for various texture correlation coefficients

$P_{FA}=10^{-3}$, N=4, ν=2, μ=5, ρ_s= 0.8, f_D=0.5 PRF, 10000 trials.

Based on this result, which is quite important, it is recommended to use the information in the neighboring cells by means of the detector derived for fully-correlated texture, even though the correlation is low. This is an improvement over the approach of using the single cell detector in situations where the texture component differs among the range cells [14], [27].

6.1.4 GLRT-MAP Detector

When a-priori information on the texture parameter distribution is available, instead of the ML estimate, the MAP estimate could be used. This approach is called the suboptimum MAP detector in [26], since the optimal but complex detector (Equation (6.13)) is not used despite the knowledge of the parameter distribution. For the fully-correlated case, as derived in Section 5.3.3, under H_0, the MAP estimate is

$$\tau_{MAP,0} = \frac{\mu}{2\nu}(\nu - NM - 1) + \frac{1}{2\nu}\sqrt{\mu(\mu(NM+1-\nu)^2 + 4\nu\sum_{k=1}^{M}\mathbf{r_k}^H\mathbf{M}_x^{-1}\mathbf{r_k}}\ , \tag{6.36}$$

and under H_1, it is

$$\begin{aligned}\tau_{MAP,1} &= \frac{\mu}{2\nu}(\nu - NM - 1) \\ &+ \frac{1}{2\nu}\sqrt{\mu(\mu(NM+1-\nu)^2 + 4\nu(\sum_{\substack{k=1\\k\neq L}}^{M}\mathbf{r_k}^H\mathbf{M}_x^{-1}\mathbf{r_k} + (\mathbf{r}_L - \mathbf{s}_L)^H\mathbf{M}_x^{-1}(\mathbf{r}_L - \mathbf{s}_L))}\ .\end{aligned} \tag{6.37}$$

Substituting these estimates in the test given by Equation (6.10) and simplifying, the following expression is obtained:

$$MN\ln\frac{\tau_{MAP,0}}{\tau_{MAP,1}} - \frac{1}{\tau_{MAP,1}}[\sum_{i=1,i\neq L}^{M}\mathbf{r}_i^H\mathbf{M}_x^{-1}\mathbf{r}_i + (\mathbf{r}_L - \mathbf{s}_L)^H\mathbf{M}_x^{-1}(\mathbf{r}_L - \mathbf{s}_L)] + \frac{1}{\tau_{MAP,0}}\sum_{i=1}^{M}\mathbf{r}_i^H\mathbf{M}_x^{-1}\mathbf{r}_i\ . \tag{6.38}$$

The target return can be estimated using Equation (6.23) and hence $\boldsymbol{s_L}$ can be formed. The existence of the target is tested by comparison of the ratio given by Equation (6.38) with a proper threshold.

6.2 Detection in Multiple-Target Environment

One of the most important problems in target detection is the existence of interfering targets. In a work done by Rickard et al., it was stated that for low false alarm probabilities the maximum achievable detection probability may be less than 0.5, even if the main target has a higher SCR [48].

It is shown here that in uncorrelated texture component case, even if they have different Doppler values, if there are two targets at the same resolution cell, the single cell GLRT detector cannot perform satisfactorily and target masking occurs.

In this study, firstly, a detector for two targets is designed. For this purpose, multiple hypotheses for existence of one target, two targets and no target cases are considered. However, due to unequal probabilities and the difficulty in cost assignment, the Bayes detector was seen to be unsuitable.

For the purpose of simplicity, a single target signal is formed by addition of the two target signals. This refers to the existence of targets together. On the other hand, a target with zero amplitude corresponds to a single target case. The target returns are estimated in derivation of the detector.

The detector derived before is extended to two-target case as follows. Let the total target signal be

$$\mathbf{s} \overset{\Delta}{=} \alpha_1 \mathbf{p_1} + \alpha_2 \mathbf{p_2} \tag{6.39}$$

where, $\mathbf{p_1}$ and $\mathbf{p_2}$ are the Doppler steering vectors of the two targets.

If the targets are at different range cells, the method derived above can be used. However, if they are at the same range cell, the ML estimators for the complex returns (α's) are obtained by solution of the equations below:

$$\frac{\partial}{\partial \alpha_1} \ln p_{\mathbf{r}|\tau,H_1}(\mathbf{r}|\tau,\alpha_1,\alpha_2,H_1) = 0\,,\ \frac{\partial}{\partial \alpha_2} \ln p_{\mathbf{r}|\tau,H_1}(\mathbf{r}|\tau,\alpha_1,\alpha_2,H_1) = 0 \tag{6.40}$$

$$-\mathbf{p}_1{}^H \mathbf{M}_x{}^{-1} \mathbf{r}_K + \alpha_1\, \mathbf{p}_1{}^H \mathbf{M}_x{}^{-1} \mathbf{p}_1 + \alpha_2\, \mathbf{p}_1{}^H \mathbf{M}_x{}^{-1} \mathbf{p}_2 = 0\,, \tag{6.41}$$

$$-\mathbf{p}_2{}^H \mathbf{M}_x{}^{-1} \mathbf{r}_K + \alpha_1\, \mathbf{p}_2{}^H \mathbf{M}_x{}^{-1} \mathbf{p}_1 + \alpha_2\, \mathbf{p}_2{}^H \mathbf{M}_x{}^{-1} \mathbf{p}_2 = 0\,. \tag{6.42}$$

Solving these equations, the estimates are found to be

$$\alpha_{1,ML} = \frac{(\mathbf{p}_2{}^H \mathbf{M}_x{}^{-1}\mathbf{p}_2)(\mathbf{p}_1{}^H \mathbf{M}_x{}^{-1}\mathbf{r}_K) - (\mathbf{p}_1{}^H \mathbf{M}_x{}^{-1}\mathbf{p}_2)(\mathbf{p}_2{}^H \mathbf{M}_x{}^{-1}\mathbf{r}_K)}{(\mathbf{p}_1{}^H \mathbf{M}_x{}^{-1}\mathbf{p}_1)(\mathbf{p}_2{}^H \mathbf{M}_x{}^{-1}\mathbf{p}_2) - \left|\mathbf{p}_1{}^H \mathbf{M}_x{}^{-1}\mathbf{p}_2\right|^2}, \tag{6.43}$$

$$\alpha_{2,ML} = \frac{(\mathbf{p}_1{}^H \mathbf{M}_x{}^{-1}\mathbf{p}_1)(\mathbf{p}_2{}^H \mathbf{M}_x{}^{-1}\mathbf{r}_K) - (\mathbf{p}_2{}^H \mathbf{M}_x{}^{-1}\mathbf{p}_1)(\mathbf{p}_1{}^H \mathbf{M}_x{}^{-1}\mathbf{r}_K)}{(\mathbf{p}_1{}^H \mathbf{M}_x{}^{-1}\mathbf{p}_1)(\mathbf{p}_2{}^H \mathbf{M}_x{}^{-1}\mathbf{p}_2) - \left|\mathbf{p}_1{}^H \mathbf{M}_x{}^{-1}\mathbf{p}_2\right|^2}. \tag{6.44}$$

Writing in a different way, the following expressions are obtained:

Let,

$$\begin{aligned} b_1 &\stackrel{\Delta}{=} \mathbf{p}_1{}^H \mathbf{M}_x{}^{-1}\mathbf{p}_1, \quad b_2 \stackrel{\Delta}{=} \mathbf{p}_2{}^H \mathbf{M}_x{}^{-1}\mathbf{p}_2 \\ b_{12} &\stackrel{\Delta}{=} \mathbf{p}_1{}^H \mathbf{M}_x{}^{-1}\mathbf{p}_2, \quad a \stackrel{\Delta}{=} b_1 b_2 - \left|b_{12}\right|^2 \end{aligned} \tag{6.45}$$

and denoting the whitening matched filtered signals as

$$WMF_1 \stackrel{\Delta}{=} (\mathbf{p}_1{}^H \mathbf{M}_x{}^{-1}\mathbf{r}_K), \quad WMF_2 \stackrel{\Delta}{=} (\mathbf{p}_2{}^H \mathbf{M}_x{}^{-1}\mathbf{r}_K), \tag{6.46}$$

the following equations are obtained:

$$\begin{aligned} \alpha_{1,ML} &= \frac{b_2}{a} WMF_1 - \frac{b_{12}}{a} WMF_2 \\ \alpha_{2,ML} &= \frac{b_1}{a} WMF_2 - \frac{b_{12}^*}{a} WMF_1 \end{aligned} \tag{6.47}$$

The estimator for α_1 for the single target case was

$$\alpha_{1,s,ML} = \frac{WMF_1}{b_1}. \tag{6.48}$$

Hence, the detector for multiple targets is

$$\frac{\sum_{i=1}^{M} \mathbf{r}_i{}^H \mathbf{M}_x{}^{-1} \mathbf{r}_i}{\sum_{i=1,i\neq L}^{M} \mathbf{r}_i{}^H \mathbf{M}_x{}^{-1} \mathbf{r}_i + (\mathbf{r}_L - \alpha_{\mathbf{1},ML}\,\mathbf{p_1} - \alpha_{\mathbf{2},ML}\,\mathbf{p_2})^H \mathbf{M}_x{}^{-1} (\mathbf{r}_L - \alpha_{\mathbf{1},ML}\,\mathbf{p_1} - \alpha_{\mathbf{2},ML}\,\mathbf{p_2})} \underset{H_0}{\overset{H_1}{\gtrless}} \gamma. \tag{6.49}$$

However, this approach has a drawback: Detection of multiple targets tests the existence of targets at Doppler frequencies $\mathbf{p_1}$ and/or $\mathbf{p_2}$. Nevertheless, in detection case, it is not straightforward to extract the information on the powers of the targets. So, a better approach is to handle each range-Doppler cell separately and consider it as the cell under test while considering the existence probability of other interfering targets in neighboring cells. In this case, it is assumed that there exist targets at each range and Doppler frequency. At cells, where there is no target, the signal can be viewed as a return from a target with zero RCS.

Let the signal at range *i*, consisting of returns from *N* Doppler frequencies be modeled as

$$s_i = \sum_{l=1}^{N} \alpha_{il}\ \mathbf{p_1} \tag{6.50}$$

Carrying out similar operations, for range *L*, the detector for the exactly-known-signal case is derived to be

$$2\gamma \mathrm{Re}\{\mathbf{s_L^H M_s^{-1} r_L}\} \underset{<}{\overset{>}{}} (\gamma-1) \sum_{\substack{i=1 \\ i\neq L}}^{M} (\mathbf{r_i} - \mathbf{s_i})^H \mathbf{M_s^{-1}} (\mathbf{r_i} - \mathbf{s_i}) + \gamma \mathbf{s_L^H M_s^{-1} s_L} + (\gamma-1) \mathbf{r_L^H M_s^{-1} r_L}. \tag{6.51}$$

If the test succeeds, it is concluded that there is a target at the L^{th} range cell. The effect of interfering targets, if there exists any, is estimated and suppressed by the detector.

For unknown target returns, the ML estimates for target returns are obtained as follows. Here it is assumed that the Doppler value is known.

Taking the derivative of the likelihood function with respect to α_{ix} and equating to zero, the following is obtained:

$$\mathbf{r_i^H M_s^{-1} p_x} = \sum_{l=1}^{N} \alpha_{il}^{*}\, \mathbf{p_l^H M_s^{-1} p}_x \tag{6.52}$$

Performing the same operations for the other Doppler frequencies and the range cells, $N \times M$ unknowns and $N \times M$ equations are obtained. The equations can be written in matrix form as given below:

$$\underbrace{\begin{bmatrix} p_{11} & p_{12} & \cdots & p_{1N} \\ p_{21} & p_{22} & \cdots & p_{2N} \\ \vdots & & \cdots & \vdots \\ p_{N1} & p_{N2} & \cdots & p_{NN} \end{bmatrix}}_{\substack{\mathbf{P} \\ N\times N}} \underbrace{\begin{bmatrix} \alpha_{11} & \alpha_{21} & \cdots & \alpha_{M1} \\ \alpha_{12} & \alpha_{22} & \cdots & \alpha_{M2} \\ \vdots & & \cdots & \vdots \\ \alpha_{1N} & \alpha_{2N} & \cdots & \alpha_{MN} \end{bmatrix}}_{\substack{\mathbf{A} \\ N\times M}} = \underbrace{\begin{bmatrix} p_1^H M_s^{-1} r_1 & \cdots & \cdots & p_1^H M_s^{-1} r_M \\ \vdots & & \cdots & \vdots \\ \vdots & & \cdots & \vdots \\ p_N^H M_s^{-1} r_1 & \cdots & \cdots & p_N^H M_s^{-1} r_M \end{bmatrix}}_{\substack{\mathbf{D} \\ N\times M}},$$

where $p_{xy} \overset{\Delta}{=} \mathbf{p}_x^{\mathbf{H}} \mathbf{M}_x^{-1} \mathbf{p}_y$.

Shortly, the estimates of the target returns are obtained using the following equation:

$$\mathbf{A} = \mathbf{P}^{-1}\, \mathbf{D} \tag{6.53}$$

If any range or Doppler cells are excluded, then these matrices can be scaled to exclude those cells. For example, if no interfering target is expected at some of the

range or Doppler cells, those cells can be excluded while forming the matrices **A**, **P** and **D**.

In what follows, some performance results will be presented. In the simulations, number of Monte Carlo points is 10^5. Texture Gamma-distribution parameters are ν=2 and μ=2. Noise power is 1 and speckle correlation coefficient is *0.8*. *PRF* is set to 2.

Detection probabilities of the detectors for 1 and 2 target cases are given in Table 6.2. F_{d1} and F_{d2} denote the Doppler frequencies. M and N are the number of range cells and pulses respectively. The first detector is the one derived in this part. The second one is the multiple-range cell-multiple-pulse detector that was derived in Section 6.1. The third one shown in the last column is the GLRT detector that uses a single range cell [14]. The SCR=-∝, values are investigated in order to exhibit the false alarm rate performance. The false alarm probability is obtained as 10^{-3}, which the desired value. It is apparent that using the single cell detector, the target can not be detected and is completely masked in multiple-target cases. Using the multiple range cells also yields high performance improvement. In multiple-range-cell detector, the loss is not as much as the one caused by the single cell detector, as the free range cells give additional information to the detector. When there is no available neighboring cell (M=1), the multiple-range-cell, single target detector is identical to the single cell detector and it can not detect the multiple targets, either. When there is only a single target, the multiple target detector experiences a loss at low SCR cases and especially when there is single range cell.

Table 6.2 Detection probabilities of the detectors for single and two target cases (F_{d1}=1, F_{d2}=0.6, N=8)

SCR1	*SCR2*	*M*	*GLRT-multiple target @p1 and/or p2*	*GLRT-single target, multiple cell @p1*	*GLRT-single cell @p1*
-∝	-∝	10	$1x10^{-3}$	$1x10^{-3}$	$1x10^{-3}$
7	7	10	0.99	0.98	0.01
7	-∝	10	0.97	0.98	0.94
5	5	10	0.98	0.96	0.01
5	-∝	10	0.95	0.96	0.88
3	3	10	0.96	0.91	0.01
3	-∝	10	0.89	0.90	0.74
1	-∝	10	0.76	0.79	0.53
-∝	-∝	1	$1x10^{-3}$	$1x10^{-3}$	$1x10^{-3}$
15	15	1	0.99	0.00	0.00
15	-∝	1	0.99	0.99	0.99
10	-∝	1	0.97	0.98	0.98
5	-∝	1	0.80	0.88	0.88
3	-∝	1	0.61	0.74	0.74
1	-∝	1	0.37	0.53	0.53

In conclusion, GLRT that uses a single cell, experiences drastic performance degradation in the multiple target scenario and cannot detect any of the targets. When multiple range cells are used, since the neighboring cells can be used in estimation of the texture parameter, performance loss is not so severe. However, the best detection performance is obtained with the multiple-target detector. This detector detects the targets at Doppler frequencies corresponding to $\mathbf{p_1}$ and/or $\mathbf{p_2}$.

Once the targets are detected, the ML estimators of the returns at $\mathbf{p_1}$ and $\mathbf{p_2}$ can be used in estimation of the power of the target return. Following this, an appropriate threshold can be set to make detection at the two Doppler values separately.

A better approach is to test the existence of a target in the cell under test, while considering the targets at the neighboring cells as interference. For this purpose, a

GLRT is derived. Here, the most problematic case, where the texture components of different range cells are independent, is considered.

Let the Doppler cell under test be $\mathbf{p_m}$ and let an interfering target exists at Doppler $\mathbf{p_i}$.(i=1,2,…, N)**.** The main target return α_m and the interfering target return α_i are assumed to be unknown. Let the hypothesis (H_0) show the case where there is an interfering target and hypothesis (H_1) denote the case where there main and interfering targets exist together:

$$H_0: \quad \mathbf{r} = \sqrt{\tau}\,\mathbf{x} + \alpha_i\,\mathbf{p}_i \quad , \tag{6.54}$$

$$H_1: \quad \mathbf{r} = \sqrt{\tau}\,\mathbf{x} + \alpha_m\,\mathbf{p}_m + \alpha_i\,\mathbf{p}_i \quad . \tag{6.55}$$

The GLRT is

$$\Lambda_g(\mathbf{r}) = \frac{\max\limits_{\tau,\alpha_m,\alpha_i,i} p_{\mathbf{r}|\tau,H_1}(\mathbf{r}|\tau,\alpha_m,\mathbf{p}_m,\alpha_i,\mathbf{p}_i,H_1)}{\max\limits_{\tau,\alpha_i,i} p_{\mathbf{r}|\tau,H_0}(\mathbf{r}|\tau,\alpha_i,\mathbf{p}_i,H_0)} \underset{H_0}{\overset{H_1}{\gtrless}} \gamma\,. \tag{6.56}$$

The log-likelihood functions are

$$\begin{aligned}\ln p_{\mathbf{r}|\tau,H_0}(\mathbf{r}|\tau,\alpha_i,\mathbf{p}_i,H_0) &= -N\ln\pi - \ln|\mathbf{M}_r| - (\mathbf{r}-\alpha_i\,\mathbf{p}_i)^H\mathbf{M}_r^{-1}(\mathbf{r}-\alpha_i\,\mathbf{p}_i)\\ &= -N\ln\pi - N\sum_{i=1}^{M}\ln\tau_i - |\mathbf{M}_\mathbf{x}| \\ &\quad -\frac{1}{\tau}(\mathbf{r}-\alpha_i\,\mathbf{p}_i)^H\mathbf{M}_\mathbf{x}^{-1}(\mathbf{r}-\alpha_i\,\mathbf{p}_i) \quad .\end{aligned} \tag{6.57}$$

$$\begin{aligned}\ln p_{\mathbf{r}|\tau,H_1}(\mathbf{r}|\tau,\alpha_m,\mathbf{p}_m,\alpha_i,\mathbf{p}_i,H_1) &= -N\ln\pi - \ln|\mathbf{M}_r| \\ &\quad -(\mathbf{r}-\alpha_m\,\mathbf{p}_m-\alpha_i\,\mathbf{p}_i)^H\mathbf{M}_r^{-1}(\mathbf{r}-\alpha_m\,\mathbf{p}_m-\alpha_i\,\mathbf{p}_i)\\ &= -N\ln\pi - N\sum_{i=1}^{M}\ln\tau_i - |\mathbf{M}_\mathbf{x}| \\ &\quad -\frac{1}{\tau}(\mathbf{r}-\alpha_m\,\mathbf{p}_m-\alpha_i\,\mathbf{p}_i)^H\mathbf{M}_\mathbf{x}^{-1}(\mathbf{r}-\alpha_m\,\mathbf{p}_m-\alpha_i\,\mathbf{p}_i)\end{aligned} \tag{6.58}$$

The texture estimates for the two hypotheses, $\tau_{ML,0}$ and $\tau_{ML,1}$, are found, by taking the partial derivative of the likelihood function with respect to the texture parameter and equating to zero, as

$$\tau_{ML,0} = \frac{(\mathbf{r} - \alpha_i \mathbf{p}_i)^H \mathbf{M}_x^{-1} (\mathbf{r} - \alpha_i \mathbf{p}_i)}{N}, \tag{6.59}$$

$$\tau_{ML,1} = \frac{(\mathbf{r} - \alpha_m \mathbf{p}_m - \alpha_i \mathbf{p}_i)^H \mathbf{M}_x^{-1} (\mathbf{r} - \alpha_m \mathbf{p}_m - \alpha_i \mathbf{p}_i)}{N}. \tag{6.60}$$

The interfering target return estimate for the H_0 hypothesis is

$$\alpha_{i,ML,0} = \frac{\mathbf{p}_i^H \mathbf{M}_x^{-1} \mathbf{r}}{\mathbf{p}_i^H \mathbf{M}_x^{-1} \mathbf{p}_i}. \tag{6.61}$$

As given in Equation (6.53), the main and interfering target return estimates $\alpha_{m,ML,1}$ and $\alpha_{i,ML,1}$ for the H_1 hypothesis are found using

$$\begin{bmatrix} \alpha_{m,ML,1} \\ \alpha_{i,ML,1} \end{bmatrix} = \begin{bmatrix} 1 & p_{12}/p_{11} \\ p_{21}/p_{22} & 1 \end{bmatrix}^{-1} \begin{bmatrix} \alpha_{m,s} \\ \alpha_{i,s} \end{bmatrix}, \tag{6.62}$$

where

$$\alpha_{m,s} = \frac{\mathbf{p}_m^H \mathbf{M}_x^{-1} \mathbf{r}}{\mathbf{p}_m^H \mathbf{M}_x^{-1} \mathbf{p}_m} \text{ and } \alpha_{i,s} = \frac{\mathbf{p}_i^H \mathbf{M}_x^{-1} \mathbf{r}}{\mathbf{p}_i^H \mathbf{M}_x^{-1} \mathbf{p}_i}. \tag{6.63}$$

This estimation is performed for each of the probable interfering Doppler values $\mathbf{p_i}$, i=1, …, N, except for the main Doppler bin under test.

Next, the Doppler bin of the interfering target, under H_0 and H_1 hypotheses, k_0 and k_1, are estimated. For this purpose, the likelihood function under H_0 is maximized over the Doppler values:

$$k_0 = \arg\min_i \quad (\mathbf{r} - \alpha_i \mathbf{p}_i)^H \mathbf{M}_x^{-1} (\mathbf{r} - \alpha_i \mathbf{p}_i), \tag{6.64}$$

$$k_1 = \arg\min_i \quad (\mathbf{r} - \alpha_{m,ML,1} \mathbf{p}_m - \alpha_i \mathbf{p}_i)^H \mathbf{M}_x^{-1} (\mathbf{r} - \alpha_{m,ML,1} \mathbf{p}_m - \alpha_i \mathbf{p}_i). \tag{6.65}$$

Hence the GLRT becomes

$$\frac{(\mathbf{r} - \alpha_{i,ML,0}(k_0)\mathbf{p}_{i_0})^H \mathbf{M}_x^{-1} (\mathbf{r} - \alpha_{i,ML,0}(k_0)\mathbf{p}_{i_0})}{(\mathbf{r} - \alpha_{m,ML,1}\mathbf{p}_m - \alpha_{i,ML,1}(k_1)\mathbf{p}_{i_1})^H \mathbf{M}_x^{-1} (\mathbf{r} - \alpha_{m,ML,1}\mathbf{p}_m - \alpha_{i,ML,1}(k_1)\mathbf{p}_{i_1})} \underset{H_0}{\overset{H_1}{\gtrless}} \gamma, \tag{6.66}$$

where $\alpha_{i,ML,j}(q)$ denotes the estimate of the interfering target return, under hypothesis H_j and taking its Doppler as q, when finding the estimate in Equation (6.62).

Next, a performance analysis result is presented. In this simulation, the interfering signal-to-clutter power ratio is 15dB; the clutter texture distribution order parameter is 2, which corresponds to a spiky situation. Additive white Gaussian noise is simulated with an interfering signal-to-noise ratio of 20dB. The main and interfering targets are located at the 5th and 7th Doppler bins, where there are a total of 10 Doppler bins (pulses). The detection probabilities of the double-target GLRT derived above and the classical single target detector are shown in Table 6.3.

Table 6.3 Detection probabilities of the double-target GLRT and single target GLRT

Main /interfering target power ratio	P_D of double-target detector	P_D of single-target detector
0.1	0.93	0.11
0.5	0.99	0.55
1	0.99	0.76
2	0.99	0.89

As it can be seen, the double-target detector has excellent performance in detecting the target, where the single target detector misses the main target when the interfering target has high power. It was verified that the algorithm detects the Doppler of the interfering target successfully.

This work can be extended to cover number of interfering targets greater than two.

CHAPTER 7

CONCLUSIONS

In this thesis, radar detection of targets against correlated, non-Gaussian and heterogeneous clutter was studied. The designed detectors may be grouped as noncoherent and coherent detection methods.

Three non-coherent techniques, Goodness-of-Fit (GoF), Expectation-Maximization (EM) and Clutter-map (CM) CFAR were designed and analyzed:

The GoF-CFAR technique firstly determines the range-heterogeneity of the clutter samples using a goodness of fit test, which is an original approach. It was shown that the performance of the test in determination of heterogeneity is excellent. After determination of the heterogeneity, the transition point and the distribution parameters are estimated and the threshold is set accordingly. The method was shown to alleviate the masking and false alarm problems near the clutter edge.

The EM-CFAR method uses the Expectation-Maximization algorithm in identifying the differing regions and estimating their distribution parameters. Using this information, the algorithm determines the threshold to yield the desired false alarm probability.

GoF and EM-CFAR algorithms are novel in that they consider the range-heterogeneity and non-Gaussian character of the clutter at the same time. The

algorithms were shown to perform significantly better when compared to the classical methods designed for homogeneous non-Gaussian clutter, which have false alarms or target masking problems near the clutter edge; and the ones designed for range-heterogeneous Rayleigh clutter, which yield excessive false alarms in spiky clutter.

The CM-CFAR, developed in this work, does not suffer from any type of heterogeneity in range, since it uses a map that stores the clutter information of each range cell. In many of the works, the shape parameter of the clutter is assumed to be known and these algorithms suffer from performance loss when the designed parameter differs from the actual one. In this study, both of the parameters are estimated and updated in the clutter map, which is believed to be novel. The algorithm is computationally efficient and performs well even in severe clutter condition.

In order to exploit all the information in range cells and coherent pulses, coherent detectors were designed: Since the detector structure is dependent on the clutter parameters, they were estimated, using both the Maximum Likelihood (ML) and Maximum-a-Posteriori (MAP) estimation techniques. Uncorrelated, partially-correlated and fully-correlated texture cases were investigated and it was shown that the texture estimators perform very well in all of the clutter conditions. As expected, the estimation performance is higher with the MAP estimator, when the assumed texture distribution matches the actual one. On the other hand, the ML estimator is general and it can be used in cases whenever no assumption on the clutter amplitude distribution can be done.

Besides being used in design of the coherent detectors, the texture parameter estimators that were derived in this work can be used in other applications such as classification and segmentation on radar images.

Using the estimates of the texture parameter and the target return, GLRT detectors were designed. In design of the detectors, the correlation structure of the speckle component was assumed to be known. It was shown that these detectors have significant improvements over the well known detectors, which do not use all the range cells, in fully and partially-correlated texture situations. The detectors become equivalent to the well-known single-cell detectors when the texture components are uncorrelated.

It was shown that the detector that operates on a single range has significant performance degradation in the existence of an interfering target. The reason for this is that the only information used in estimation of the clutter is obtained from the range cell under consideration, which is corrupted by an interfering target. Hence, a detector was proposed to avoid the interfering target problem in the single-range cell detector. Also, another method was proposed to succeed the single-target detector to make it operate in multiple-target case, which is believed to be novel. It was shown that the method performs excellent in detection of the targets and thus alleviates the masking problem.

Future works can be stated as follows: Firstly, the analytical derivation for the detection and the false alarm probabilities of the coherent detectors can be performed. Then, the derivations can be extended to cover various clutter distributions and correlation structures. In addition, the multiple target study can be extended to cover the effects of pulse compression range sidelobes on other targets. Because, an important difficulty in design of the detectors is the mathematical tractability, special emphasis should be given on effective modeling of various clutter types and simplifications of the detectors to obtain suboptimum but acceptable solutions.

REFERENCES

[1] Anastassopoulos, V., and Lampropoulos, G.A., "Optimal CFAR detection in Weibull clutter," *IEEE Transactions on Aerospace and Electronic Systems*, vol. 31, no. 1, pp. 52-64, January 1995.

[2] Anastassopoulos, V., Lampropoulos, G.A., Drosopoulos, A., and Rey, M., "High Resolution Radar Clutter Statistics," *IEEE Transactions on Aerospace and Electronic Systems*, vol. 35, no.1, pp. 43-60, January 1999.

[3] Anderson, T.W. and Darling D.A., "A test of goodness of fit," *J.Am.Stat.Assoc*., vol. 49, pp. 765-769, 1954.

[4] Armstrong, B.C., and Griffiths, H.D., "Modelling Spatially Correlated K-Distributed Clutter," *Electronics. Letters,* vol. 27, no. 15, pp. 1355-1356, July 1991.

[5] Billingsley, J.B., Farina A., Gini F, Greco M.V., and Verrazzani L., "Statistical Analyses of Measured Radar Clutter Data," *IEEE Transactions on Aerospace and Electronic Systems,* vol. 35, no. 2, pp. 579-593, April 1999.

[6] Billingsley, J.B., *Low Angle Radar Land Clutter – Measurements and Empirical Models*. Scitech Publishing, NY, 2002.

[7] Blacknell, D., "Comparison of parameter estimators for K-distribution," *IEE Proceedings – Radar, Sonar Navigation,* vol. 141, no. 1, pp. 45-52, February 1994.

[8] Bucciarelli, T., Lombardo, P., and Tamburrini, S., "Optimum CFAR detection against compound Gaussian clutter with partially correlated texture," *IEE Proc.-Radar, Sonar Navigation.,* vol. 143, no. 2, pp. 95-104, April 1996.

[9] Chen, B, Varshney, P.K. and Michels, J.H., "Adaptive CFAR Detection for Clutter-Edge Heterogeneity Using Bayesian Inference," *IEEE Transactions on Aerospace and Electronic Systems,* vol. 39, no. 4, pp. 1462-1470, October 2003.

[10] Chung, P.J., Roberts, W.J.J., and Böhme, J.F., "Recursive K-Distribution Parameter Estimation," *IEEE Transactions on Signal Processing,* vol. 53, no. 2, pp. 397-402, February 2005.

[11] Christofferson, R.D., and Gillette, D.A., "A Simple Estimator of the Shape Factor of the Two-Parameter Weibull Distribution," *Journal of Climate and Applied Meteorology*, vol. 26, no. 2, pp. 323-325, February 1987.

[12] Conte, E., and Longo M., "Characterisation of radar clutter as a spherically invariant random process," *IEE Proc. F.,* no. 2, vol. 134, pp. 191-197, April 1987.

[13] Conte, E., Longo, M., and Lops, M., "Modeling and simulation of non-Rayleigh radar clutter," *IEE Proceedings-F*, vol. 138, no. 2, pp. 121-130, April 1991.

[14] Conte, E., Lops, M., and Ricci, G., "Asymptotically optimum radar detection in compound-Gaussian clutter," *IEEE Transactions on Aerospace and Electronic Systems*, vol. 31, no. 2, pp. 617-625, April 1995.

[15] Conte, E, De Maio, A, and Galdi, C, "Statistical Analysis of Real Clutter at Different Range Resolutions," *IEEE Transactions on Aerospace and Electronic Systems,* vol. 40, no. 3, pp. 903-918, July 2004.

[16] Doyuran, Ü, and Tanık, Y., "Radar belirsizlik ve kör bölge çözümünde değişken darbe aralığı," *Proceedings of the ITUSEM 2005*, pp. 219-222, Adana, Turkey, November 2005.

[17] Doyuran, Ü, and Tanık, Y., "Weibull kargaşa haritalı radar hedef tespiti," *Proceedings of the URSI-Türkiye 2006*, pp. 601-603, Ankara, Turkey, September 2006.

[18] Doyuran, U, and Tanik, Y., "Detection in range-heterogeneous Weibull clutter," *Proceedings of the IEEE Radar Conference-2007*, pp. 343-347, Waltham, MA, USA, April 2007.

[19] Doyuran, Ü, and Tanık, Y., "Değişken kargaşa altında radar hedef tespiti," *Proceedings of the SİU Conference 2007*, Eskişehir, Turkey, June 2007.

[20] Doyuran U, and Tanik Y., "Multi-Range and Multi-Pulse Radar detection in correlated non-Gaussian clutter," *Proceedings of the European Radar Conference*, Munich, Germany, October 2007 (to be published).

[21] Edde, B., *Radar: Principles, Technology, Applications*, Prentice-Hall, NJ, 1995.

[22] Evans, J.W., Johnson, R.A. and Green, D.W., "Two and Three-Parameter Weibull Goodness-of-Fit Tests," *United States Department of Agriculture, Forest Products Laboratory, Research Paper FPL-RP-493.*

[23] Farina, A and Studer, F.A., "A Review of CFAR Detection Techniques in Radar Systems," *Microwave Journal,* vol. 29, pp. 115-128, September 1986.

[24] Farina A., Gini F., Greco M.V., and Verrazzani L., "High resolution sea clutter data: Statistical analysis of recorded live data," *IEE Proceedings F.*, vol. 144, no. 3, pp. 121-130, June. 1997.

[25] Finn, H.M. "A CFAR Design for a Window Spanning Two Clutter Fields," *IEEE Transactions on Aerospace and Electronic Systems*, vol. 22, no. 2, pp. 155-169, March 1986.

[26] Gini, F. "Sub-optimum coherent radar detection in a mixture of K-distributed and Gaussian clutter," *IEE Proceedings-.F,* vol. 144, no. 1, pp. 39-48, February 1997.

[27] Gini, F., Greco, M.V. and Farina, A., "Clairvoyant and adaptive signal detection in non-Gaussian clutter: A data dependent threshold interpretation," *IEEE Transactions on Signal Processing*, vol. 47, no. 6, pp. 1522-1531, June 1999.

[28] Gini, F., and Farina, A., "Vector subspace detection in compound-Gaussian clutter. Part 1: Survey and new results," *IEEE Transactions on Aerospace and Electronic Systems*, vol. 38, no. 4, pp. 1295-1311, October 2002.

[29] Goldstein, G.B., "False-alarm regulation in log-normal and Weibull clutter," *IEEE Transactions on Aerospace and Electronic Systems*, vol. AES-9, no. 1, pp. 84-92, January 1973.

[30] How, J., and Leung, H., "No evidence of stable distributions in radar clutter," *Higher-Order Statistics, 1997. Proceedings of the IEEE Signal Processing Workshop on*, pp. 264-267, Banff, Alta, July 1997.

[31] Iskander, D.R., Zoubir, A.M. and Boashash, B., "A method for estimating the parameters of the K-distribution," *IEEE Transactions on Signal Processing*, vol. 47, no. 4, pp.1147-1151, April 1999.

[32] Iskander, D.R., and Zoubir A.M., "Estimation of the parameters of the K-distribution using higher order and fractional moments," *IEEE Transactions on Aerospace and Electronic Systems*, vol. 35, no. 4, pp. 1453-1457, October. 1999.

[33] Kay, S.M., *Fundamentals of Statistical Signal Processing: Estimation Theory*. Prentice-Hall, NJ, 1993.

[34] Kelly, E.J., "An Adaptive Detection Algorithm," *IEEE Transactions on Aerospace and Electronic Systems*, vol. 22, no. 1, pp. 115-127, March 1986.

[35] Levanon, N., and Shor, M, "Order statistics CFAR for Weibull background," *IEE Proceedings*, vol. 137, no. 3, pp. 157-162, June 1990.

[36] Lombardo, P., and Farina, A., "Coherent Radar Detection against K-distributed clutter with partially correlated texture," *Elsevier Signal Processing,* vol. 48, no. 1, pp. 1-15, January 1996.

[37] Long, M.W, *Radar Reflectivity of Land and Sea*, 3rd edition, Artech House, Dedham, MA, USA, 2001.

[38] Lops, M., "Hybrid clutter-map/L-CFAR procedure for clutter rejection in nonhomogenous environment," *IEE Proceedings-Radar, Sonar Navigation*, vol. 143, no. 4, pp. 239-245, August 1996.

[39] Moon, T.K., and Stirling, W.C., *Mathematical Methods and Algorithms for Signal Processing*, Prentice-Hall, NJ, 2000.

[40] Nikias, C., and Shao, M., *Signal Processing with Alpha-Stable Distributions and Applications*, John Wiley, NY, 1995.

[41] Posner, F.L., "Spiky sea clutter at high range resolutions and very low grazing angles," *IEEE Transactions on Aerospace and Electronic Systems*, vol. 38, no. 1, pp. 58-73, January 2002.

[42] Pulsone, N.B., and Raghavan, R.S., "Analysis of an adaptive CFAR detector in non-Gaussian interference," *IEEE Transactions on Aerospace and Electronic Systems*, vol. 35, no. 3, pp. 903-915, July 1999.

[43] Raemer, H.R. *Radar Systems Principles*, CRC Press, USA, 1997.

[44] Raghavan, R.S., "A method for estimating parameters of K-distributed clutter," *IEEE Transactions on Aerospace and Electronic Systems*, vol. 27, no. 2, pp. 238-246, March 1991.

[45] Rangaswamy, M., Weiner, D., and Öztürk, A., "Non-Gaussian random vector identification using spherically invariant random processes," *IEEE Transactions on Aerospace and Electronic Systems*, vol. 29, no. 1, pp. 111-124, January 1993.

[46] Ravid, R., and Levanon, N., "Maximum-likelihood CFAR for Weibull background," *IEE Proceedings-F,* vol. 139, no. 3, June 1992.

[47] Richards, M.A., *Fundamentals of Radar Signal Processing*, McGraw-Hill, NY, 2005.

[48] Rickard, J:T: and Dillard, G.M:, "Adaptive detection algorithms for multiple-target situations," *IEEE Transactions on Aerospace and Electronic Systems*, vol. 13, no. 4, pp. 338-343, July 1977.

[49] Robey, F.C., Fuhrman, D.R., Kelly, E.J., and Nitzberg, R., "A CFAR adaptive matched filter detector," *IEEE Transactions on Aerospace and Electronic Systems*, vol. 28, no. 1, pp. 208-216, January 1992.

[50] Rohling, H., "Radar CFAR thresholding in clutter and multiple target situations," *IEEE Transactions on Aerospace and Electronic Systems*, AES-19, no. 4, pp. 608-621, July 1983.

[51] Sangston, K.J., and Gerlach, K.B., "Coherent detection of Radar targets in a non-Gaussian background," *IEEE Transactions on Aerospace and Electronic Systems*, vol. 30, no. 2, pp. 330-340, April 1994.

[52] Sangston, K.J., Gini, F., Greco, M.V., and Farina, A., "Structures for Radar detection in compound Gaussian clutter," *IEEE Transactions on Aerospace and Electronic Systems*, vol. 35, no. 2, pp. 445-457, April 1999.

[53] Sekine, M., and Mao, Y., *Weibull Radar Clutter*, Peter Peregrinus, London, 1990.

[54] Skolnik, M.I., *Introduction to Radar Systems*, 3rd ed. McGraw-Hill, NY, 2001.

[55] Smith, M.E., and Varshney, P.K., "Intelligent CFAR processor based on data variability," *IEEE Transactions on Aerospace and Electronic Systems*, vol. 36, no. 3, pp. 837-847, July 2000.

[56] Stimson, G.W., *Introduction to Airborne Radar*, 2nd ed., SciTech Publishing, NJ, 1998.

[57] Streit, R.L., and Willett, P.K., "Detection of Random Transient Signals via Hyperparameter Estimation", *IEEE Transactions on Signal Processing*, vol. 47, no. 7, pp. 1823-1834, July 1999.

[58] Titterington D.M., Smith A.F.M. and Makov U.E., *Statistical Analysis of Finite Mixture Distributions*, John Wiley and Sons, NY, 1985.

[59] Van Trees, H.L., *Detection, Estimation, and Modulation Theory*, John Wiley and Sons, NY, 1968.

[60] Ward, K.D., "Compound representation of high resolution sea clutter," *Electronics Letters.,* vol. 17, no. 16, pp. 561-563, August 1981.

[61] Ward, K.D., Baker, C., and Watts, S., "Maritime surveillance radar. Part 1: Radar scattering from the ocean surface," *IEE Proceedings-F*, vol. 137, no. 2, pp. 51-62, April 1990.

[62] Ward, K.D., Watts S., and Tough R.J.A., *Sea Clutter: Scattering, the K distribution and Radar Performance*, SciTech Publishing, 2006.

[63] Weber, P. and Haykin, S., "Ordered Statistic CFAR Processing for Two-Parameter Distributions with Variable Skewness," *IEEE Transactions on Aerospace and Electronic Systems,* vol. 21, no. 6, pp. 819-821, November 1985.

[64] Wright, J.W, "A new model for sea clutter," *IEEE Transactions on Antennas and Propagation.,* vol. AP-16, no. 2, pp. 217-223, March 1968.

[65] Zenbil E.A., *Estimation Techniques for a Class of Non-Regular Distributions: The Weibull Case*, PhD Dissertation, Department of Statistics, METU, March 1991.

CURRICULUM VITAE

PERSONAL INFORMATION

Surname, Name	: Doyuran, Ülkü
Nationality	: Turkish (TC)
Date and Place of Birth	: 12 September 1976, Tokat, Turkey
Phone	: +90 312 240 84 41
Fax	: +90 312 354 52 05
Email	: udoyuran@aselsan.com.tr

EDUCATION

Degree	Institution	Year of Graduation
MS	METU Electrical and Electronics Engineering	2001
BS	METU Electrical and Electronics Engineering	1998
High School	Tokat Anadolu Lisesi, Tokat	1994

WORK EXPERIENCE

Year	Place	Enrollment
2005- Present	ASELSAN Inc.	Systems Engineer
1998-2005	METU Department of Electrical and Electronics Engineering	Research Assistant
1996,1997 August	TÜBİTAK BİLTEN	Intern Engineering Student

FOREIGN LANGUAGES

English, German

PUBLICATIONS

1. Doyuran, Ü, Tanık Y. "Radar belirsizlik ve kör bölge çözümünde değişken darbe aralığı," Proceedings of ITUSEM 2005, November 2005, pp.219-222.
2. Doyuran U, Tanik Y., "Weibull kargaşa haritalı radar hedef tespiti," *URSI Türkiye 2006*, pp.601-603, Eylül 2006.
3. Doyuran U, Tanik Y., "Detection in range-heterogeneous Weibull clutter," *IEEE Radar Conference*, pp.343-347, April 2007.
4. Doyuran U, Tanik Y., "Değişken kargaşa altında radar hedef tespiti," *SİU 2007*, Haziran 2007.
5. Doyuran U, Tanik Y., "Multi-Range and Multi-Pulse Radar detection in correlated non-Gaussian clutter," *European Radar Conference*, October 2007 (to be published).